MEASUREMENT OF LATTICE STRAIN AND RELAXATION EFFECTS IN STRAINED SILICON USING X-RAY DIFFRACTION AND CONVERGENT BEAM ELECTRON DIFFRACTION

David Robert Diercks, B.S., M.S.

Dissertation Prepared for the Degree of

DOCTOR OF PHILOSOPHY

UNIVERSITY OF NORTH TEXAS

August 2007

APPROVED:

Michael J. Kaufman, Major Professor and Department Chair
Rajarshi Banerjee, Committee Member
Brian P. Gorman, Committee Member
Richard F. Reidy, Committee Member
Nandika A. D'Souza, Program Coordinator
Oscar Garcia, Dean of the College of Engineering
Sandra L. Terrell, Dean of the Robert B. Toulouse School of Graduate Studies

Diercks, David Robert, Measurement of Lattice Strain and Relaxation Effects in Strained Silicon Using X-ray Diffraction and Convergent Beam Electron Diffraction. Doctor of Philosophy (Materials Science and Engineering), August 2007, 144 pp., 8 tables, 127 illustrations, references, 80 titles.

The semiconductor industry has decreased silicon-based device feature sizes dramatically over the last two decades for improved performance. However, current technology has approached the limit of achievable enhancement via this method. Therefore, other techniques, including introducing stress into the silicon structure, are being used to further advance device performance. While these methods produce successful results, there is not a proven reliable method for stress and strain measurements on the nanometer scale characteristic of these devices. The ability to correlate local strain values with processing parameters and device performance would allow for more rapid improvements and better process control. In this research, x-ray diffraction and convergent beam electron diffraction have been utilized to quantify the strain behavior of simple and complex strained silicon-based systems. While the stress relaxation caused by thinning of the strained structures to electron transparency complicates these measurements, it has been quantified and shows reasonable agreement with expected values. The relaxation values have been incorporated into the strain determination from relative shifts in the higher order Laue zone lines visible in convergent beam electron diffraction patterns. The local strain values determined using three incident electron beam directions with different degrees of tilt relative to the device structure have been compared and exhibit excellent agreement.

ACKNOWLEDGEMENTS

I would like to thank my advisor Mike Kaufman for instructive guidance, constant support, and friendship. I also thank each of my other committee members, Raj Banerjee, Brian Gorman, and Rick Reidy for being extremely helpful and making my time here both instructive and enjoyable. Additionally, I appreciate the help of the departmental staff.

My labmates and classmates have also enriched my experience here through friendships, thoughtful discussions, helpfulness, and keeping things fun. I especially thank Ananth and Jun for their friendship and helpfulness. Among the several other students who have played important roles in my life here are Casey, Kris, Meggan, Maia, Pawan, Suman, Uma, and Vaishali and two REU students, Sarah and Stephanie.

And the most important person in my life, my wife Megan, has been nothing but patient and supportive of me. She makes each day better for me.

I also gratefully acknowledge the Semiconductor Research Corporation for funding this project through a Texas Instruments custom grant. Additionally, several Texas Instruments employees have provided support and encouragement on this project, including: Rich Irwin, Amitabh Jain, Lance Robertson, Hans Weijtmans, and Rick Wise.

TABLE OF CONTENTS

Page

LIST OF TABLES

Page

LIST OF FIGURES

Page

CHAPTER 1

OVERALL MOTIVATION

The continued drive for faster and cheaper integrated circuits has resulted in dramatic decreases in the feature sizes in metal-oxide-silicon field effect transistors (MOSFETs). Smaller devices allow faster performance due to the decreased path length for charge transport. Cost reductions are also achieved in reduced scale devices because of the ability to incorporate more functionality in a given volume. Gordon Moore was the first to publicly express these trends, which have subsequently been dubbed “Moore’s Law,” and their advantages [1]. The size and cost reductions of transistors since 1970 are shown in Figure 1.1.

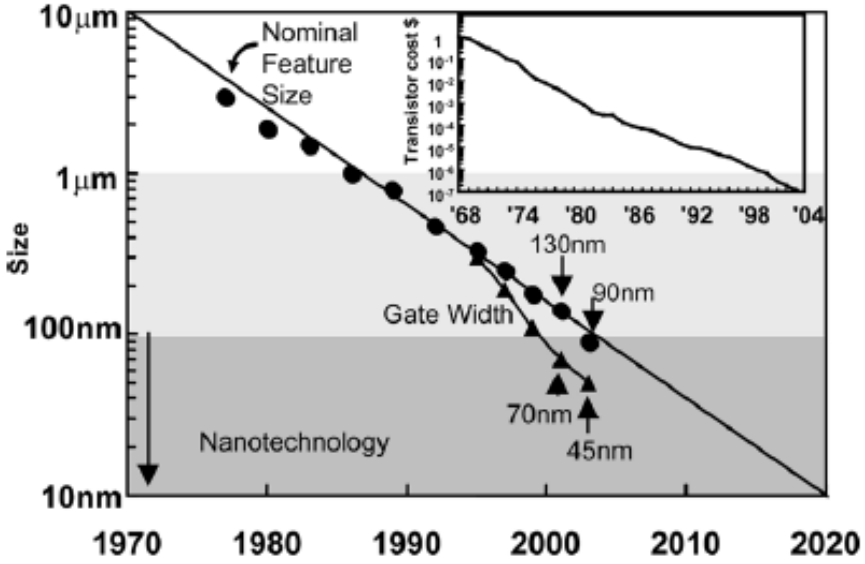

Figure 1.1 – Transistor feature size and cost versus year from ref [2]. (© 2004 IEEE) Used by permission.

While the exponential reduction in transistor size has been achieved mainly through simple scaling of feature size, the current technology has approached the theoretical limit of what can be accomplished via scaling [3,4]. Therefore, other means of increasing performance have been introduced. Straining the silicon is one of the most recent approaches to be incorporated in MOSFETs [5-7]. Several methods of straining silicon have been researched. Whole wafer techniques can be used to introduce biaxial stresses into the system, whereas local stressing methods are used to introduce uniaxial stresses.

It has been shown that biaxial tensile stress has the potential to enhance charge mobility in both n- and p-MOSFETs [7-8] depending on channel orientation. However, the whole wafer techniques for introducing stress also require extensive modification of the fabrication processes. So, the difficulty of incorporating this technology into the current fabrication schemes has been a barrier to introduction of this method into production devices. Since uniaxial stress poses fewer challenges for incorporation into existing systems, this method of charge mobility enhancement has already been successfully utilized in production devices [2,8].

One difficulty with uniaxial stress is that the direction of stress needed for enhanced mobility is opposite for hole and electron transport. Longitudinal compressive stress enhances hole mobility, as shown in Figure 1.2, whereas longitudinal tensile stress is needed to enhance electron mobility. Therefore multiple methods of introducing local stresses are necessary. Methods that have been developed for creating local uniaxial stress include: source/drain modification, capping layers, and stress liners [4,6,10].

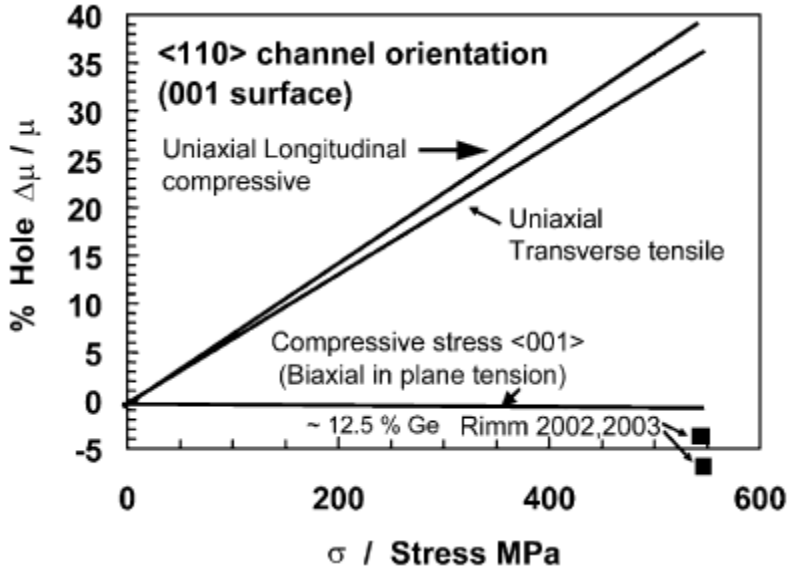

Figure 1.2 – Hole mobility enhancement as a function of stress from ref [2]. (© 2004 IEEE) Used by permission.

The ability to measure these stress values is of great importance in being able to systematically control, and therefore improve, MOSFET performance via strained silicon. Because the strains are introduced locally on devices that have channel lengths of less than 100 nm, there are few techniques capable of providing quantitative strain values for individual gate channels.

The next section will highlight a few methods that have been used for measuring strain in silicon-based microelectronics and provide the background on why convergent beam electron diffraction (CBED) is a promising technique for this problem.

CHAPTER 2

STRAIN MEASUREMENTS IN SILICON

Several techniques have been used for measuring strain in silicon-based microelectronics. These include x-ray diffraction (XRD), Raman spectroscopy, and convergent beam electron diffraction (CBED).

2.1 X-Ray Diffraction

In XRD, an x-ray source is created via the acceleration of thermally emitted electrons from a tungsten filament into a metal target. The decay of some of the excitation events caused by these electrons results in x-ray emission. The wavelength of these x-rays is governed by the characteristic energy levels of the target metal. The most commonly used metals for this are Mo, Cu, Co, and Cr. These x-rays are directed and focused toward the area of interest. Due to the difficulty in focusing the uncharged, large wavelength x-rays, lateral resolution is typically several hundred micrometers. The depth of penetration of x-rays is dependent on the scattering factor of the material examined.

Many x-rays that strike the material undergo diffraction events. These diffracted x-rays may interfere with each other, both destructively and constructively. Constructive interference results in output x-ray signals at particular angular relationships between the incident beam, the crystal structure, and the specimen orientation. Bragg's law defines these relationships:

$$n \cdot \lambda = 2 \cdot d \cdot \sin(\theta) \qquad (2.1)$$

where n is an integer, λ is the wavelength of the x-rays, d is the d-spacing for a particular set of crystallographic planes, and θ is the angle between the incident x-rays and the crystallographic planes causing the diffraction. This is shown schematically in Figure 2.1.

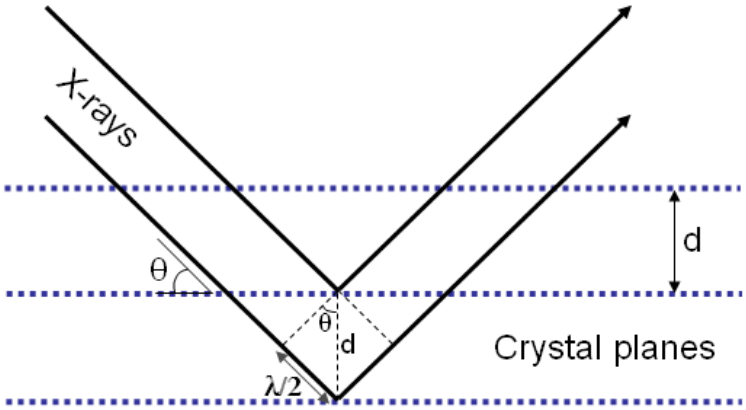

Figure 2.1 – Illustration of Bragg's law for diffraction from a crystalline material

The local d-spacings of crystallographic planes change as a material is strained. Therefore, from Bragg's equation it can be seen that changes in d will alter the angles at which diffraction events are detected for a fixed wavelength. The result is that the angles at which constructive interference occurs will be shifted relative to the unstrained material. It is these shifts in XRD peak positions that are used to quantify the strain in the material.

Some limitations of using XRD for measuring strain in silicon are: limited spatial resolution, imprecise depth resolution, and challenges associated with peak deconvolution.

Therefore the use of x-ray diffraction for strain measurements in silicon has typically been limited to whole wafer measurements and thin film characterization [11-13]. Among the thin film quantities that can be determined with this method are film thickness, interfacial roughness, strain, and, for crystalline solid solutions, elemental concentration.

Thickness measurements are based on the diffracted beams from the film and the substrate interfering with each other. The fringe period is inversely related to the film thickness as shown in the following relation [14]:

$$t = \frac{\lambda \cdot \sin(\theta_B + \varphi)}{d\theta_p \cdot \sin(2\theta_B)} \qquad (2.2)$$

where t is the film thickness, λ the incident wavelength, θ_B the Bragg angle, φ the angle between the Bragg planes and the crystal surface, and $d\theta_p$ the fringe period. It can also be seen that for a given film, variations in film thickness or the orientation between the Bragg planes and crystal surface will affect the fringe period. Therefore these fringes also give an indication of the film quality.

For thin films that are expected to have some lattice relationship with the substrate, a series of $\omega/2\theta$ scans around Bragg diffraction peaks may be performed in order to produce a two-dimensional reciprocal space representation. The lattice parameters derived from this give an indication of the film strain. For a film that is lattice-matched to the substrate, elastic moduli may be used to determine what the unstrained lattice parameters of the film are. Additionally, for solid solutions where the relationship between relative concentration and lattice parameters is known or can be

assumed (i.e. using Vegard's law), this unstrained lattice parameter value may be used to determine elemental concentration.

Recent efforts to improve upon the beam size limitations have utilized so-called "x-ray microbeams." The formation of these typically requires using synchrotron x-ray sources or other methods of decreasing angular divergence and advanced x-ray focusing optics. These methods have been implemented for strain measurement in copper and have been able to produce sub-micrometer x-ray spot sizes [15]. Unfortunately, the beam size is insufficiently large for the nanometer scale spatial resolution necessary for the devices in this research.

2.2 Raman Spectroscopy

In Raman spectroscopy a coherent light source is focused on the sample and the frequency of the scattered light is collected and analyzed. Most of the scattered photons have the same energy, and therefore wavelength, as the incident light (Rayleigh scattering). However, a very small percentage of photons change the vibrational state of the molecules they interact with and also, therefore, undergo a change in optical frequency. Most of these are Stokes-shifted to lower energies (longer wavelengths), but some are anti-Stokes-shifted to higher energies (shorter wavelengths). It is these shifts from the incident wavelength that are used for characterization of the material. Since the molecules' vibrational states are a function of their bonding arrangements, the amount of change in wavelength of the scattered light is also dependent on the material's bonding. The bond state of the material can be affected by the types of atoms, bond order, orbital hybridization state, and strain state, among other factors.

The resolution of objects using parallel beam optics is directly proportional to the incident wavelength and inversely proportional to the refractive index of the medium through which it passes. Therefore, smaller laser spot sizes have been obtained using shorter wavelength optical and ultraviolet light and reducing the refractive index via oil-immersion. The incorporation of near-field scanning optical microscopy (NSOM or SNOM) into Raman spectroscopy is also being investigated for improving the spatial resolution to beyond the diffraction limit [16].

An additional difficulty in Raman spectroscopy is in the deconvolution of the causes of the peak shift. The strain tensor is a second rank tensor and, therefore, there may be several components of the tensor each contributing to the overall shift. Also, local compositional fluctuations can cause changes in the peak position and may not be distinguishable from strain-induced shifts.

Raman spectroscopy has been used to measure strain in several microelectronics features in the sub-micron to tens of microns range [10,17,18].

2.3 Transmission Electron Microscopy

In transmission electron microscopy (TEM), a beam of electrons generated from either a filament or a field emission gun (FEG) is focused and accelerated down a column where it passes through a very thin specimen. The resulting interaction of the electrons with the specimen can be used to image and characterize many aspects of the specimen including mass contrast, phase contrast, defects, interfaces, density variations, atomic composition, crystal structure and orientation, and lattice parameters. A schematic of bright field imaging and parallel beam diffraction in the TEM is shown in Figure 2.2.

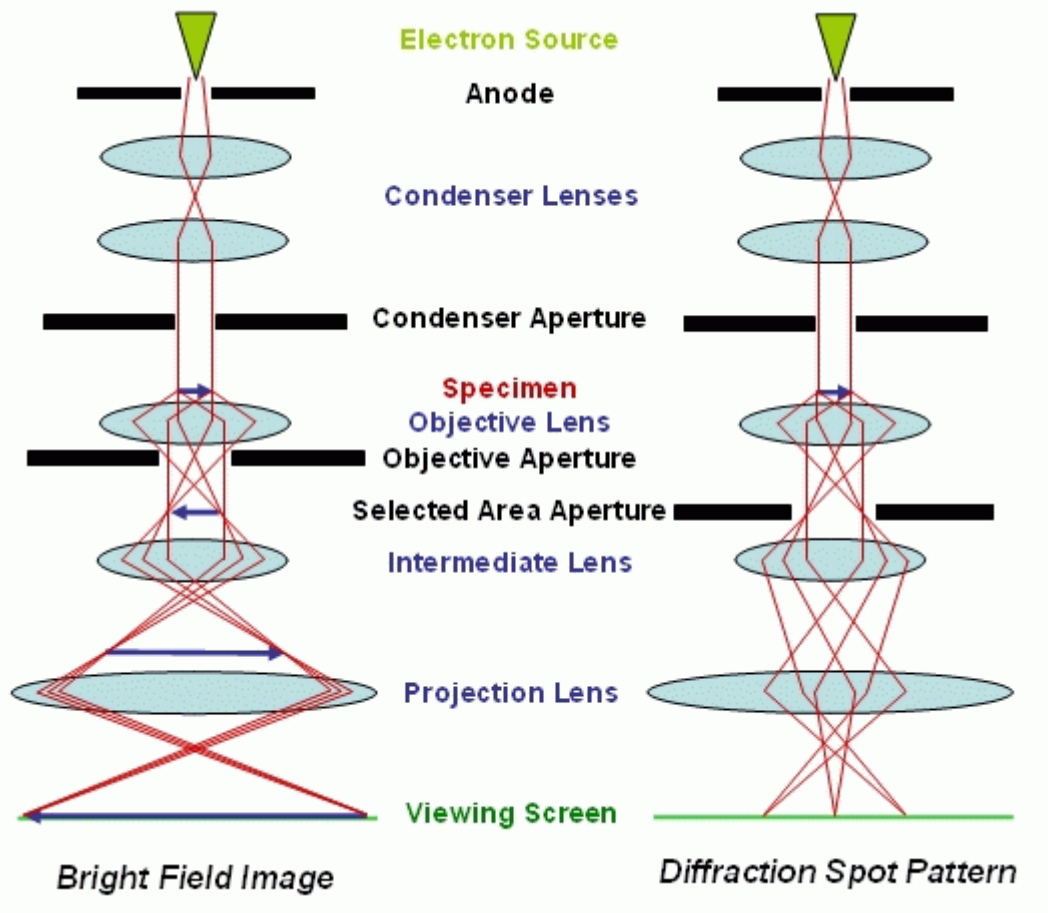

Figure 2.2 – Schematic illustrations of the transmission electron microscope for (a) bright field imaging and (b) diffraction spot pattern collection.

Diffraction in the TEM occurs via the same wavelength interference mechanism as in x-ray diffraction. However, the wavelengths of electrons produced by the high acceleration voltages in TEMs are orders of magnitude smaller than the wavelengths of x-rays. Therefore, the angles of diffraction are much smaller – so much so that the planes which produce the diffraction patterns are nearly parallel to the incident electron beam.

Additionally, the small specimen thicknesses necessary for electron transparency result in the expansion of the intensity of constructive interference about the Bragg angle as there is insufficient material to cause complete destructive interference for

angles close to the Bragg angle. This broadening is represented by a broadening of the reciprocal lattice in a direction parallel to the thin direction of the sample. Thus, instead of the reciprocal lattice consisting of points, it can be viewed as an array of rods. These reciprocal lattice rods mean that there will be diffracted intensity from planes slightly off of the exact Bragg condition.

The reason for the expansion of the reciprocal lattice points can be seen by considering the following. The scattering intensity of a reciprocal lattice vector k by a group of unit cells is given by the following relation:

$$\phi_g = \sum_{n=1}^{N} F_n e^{-2\pi i \mathbf{k}\cdot\mathbf{r}} \qquad (2.3)$$

where ϕ_g is the is the amplitude of scattering, N the number of unit cells, F_n the structure factor for unit cell n, and r the distance over which the wavevector propagates. Assuming a large number of unit cells in the specimen, this becomes an integral:

$$\phi_g = \frac{F_n}{V_c} \int e^{-2\pi i \mathbf{k}\cdot\mathbf{r}} d\mathbf{r} \qquad (2.4)$$

where V_c is the volume of the unit cell. Defining this in Cartesian coordinates gives:

$$\phi_g = \frac{F_n}{V_c} \int_0^A \int_0^B \int_0^C e^{-2\pi i \mathbf{k}\cdot\mathbf{r}} dx dy dz \qquad (2.5)$$

where A, B, and C are the specimen dimensions in the x, y, and z directions, respectively. Equation 2.5 is the Fourier transform of the specimen along its x, y, and z directions. Thus, with the specimen being thinner in the z direction in real space, the reciprocal space dimension lengthens in that direction, creating reciprocal lattice rods (relrods).

2.3.1 Convergent Beam Electron Diffraction

The first TEM was developed by Knoll and Ruska in the early 1930s. Shortly after that Kossel and Möllenstedt developed the convergent beam electron diffraction (CBED) method for analyzing specimens [19]. CBED is a technique used in TEM whereby a diffraction pattern is created from the electron beam focused on a small volume of material.

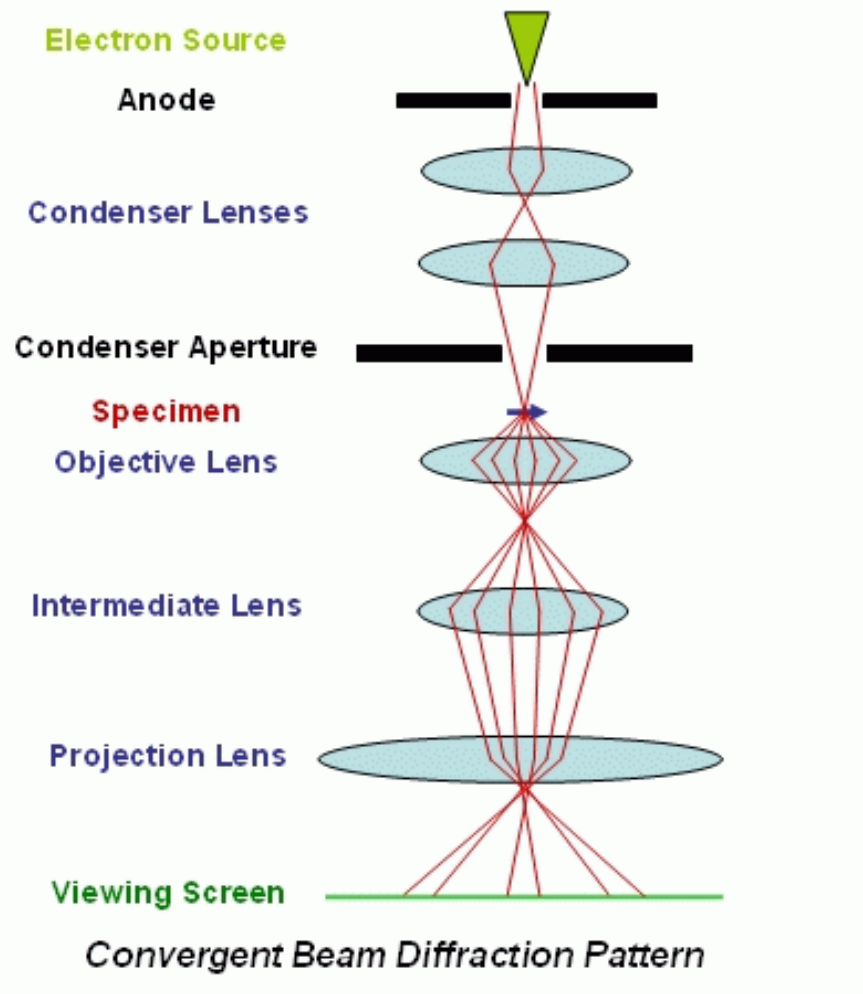

Figure 2.3 – Schematic illustration of the collection of a convergent beam electron diffraction pattern.

Diffraction images created using a parallel electron beam arrangement result in a diffraction spot pattern, whereas in a convergent beam arrangement, these spots are broadened out into disks. The convergent beam can be thought of as a grouping of small parallel electron beams all having slightly different three-dimensional orientations. Schematic drawings comparing the two diffraction arrangements are shown in Figures 2.2(b) and 2.3.

Two advantages of CBED versus parallel beam diffraction are that a smaller area can be probed and that three-dimensional information about the structure can be ascertained. This three-dimensional information can be used to determine the specimen thickness, crystal space group, and lattice parameters (and, therefore, strain).

2.3.1.1 Thickness Determination Using CBED

The thickness determination is performed under a two-beam condition, that is, by tilting the sample such that there is only the transmitted beam and one strongly excited reflection (or set of reflections) from a single set of planes. Under this condition, the reflected *hkl* disk contains symmetric intensity oscillations and the 000 disk contains asymmetric ones called Kossel-Möllenstedt fringes. An example of such a pattern is shown in Figure 2.4.

These oscillations arise from the summation of the transmitted and diffracted intensities by the crystal structure through the thickness of the specimen. This causes a sinusoidal behavior in the intensity with the transmitted and diffracted beams' behavior being opposite – the lowest intensity for one is the peak intensity for the other. The physical distance over which one complete oscillation occurs is called the extinction

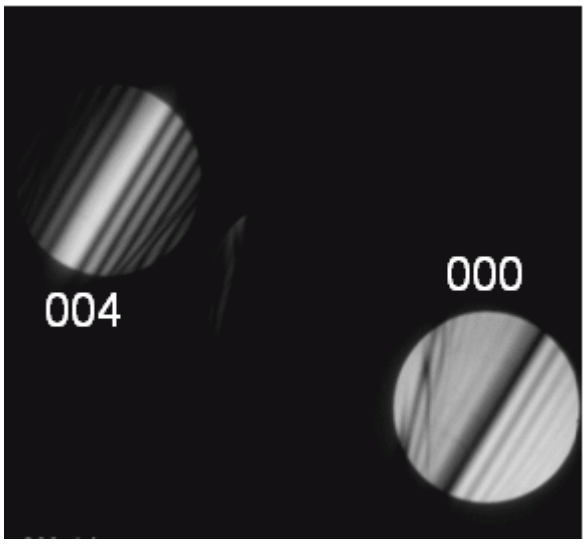

Figure 2.4 – Two beam diffraction condition for the 004 refection in silicon showing the Kossel-Möllenstedt fringes. They are asymmetric in the 000 disk and symmetric in the diffracted disk.

distance (ξ_g). Due to the nature of how this effect arises, the extinction distance depends on the electron beam acceleration voltage, the material, the crystal structure, and the crystal direction. The number and size of the fringes in the disks therefore depend on all these factors and the physical distance the electron beam traverses in the specimen. Thus, if the extinction distance is known for a given set of conditions, the thickness of the specimen can be determined. The exact Bragg condition, where the deviation parameter, s, equals zero, is the bright central fringe in the *hkl* disk and the fringe spacings correspond to angular deviations ($\Delta\theta$) from the Bragg condition. Therefore, the deviation for the *i*th fringe is given by:

$$s_i = \lambda \frac{\Delta\theta_i}{2\theta_B d^2} \qquad (2.6)$$

where λ is the electron wavelength, θ_B the Bragg angle for the diffracting plane, and d the interplanar spacing. This value s_i can then be substituted into the equation relating the extinction distance and the specimen thickness:

$$\frac{s_i^2}{n_k^2} + \frac{1}{\xi_g^2 n_k^2} = \frac{1}{t^2} \qquad (2.7)$$

where n_k is an integer and t is the specimen thickness.

However, if the extinction distance is not known for a set of conditions, the thickness can still be extracted based on the equations that govern the spacing of these fringes. Since equation 2.7 is linear, plotting (s_i^2/n_k^2) versus $(1/n_k^2)$ for a series of fringes gives a slope of $(1/\xi_g^2)$ and a y-intercept of $(1/t^2)$. Therefore, for an unknown extinction distance, the spacings of several fringes from the central fringe in the diffracted disk can be measured. Then a series of integers can be assigned to the n_k values until a series that produces the appropriate linear relationship is found. The specimen thickness is then given by the y-intercept.

2.3.1.2 Lattice Parameter Determination Using CBED

The crystal structure can be determined by looking at the CBED patterns from a few major zone axes. The symmetry within the central disk and from the whole pattern for a given zone axis can be used to identify the possible point groups of the crystal. For an unknown system, the use of multiple zone axes is generally necessary to obtain only one possible point group for the system. The space-group can then be determined by looking at the dynamical absences, or Gjønnes-Moodie lines, of disks in the zone axis patterns [20].

Once the crystal structure is known, higher order Laue zone, or HOLZ, lines can be used to determine deviations from the equilibrium lattice parameters in a given region or relative deviations between regions. HOLZ lines arise due to diffraction from planes not parallel to the incident electron beam. As shown in the Ewald sphere construction (Figure 2.5), the first set of reciprocal lattice points above the zero order Laue zone (ZOLZ) are called the first order Laue zone (FOLZ) and correspond to the condition hu+kv+lw=1 where h, k, and l are the indices for the diffracting plane and u, v, and w are the indices for the incident beam direction, the next set are called the second

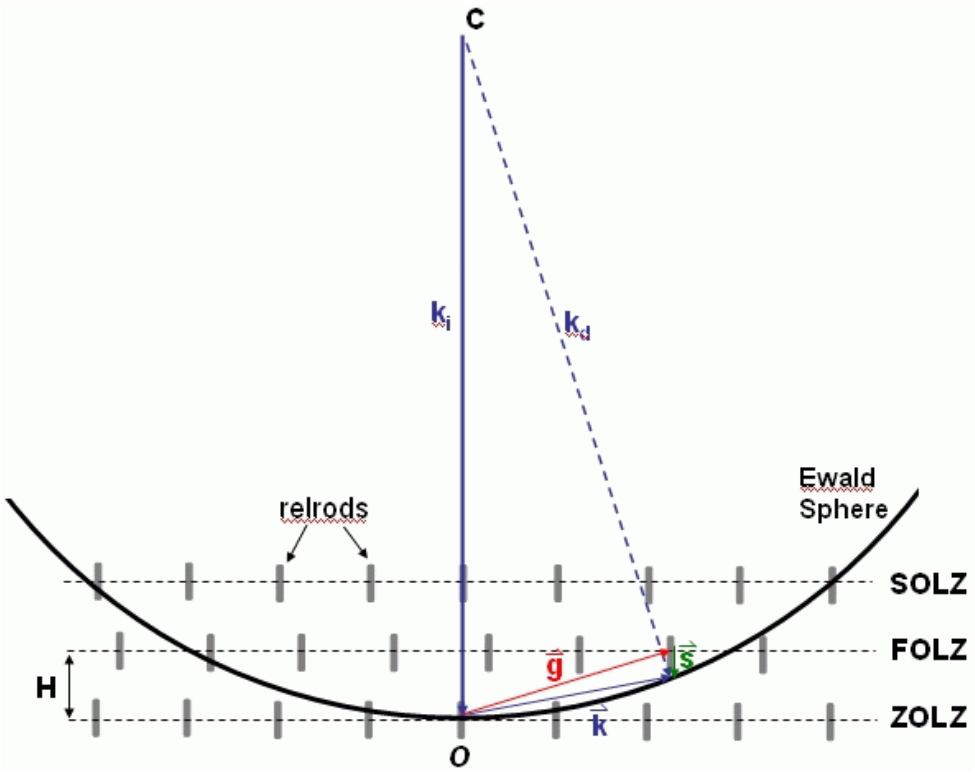

Figure 2.5 – Reciprocal space schematic showing the diffraction conditions for the zero order Laue zone (ZOLZ), first order Laue zone (FOLZ), and second order Laue zone (SOLZ) by intersection of the Ewald sphere with the relrods. H is the reciprocal lattice spacing. The incident and diffracted electron beams are given by k_i and k_d respectively. The diffraction vector is given by g and the deviation parameter is given by s.

order Laue zone (SOLZ), etc. All of these planes above the ZOLZ are generically referred to as HOLZ. The HOLZ reciprocal lattice points that are intersected by the Ewald sphere meet the diffraction conditions of equation 2.1 but are not oriented parallel to the incident electron beam axis.

The diffracted intensity from these planes is scattered out to relatively high angles, resulting in a series of concentric, bright rings around the ZOLZ pattern. Inside the central 000 disk of the ZOLZ are fine, dark lines, each associated with one of the bright lines in the outer rings of reflections. A diffraction pattern showing a ring of HOLZ reflections are shown in Figure 2.6. The bright lines are called “excess” lines, and the dark ones “deficit” lines. It is the deficit lines that are used for lattice parameter determinations because the close proximity of the lines makes small shifts in the line positions more readily detectable.

Due to their sensitivity to small lattice parameter changes, the potential for using HOLZ lines for strain determination was recognized with their discovery and explanation by Jones et al. [21] and has been utilized by numerous authors for many materials [22-25]. This technique involves using a small (~1 nm) convergent probe to generate a diffraction pattern where the central disk contains the HOLZ deficit lines that are very sensitive to slight elastic distortions to the lattice. The sensitivity of CBED to lattice strain is on the order of 2×10^{-4} [26-27]; this corresponds to a minimum stress of ~35 MPa for silicon. Cooling the specimen and using electron energy filtering can provide additional improvements in HOLZ line resolution. Both of these methods decrease the diffuse background caused by inelastically scattered electrons. In energy filtering, a selection slit is used to control the energy of the electrons that are used in the image

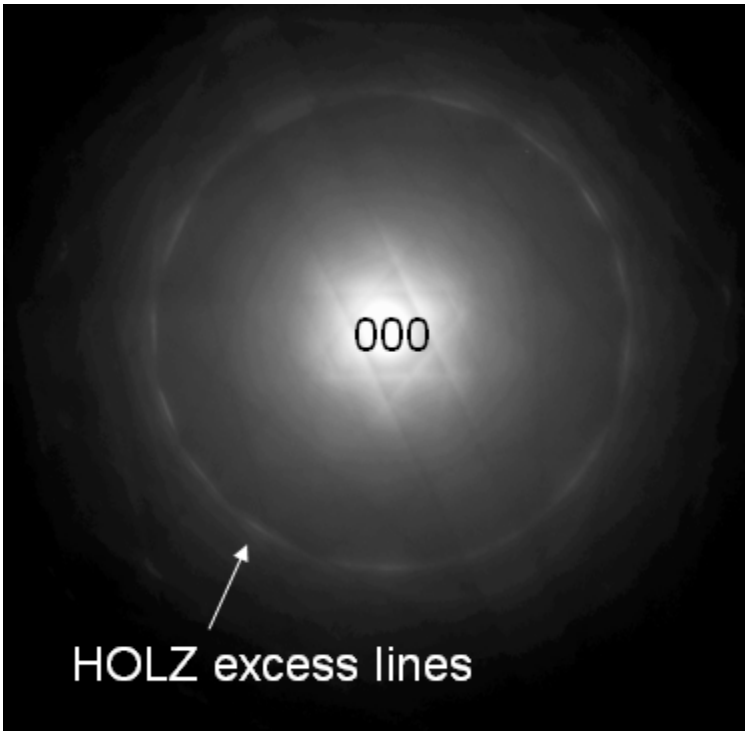

Figure 2.6 – Silicon <120> CBED pattern showing the ring of excess HOLZ lines around the central transmitted disk.

display. A comparison of an unfiltered and an energy filtered HOLZ line pattern is shown in Figure 2.7. Further, both kinematical and dynamical simulation programs have been developed to model the HOLZ patterns as a function of lattice distortion (i.e., strain state) [28-30].

The use of HOLZ line patterns for strain determination in silicon has primarily been concerned with complimentary metal-oxide-semiconductor (CMOS) devices. There are several sources of stresses and strains in CMOS devices. Non-uniform temperature distribution during thermal processing may lead to wafer warpage, local plastic deformation, or slip. During film growth, thermal expansion mismatch and lattice mismatch can lead to stresses in the films and substrate. This is especially prominent at corners, such as in trenches [31]. Localized oxidation or other reactive growth

mechanisms can lead to volume changes, which induce stress. Each of these can cause a number of deleterious effects leading to decreased production yield and reduced device performance.

Because of this, several research groups began using CBED to quantifiably measure these local deleterious strains in CMOS devices. These included measurements around shallow trench isolation structures [32-34], local oxidation of silicon (LOCOS) structures [35], and silicides [36].

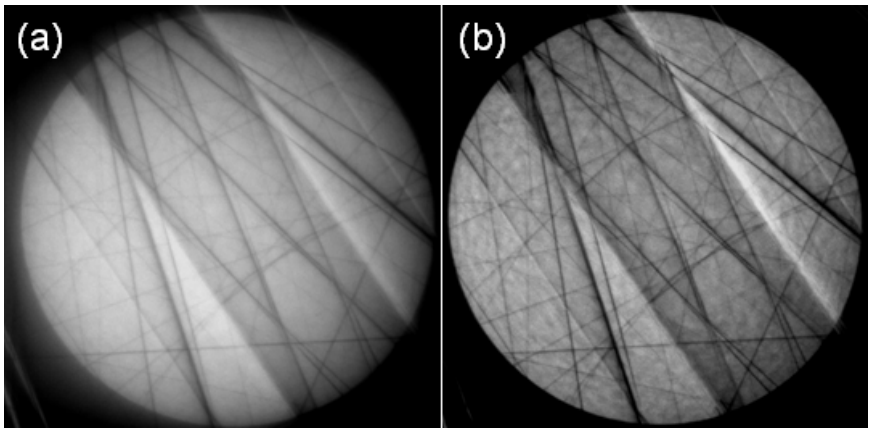

Figure 2.7 – (a) Unfiltered and (b) energy-filtered HOLZ line patterns. A 30eV window around the zero-loss electron peak was used in the energy-filtered pattern.

Researchers have also sought to use strain in silicon-based devices in a beneficial manner. $Si/Si_{1-x}Ge_x$ multilayer heterostructures were among the first attempts at using strain to increase carrier mobility. CBED investigations on such structures were concerned with measuring strain along and through the layers as a function of Ge content and layer thickness [25, 37-38]. More recently, the intentional introduction of strain into the channel areas of transistors increases the importance of measuring stress and strain on a fine scale. Therefore this research seeks to apply CBED to the

strain measurements of intentionally stressed, 65-nm technology node p-MOSFETs having gate lengths of 35-40 nm.

In this chapter several of the advantages of using CBED for strain measurement have been highlighted. There are also many challenges associated with using TEM HOLZ line patterns for strain measurement. These will be discussed in the appropriate sections of chapter 4.

CHAPTER 3

EXPERIMENTAL PROCEDURE

A variety of specimens were analyzed in this research. These include blanket wafers of ~50nm of chemical vapor deposited $Si_{.85}Ge_{.15}$ on (001) Si (subsequently called SiGe01) and ~127nm of $Si_{.78}Ge_{.22}$ on (001) Si (subsequently called SiGe02), and 40 nm gate length p-MOSFET structures with recessed SiGe stressors in wafers removed from production just after gate fabrication and also those from fully-processed wafers.

3.1 Blanket Wafers

3.1.1 X-Ray Diffraction

A Rigaku Ultima III X-Ray Diffractometer (XRD) was used to characterize the strain and composition of the SiGe films on (001) Si. ω - $\omega/2\theta$ scans were performed around the 004, 113, and 224 peaks for the SiGe film and Si substrate in order to create reciprocal space maps. For these scans, a series of continuous $\omega/2\theta$ scans were collected with the starting ω value incremented by 0.01° for each subsequent scan. The 004 scan allows for the best resolution of the lattice spacing in the [001] direction and the 224 scan gives the best resolution in the [110] direction. The 113 scan, in addition to providing verification of the results from the other two scans, has an incident beam angle of less than 3°. Therefore a greater proportion of counts from this scan are from the film. Any small variations in the film structure would be most noticeable in this geometry. The scan geometries are shown in Figures 3.1-3.3.

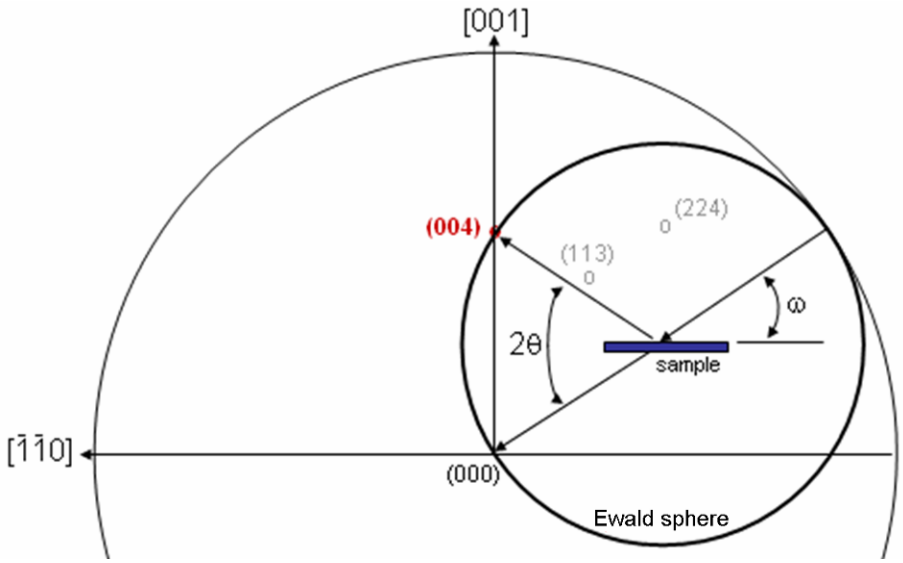

Figure 3.1 – The reciprocal space geometry of the ω - $\omega/2\theta$ XRD scan around the (004) peaks for the blanket wafers.

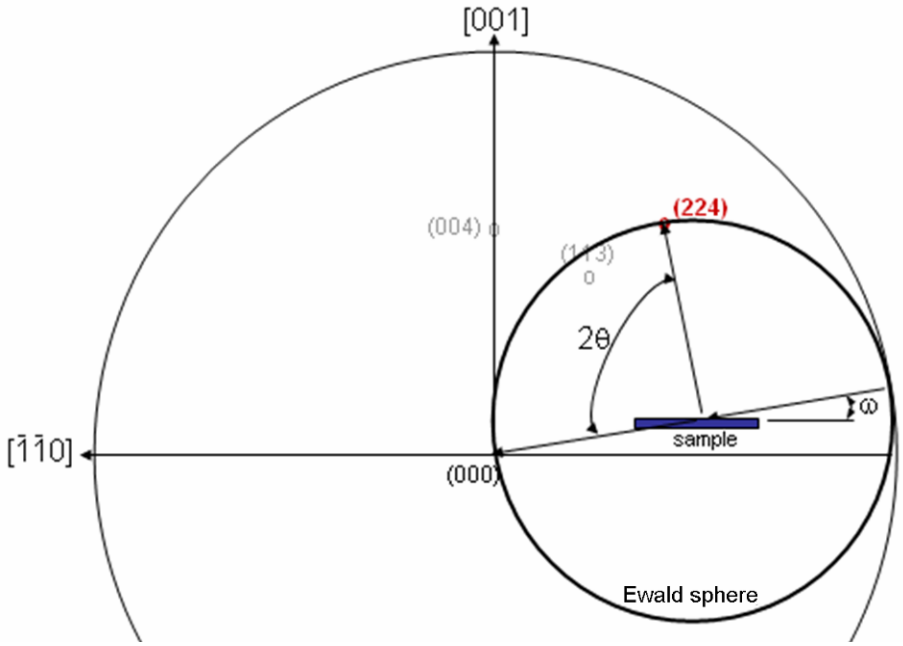

Figure 3.2 – The reciprocal space geometry of the ω - $\omega/2\theta$ XRD scan around the (224) peaks for the blanket wafers.

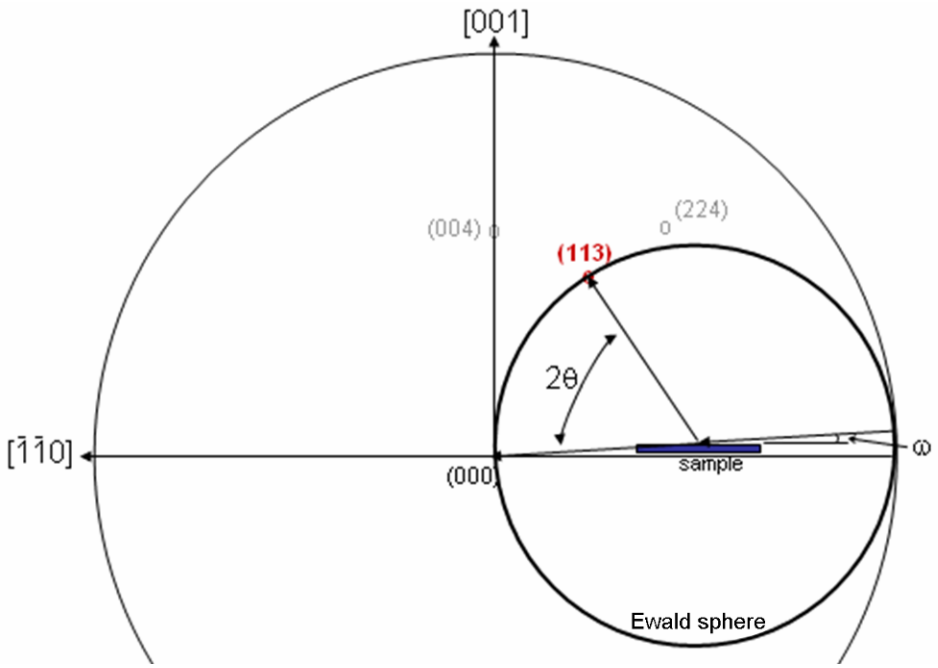

Figure 3.3 – The reciprocal space geometry of the ω - $\omega/2\theta$ XRD scan around the (113) peaks for the blanket wafers.

Rocking curves were also obtained around the (004), (224), and (113) silicon peaks using $\omega/2\theta$ scans to confirm the reciprocal space map values and to ascertain the film thicknesses.

3.1.2 Transmission Electron Microscopy

Three different methods of transmission electron microscopy (TEM) specimen preparation were used in this research. The first method was that traditionally used for cross-sectional TEM samples, that is, small sections of the substrate were glued together, diced in cross-section, and thinned. The thinned material was cut into 3 mm disks, attached to a copper grid, and then dimpled. Finally, the samples were argon-ion milled in a Gatan model 691 Precision Ion Polishing System at a 4° incident angle. This method is shown in Figure 3.4.

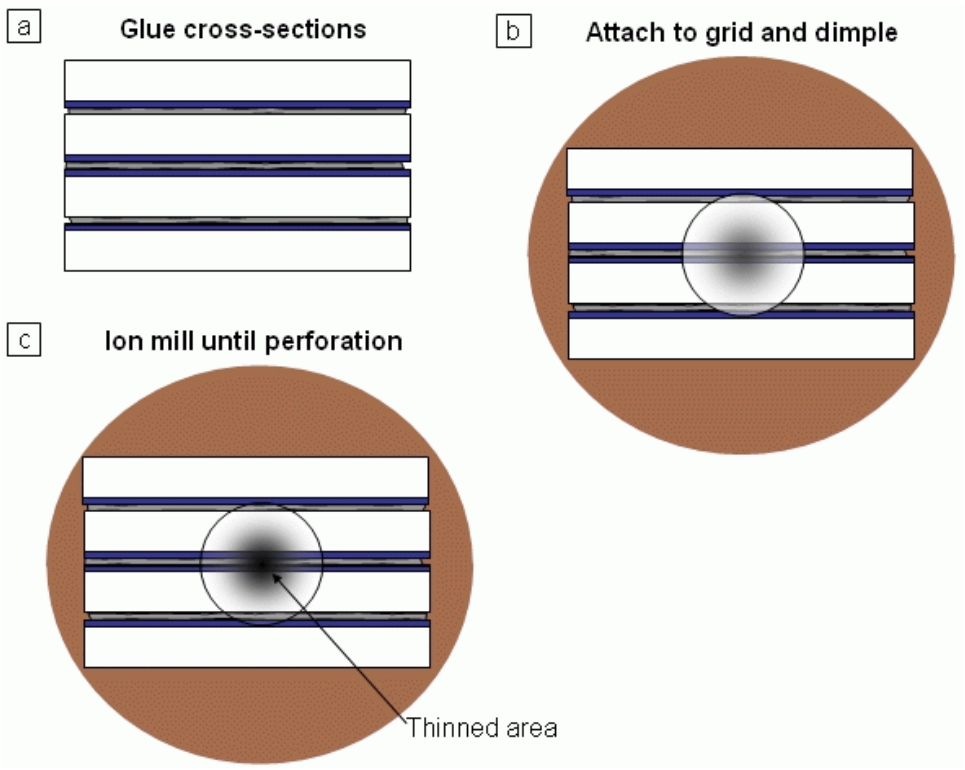

Figure 3.4 – Traditional method for cross-sectional TEM sample preparation. (a) Thin cross-section slices are glued together. (b) The cross-sections are attached to a TEM grid and undergo dimple grinding to near perforation. (c) Argon ion milling is then performed until perforation of the sample.

The other two methods of sample preparation utilized an FEI Nova 200 focused ion beam (FIB) system. In both of these the area of interest was first protected through electron beam deposition of a layer of platinum from a gaseous platinum-containing organic precursor. After electron beam deposition of a platinum layer at least fifty nanometers in thickness, a gallium ion beam was used to further deposit platinum to a total layer thickness of ~2.5 microns. This thickness provided ample protection of the area of interest from ion-beam damage during subsequent milling steps.

The first FIB method involved hand polishing a cross-sectioned sample to less than 100 microns, then gluing this piece to a semicircular copper grid for final thinning in

the FIB as shown in Figure 3.5. This method will subsequently be called the "H-bar method."

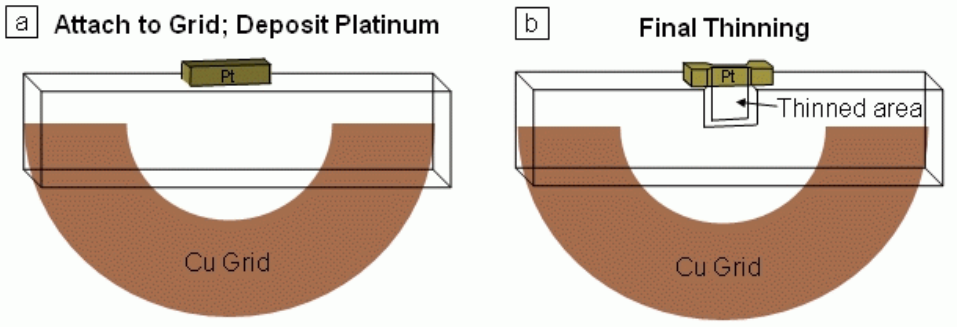

Figure 3.5 – H-bar cross-sectional TEM sample preparation method. (a) A cross-section piece is mechanically thinned to less than 100 microns and attached to a semi-circular TEM grid. Platinum is deposited over the area of interest using gaseous platinum-containing molecules. (b) A focused ion beam system is then used to thin the specimen with gallium ions.

In the other FIB method, the specimen was removed from the bulk wafer using the FIB system. First, a U-shaped pattern was milled around the platinum-protected region. Next, a cut was made at 52° to the initial U-cut to free the wedge from the substrate. This wedge was then attached (using the platinum) to an Omniprobe Autoprobe 200 needle, lifted out of the host material, and then connected to a post on a semi-circular copper grid. From there, final thinning of the specimen was performed using the gallium ion beam. This method, depicted in Figure 3.6, will subsequently be referred to as the "lift-out method."

For those samples milled in the FIB system, a 30kV voltage was used to reduce the specimens to less than 800 nm thick. Thinning to the final specimen thickness was performed with a 5kV beam voltage in order to limit the amount of damage to the surfaces of the specimen. Additionally, after the FIB processing, these specimens were

cleaned for 30 seconds with an argon plasma in a South Bay Technology PC-2000 plasma cleaner.

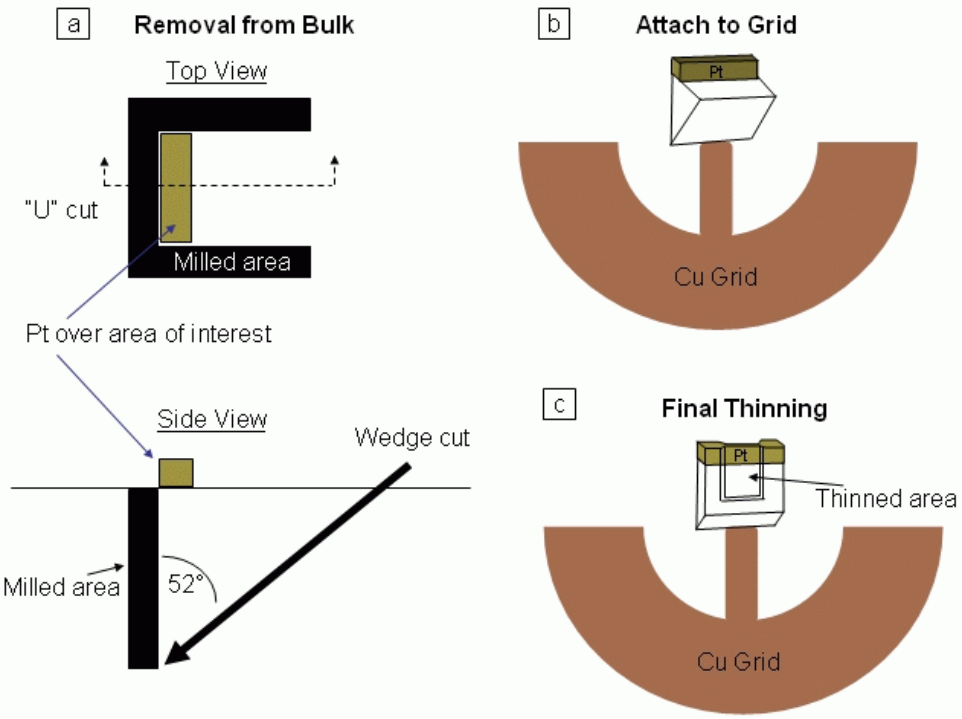

Figure 3.6 – Lift-out cross-sectional TEM sample preparation method. (a) Platinum is deposited over the area of interest using a gaseous platinum-containing molecule. A gallium ion beam is used to mill around the area of interest (top view). The wafer is then tilted 52° to make an angular cut which frees the wedge-shaped specimen from the wafer. (b) This specimen is removed from the substrate using a micro-manipulator and is attached to a post on a copper TEM grid using platinum. (c) A focused ion beam system is then used to thin the specimen with gallium ions.

For the blanket wafer specimens, most samples were thinned into a wedge shape as shown in Figure 3.7. This provided the capability to measure the effects of specimen thickness via the preparation of only one specimen. Specimens of constant thickness were also prepared to verify that the results observed were not an effect of the sample geometry. The thinned area was confined to approximately a 5 to 8 μm region in the middle of the 15 to 30 μm long section that was removed from the bulk

specimen. In all cases, the sample thicknesses were measured using Kossel-Möllenstedt fringes as described in section 2.3.1.1.

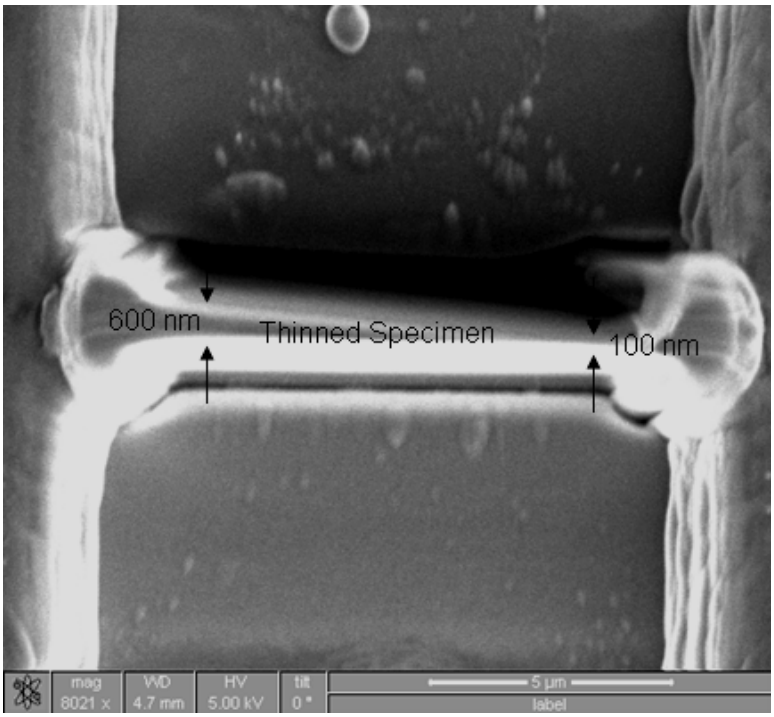

Figure 3.7 – Scanning electron microscopy (SEM) image of the top view of a TEM specimen thinned into a wedge shape.

The convergent beam electron diffraction (CBED) analysis was performed in an FEI Tecnai F20 TEM equipped with scanning and energy-filtering capabilities. The majority of the cross-sectional samples were cut such that the foil normal was approximately parallel to the <110> direction. Since there are no discernable HOLZ lines in this orientation, the sample was tilted approximately 5°, parallel to the SiGe/silicon interface (along the 004 Kikuchi band), to a <560> zone axis where the HOLZ lines are readily apparent. In some cases, the sample was tilted further to the <230> zone axis since this is the main zone axis used in much of the previous literature

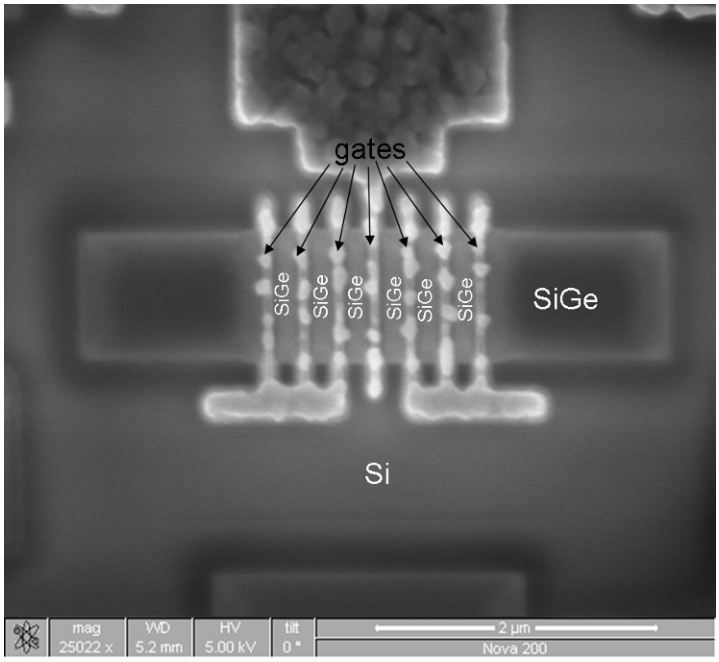

Figure 3.8 – SEM image of the top view of the MOSFET structure from a partially-processed wafer.

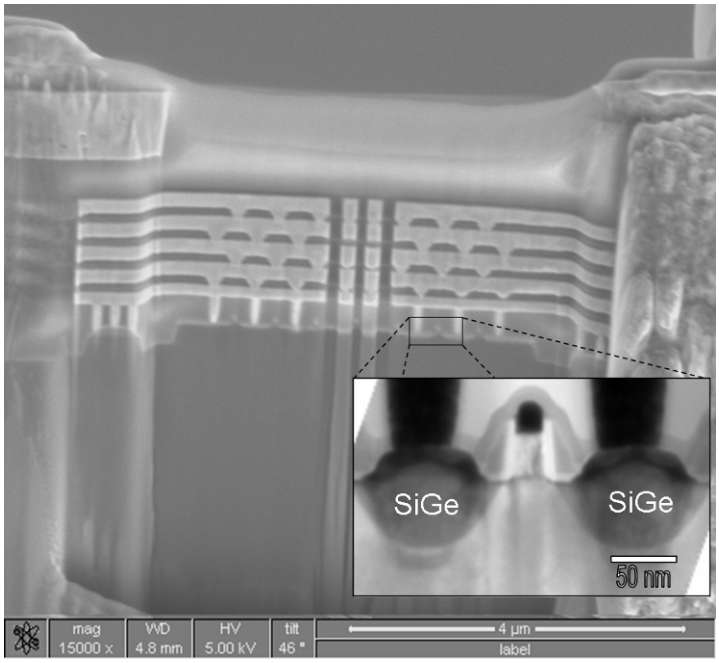

Figure 3.9 – SEM image of the side view of the MOSFET structure in the fully-processed wafer after FIB thinning. The inset is a TEM image showing the close-up of one gate.

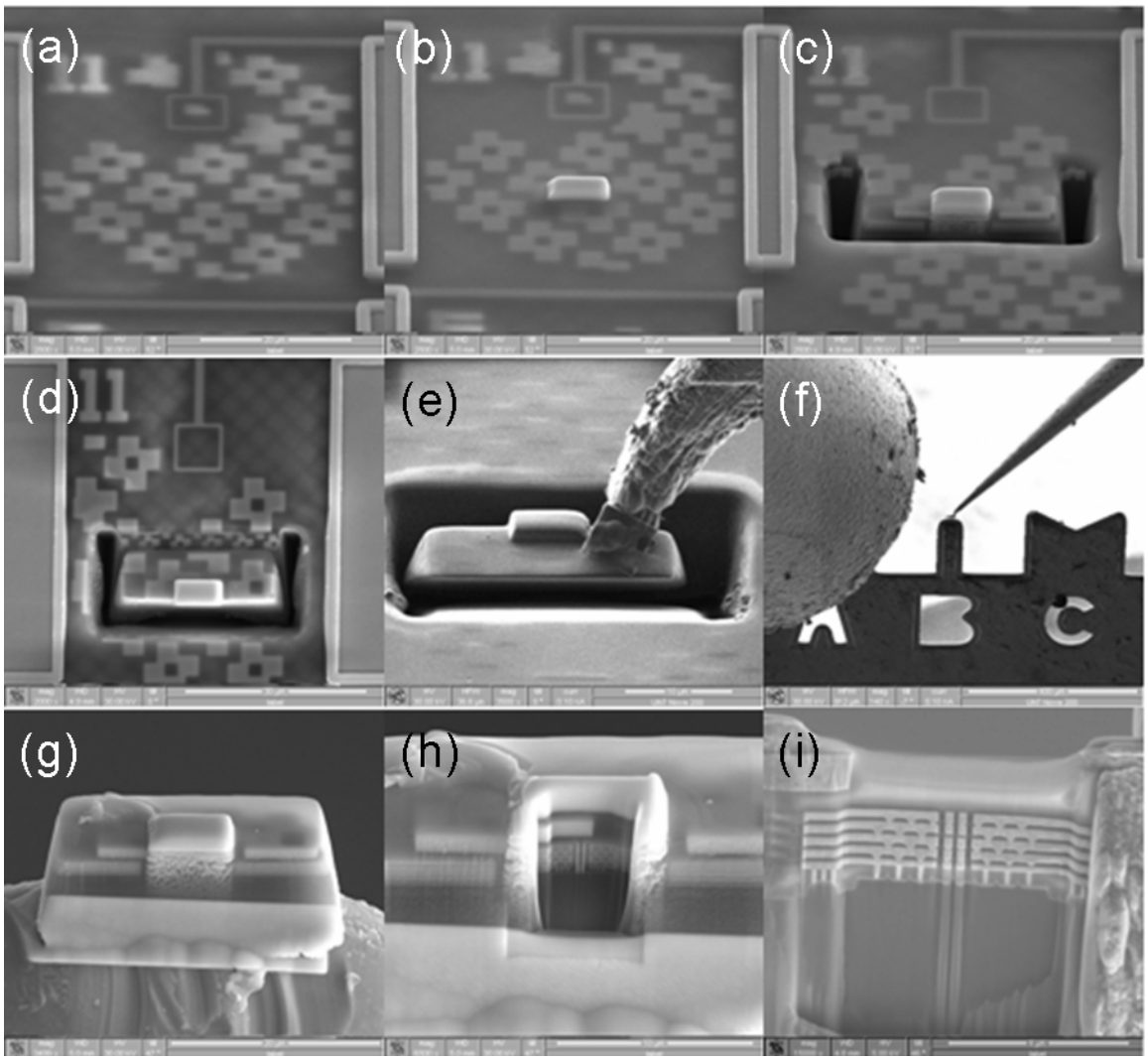

Figure 3.10 – The lift-out specimen preparation procedure for the MOSFET structures. (a) Device area before starting procedure. (b) Deposition of platinum. (c) Milling on three sides around the area of interest. (d) Wedge cut to free the specimen from the wafer. (e) Attachment of the micro-manipulator to the specimen with platinum. (f) Transfer of the specimen to a TEM grid. The needle for the platinum source can be seen on the left side of the figure. (g) The specimen after being attached to the TEM grid. (h) The specimen after milling to the MOSFET structures from one side. (i) The final TEM specimen.

on this subject. Energy-filtered CBED patterns were obtained in the scanning transmission electron microscopy (STEM) mode using a convergence angle of about 3°. A cross-sectional sample with a <100> foil normal was also prepared in order to compare planes from the same families with different orientations relative to the

SiGe/silicon interface. In this case, CBED patterns were collected from the <901> and <910> axes which are 6.3° from the <100>.

3.2 Patterned Wafers

The TEM lift-out method was used for preparation of the site-specific MOSFET samples. The geometry and dimensions of the removed sections are shown in Figures 3.8 and 3.9. Figure 3.10 illustrates the steps of the lift-out procedure for these specimens. CBED analysis was performed at the <230>, <340>, and <670> zone axes.

CHAPTER 4

RESULTS AND DISCUSSION

4.1 Blanket Wafers

4.1.1 X-Ray Diffraction

Prior to TEM specimen preparation, the structures of the bulk SiGe blanket wafers were measured using x-ray diffraction. Reciprocal space maps (RSMs) were constructed from ω - $\omega/2\theta$ scans performed around the 004, 113, and 224 peaks for the SiGe film and Si substrate. The reciprocal lattice values, q, along the real lattice directions are related to the system parameters by the following equations:

$$q_{[001]} = \frac{2\cos(\theta - \omega)\sin(\theta)}{\lambda} \qquad (4.1)$$

$$q_{[110]} = \frac{2\sin(\theta - \omega)\sin(\theta)}{\lambda} \qquad (4.2)$$

where λ is the x-ray wavelength and the angles are as shown in Figures 3.1 – 3.3. The results of the RSM scans are shown in Figures 4.1 - 4.6.

For each of the three scanned peak regions, the maximum intensity for the SiGe peak was directly below the Si peak. That is, the reciprocal lattice unit q has the same value in the [110] direction for the SiGe and Si. This means that the SiGe is perfectly lattice-matched to the Si on the (001) plane. The values for q in the [001] direction are smaller for the SiGe than for the Si, meaning that the SiGe is elongated in that direction compared to the Si. The real space lattice values for the SiGe for both wafers were

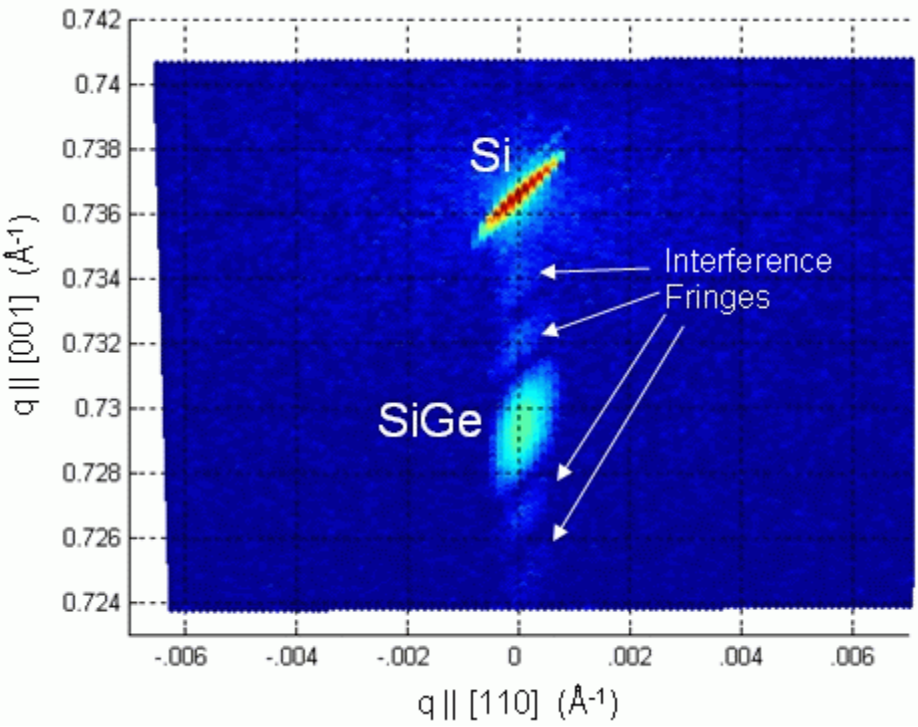

Figure 4.1 – RSM of the Si and SiGe (004) peaks for the SiGe01 blanket wafer.

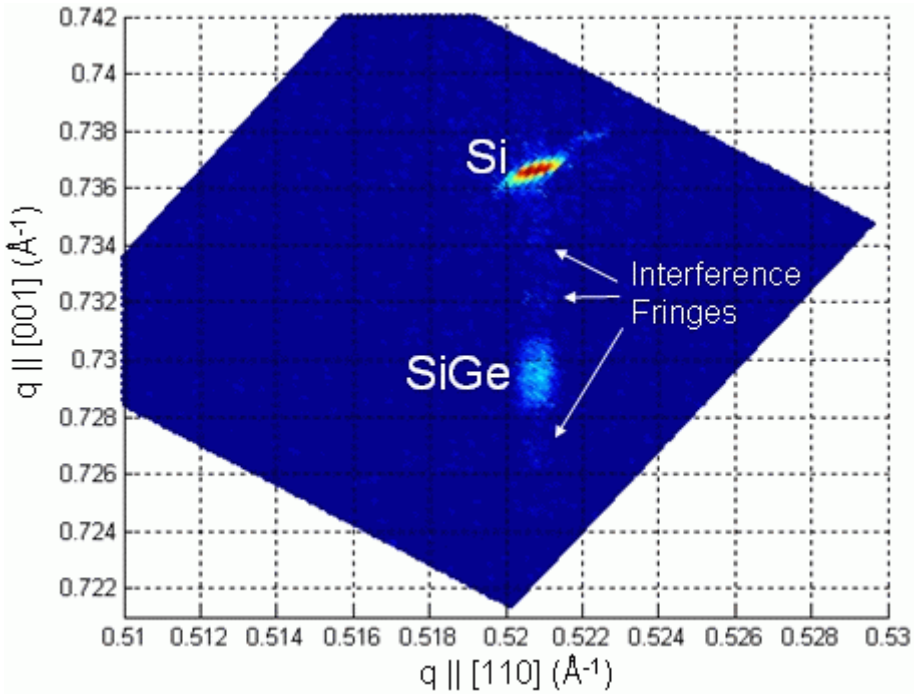

Figure 4.2 – RSM of the Si and SiGe (224) peaks for the SiGe01 blanket wafer.

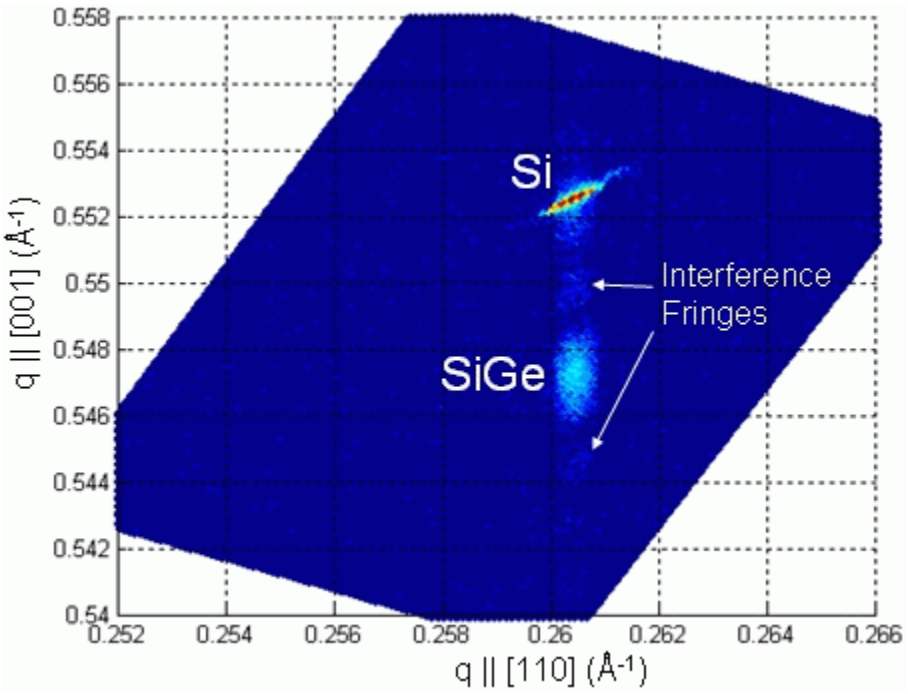

Figure 4.3 – RSM of the Si and SiGe (113) peaks for the SiGe01 blanket wafer.

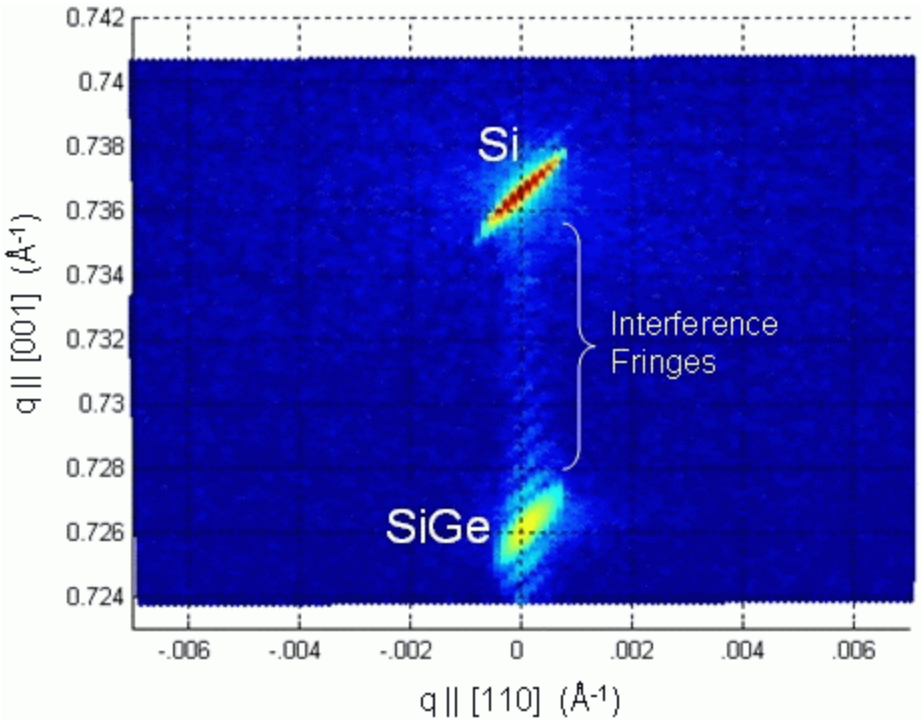

Figure 4.4 – RSM of the Si and SiGe (004) peaks for the SiGe02 blanket wafer.

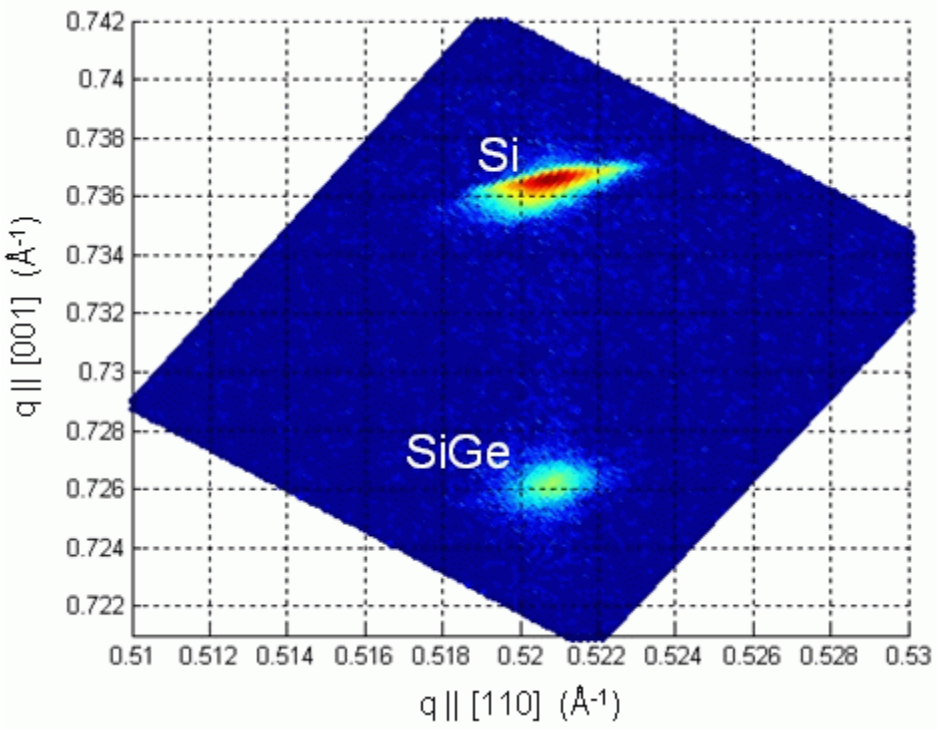

Figure 4.5 – RSM of the Si and SiGe (224) peaks for the SiGe02 blanket wafer.

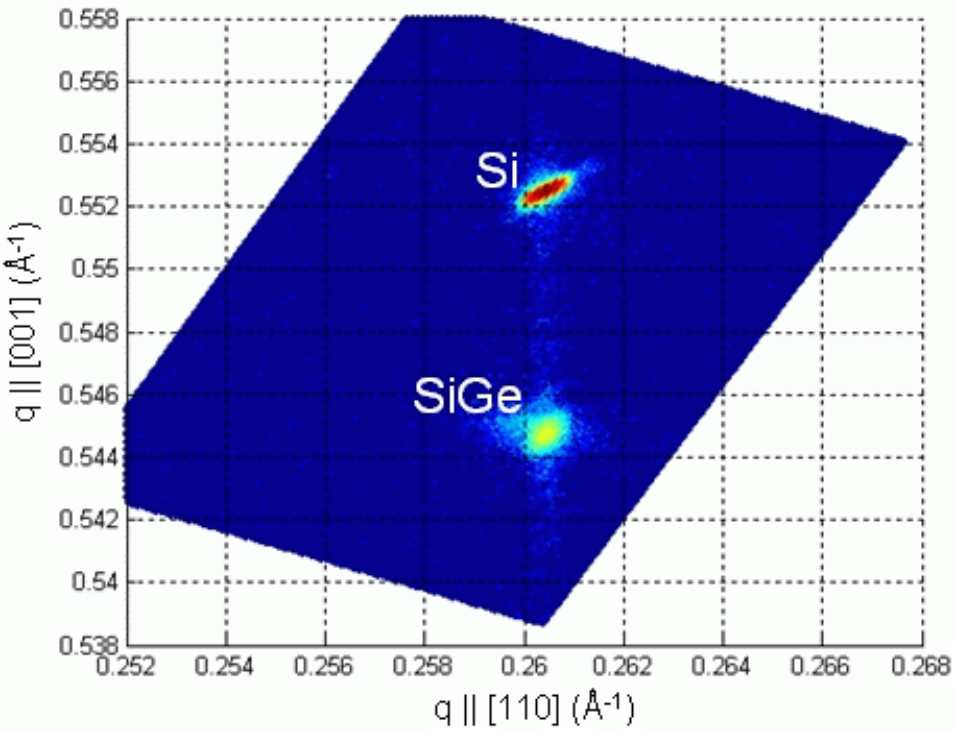

Figure 4.6 – RSM of the Si and SiGe (113) peaks for the SiGe02 blanket wafer.

calculated individually for each of the RSM scans. These results are shown in Table 4.1. From these, it is apparent that for both samples the SiGe is tetragonally distorted with the lower germanium content film being less distorted. Based on the lattice parameter calculations from these scans, the germanium content of the films can be determined using the elastic properties of silicon. It has been shown that the strain perpendicular to the interface for pseudomorphic growth of SiGe on silicon obeys the following relation:

$$\varepsilon_{\perp} = \kappa(0.00501x^2 + 0.03675x) \qquad (4.3)$$

where κ is the elastic constant determined by the stress state and x is the fractional amount of germanium [39]. In this case with a biaxial stress and (001) surface,

$$\kappa = 1 + 2\frac{C_{12}}{C_{11}} \qquad (4.4)$$

where C_{11} and C_{12} are the stiffness tensor values. For $Si_{1-x}Ge_x$ [40]:

$$C_{11} = 165.8 - 37.3x \text{ GPa} \qquad (4.5)$$

$$C_{12} = 63.9 - 15.6x \text{ GPa} \qquad (4.6)$$

From equations 4.3 through 4.6, SiGe01 has a composition of $Si_{.851}Ge_{.149}$ and SiGe02 has a composition of $Si_{.788}Ge_{.212}$. These are both close to the target compositions of 15 and 22% germanium, respectively.

Individual rocking curves of $\omega/2\theta$ scans were also collected (Figures 4.7 – 4.12). In these, in addition to the diffraction peaks from the SiGe and the silicon, there are peaks (interference fringes) which correspond to interference in the diffracted beams from the SiGe and silicon. The clarity of these fringes in both the rocking curves and the RSMs indicate a sharp interface between the SiGe and silicon and constant film

Table 4.1 – Values for the Si and SiGe peak positions from the reciprocal space map scans and the calculated lattice parameters based on those peak positions. The last two columns show the lattice parameter values determined from an average over all the scans.

	004 scan q[001] ($Å^{-1}$)	004 scan q[110] ($Å^{-1}$)	Calc. c (Å)	113 scan q[001] ($Å^{-1}$)	113 scan q[110] ($Å^{-1}$)	Calc. a (Å)	Calc. c (Å)	224 scan q[001] ($Å^{-1}$)	224 scan q[110] ($Å^{-1}$)	Calc. a (Å)	Calc. c (Å)	Avg. a (Å)	Avg. c (Å)
Si peak on SiGe01	0.7365	0.0000	5.4311	0.5524	0.2604	5.4308	5.4309	0.7365	0.5208	5.4308	5.4309	5.4309	5.4310
SiGe peak on SiGe01	0.7293	0.0001	5.4847	0.5469	0.2604	5.4309	5.4855	0.7294	0.5210	5.4288	5.4840	5.4299	5.4847
Si peak on SiGe02	0.7365	0.0000	5.4311	0.5524	0.2604	5.4308	5.4309	0.7365	0.5208	5.4308	5.4309	5.4309	5.4310
SiGe peak on SiGe02	0.7262	-0.0001	5.5081	0.5448	0.2605	5.4288	5.5066	0.7261	0.5207	5.4320	5.5089	5.4304	5.5079

thickness for both wafers. From these scans, the thickness of the SiGe film can be approximated by fitting with a dynamical diffraction simulation. From the RSMs and rocking curves SiGe01 has a thickness of 50nm and a composition of $Si_{.851}Ge_{.149}$ and SiGe02 has a thickness of 126 nm and a composition of $Si_{.788}Ge_{.212}$.

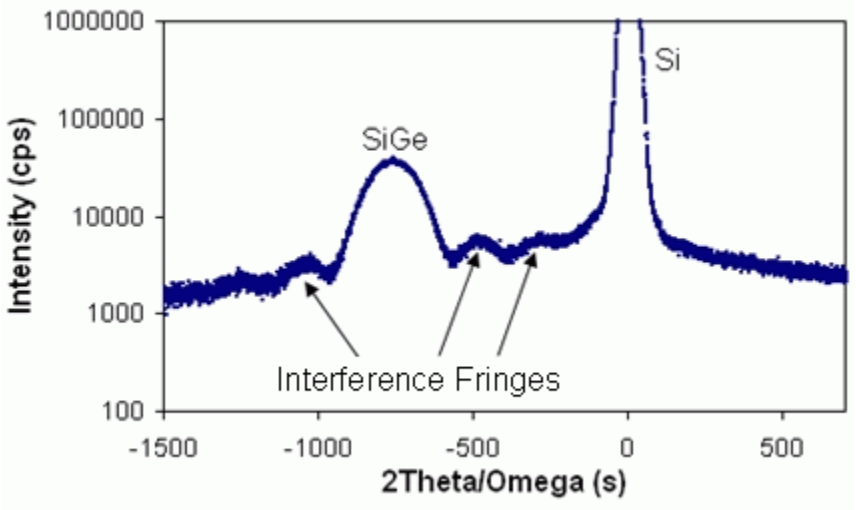

Figure 4.7 – 004 $\omega/2\theta$ rocking curve from SiGe01.

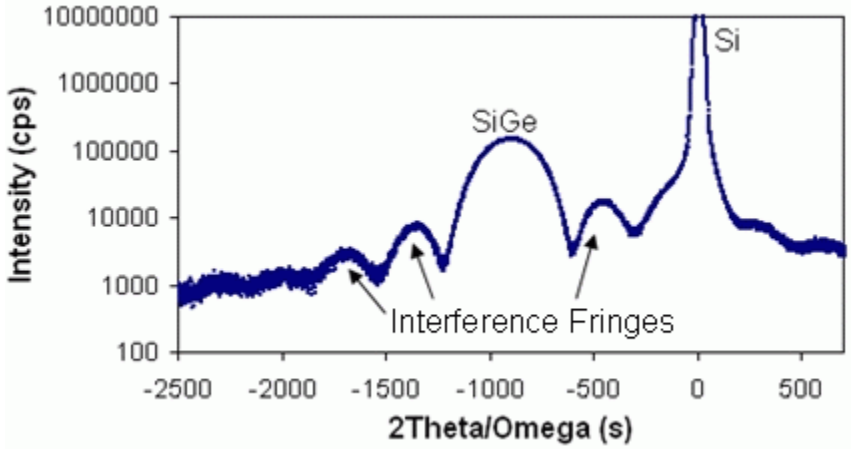

Figure 4.8 – 113 $\omega/2\theta$ rocking curve from SiGe01.

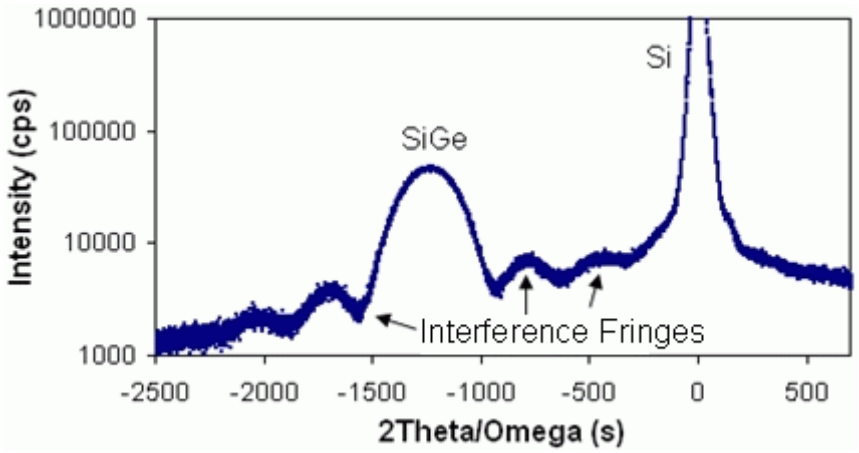

Figure 4.9 – 224 $\omega/2\theta$ rocking curve from SiGe01.

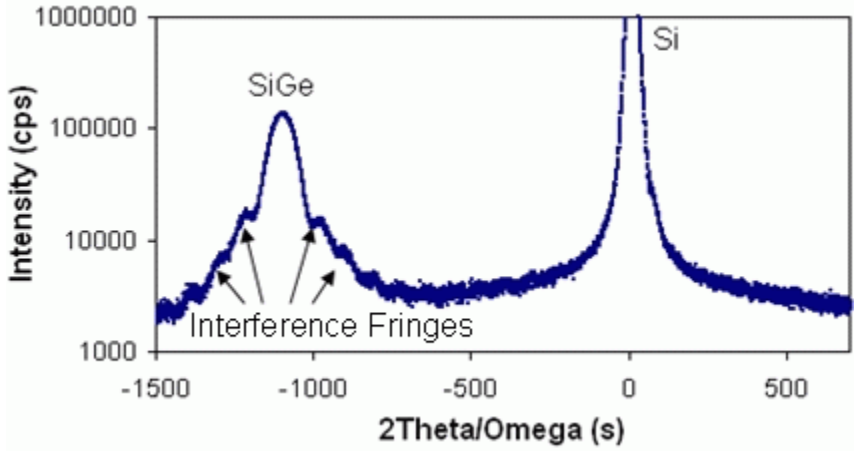

Figure 4.10 – 004 $\omega/2\theta$ rocking curve from SiGe02.

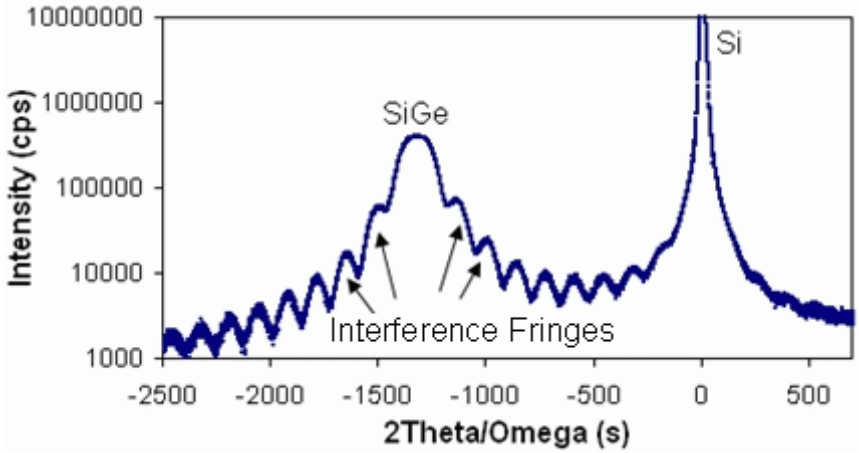

Figure 4.11 – 113 $\omega/2\theta$ rocking curve from SiGe02.

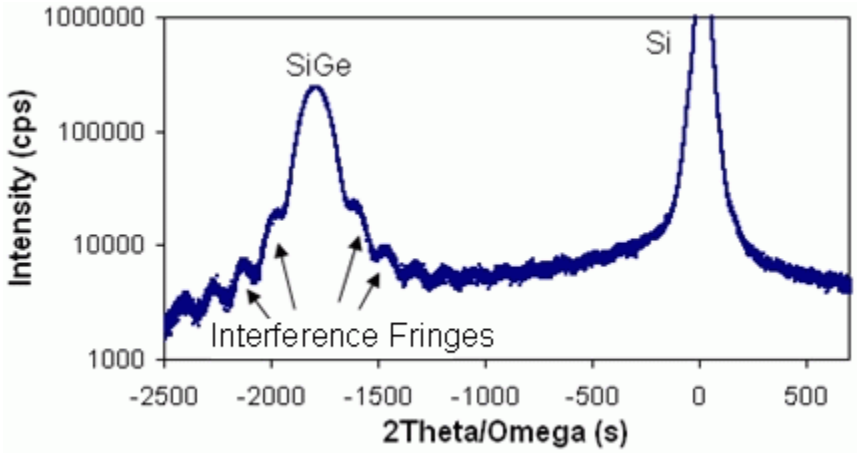

Figure 4.12 – 224 $\omega/2\theta$ rocking curve from SiGe02.

4.1.2 Transmission Electron Microscopy

4.1.2.1 Choice of Axis for Higher Order Laue Zone Line Analysis

For typical semiconductor devices, the obvious axis for HOLZ line analysis is <110> as that is the direction normal to the device structures. However, HOLZ line analysis cannot be performed along a <110> due to the spacing between reciprocal lattice Laue zones being too large to permit significant HOLZ diffraction in this orientation.

The equation for the radius of the n^{th} Laue zone ring is given by:

$$G_n = n \cdot H \sqrt{\frac{2}{nH\lambda} - 1} \qquad (4.7)$$

where G is the reciprocal lattice radius, n the Laue zone number, H the reciprocal lattice spacing parallel to the electron beam, and λ the electron beam wavelength. This geometry can be confirmed through application of the Pythagorean theorem to the

situation depicted in Figure 4.13. From this equation, the expected radii of the first five HOLZ in silicon for several zone axes are listed in Table 4.2. For a <110> axis,

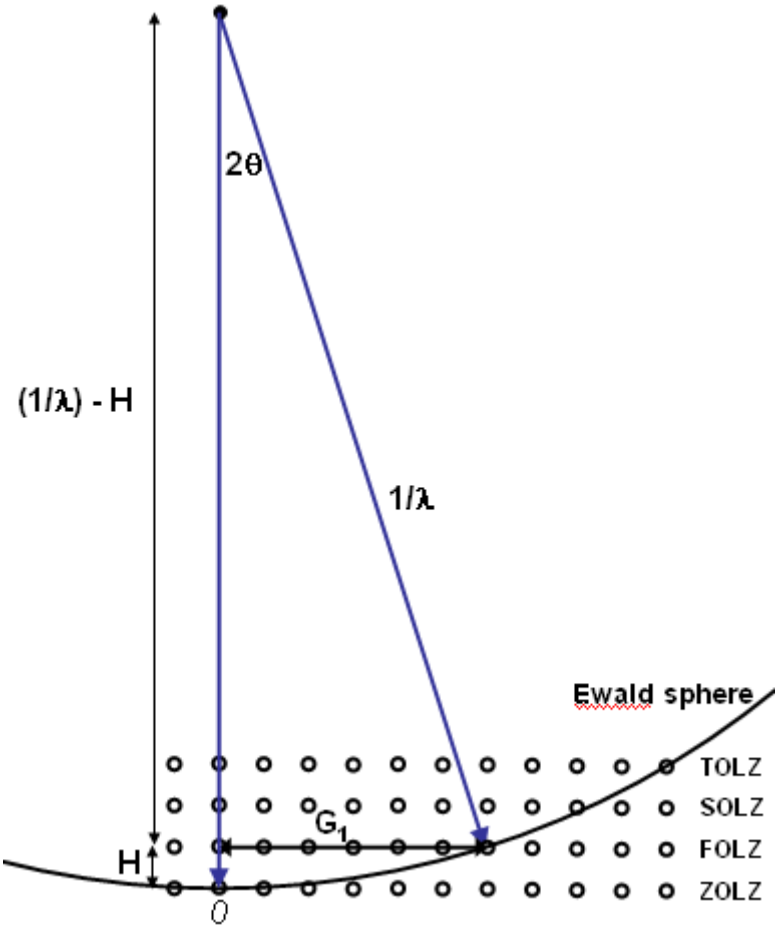

Figure 4.13 – Schematic of reciprocal space showing the radius of diffraction (G_1) for the first order Laue zone (FOLZ). H is the reciprocal lattice spacing, λ is the electron beam wavelength, and 2θ is the angle between the incident and diffracted beams.

scattering out to very large angles is required to meet the diffraction conditions for the second order Laue zone. The second order Laue zone is the first allowed set of HOLZ reflections in this orientation as all the first order Laue zone reflections are forbidden along this direction for the diamond cubic structure.

Table 4.2 – The reciprocal lattice radii (G) in nm^{-1} for several incident zone axes. H is the reciprocal lattice spacing. The radii highlighted in red are those HOLZ reflections that are forbidden by the diamond cubic structure. The radii highlighted in orange are those where HOLZ reflections from these zones were not visible in the CBED images.

direction			H (nm^{-1})	G_1 (nm^{-1})	G_2 (nm^{-1})	G_3 (nm^{-1})	G_4 (nm^{-1})	G_5 (nm^{-1})
1	**0**	**0**	1.84	38.26	54.04	66.11	76.25	85.15
1	**1**	**0**	1.30	32.18	45.48	55.65	64.21	71.73
1	**1**	**1**	1.06	29.09	41.11	50.31	58.05	64.86
1	**2**	**0**	0.82	25.60	36.19	44.30	51.12	57.13
1	**3**	**0**	0.58	21.53	30.44	37.27	43.02	48.08
2	**3**	**0**	0.51	20.17	28.51	34.91	40.29	45.03
3	**4**	**0**	0.37	17.13	24.21	29.65	34.23	38.26
4	**5**	**0**	0.29	15.13	21.40	26.20	30.25	33.82
5	**6**	**0**	0.24	13.70	19.38	23.73	27.40	30.62
6	**7**	**0**	0.20	12.61	17.84	21.84	25.22	28.19

The expected radii from this table can be compared to the HOLZ deficit lines that are visible in the central disk of the CBED patterns from each of these directions (Figures 4.14 - 4.16). From this comparison, it can be seen that HOLZ lines from zones with radii greater than approximately 32 nm^{-1} are not visible in the experimental CBED

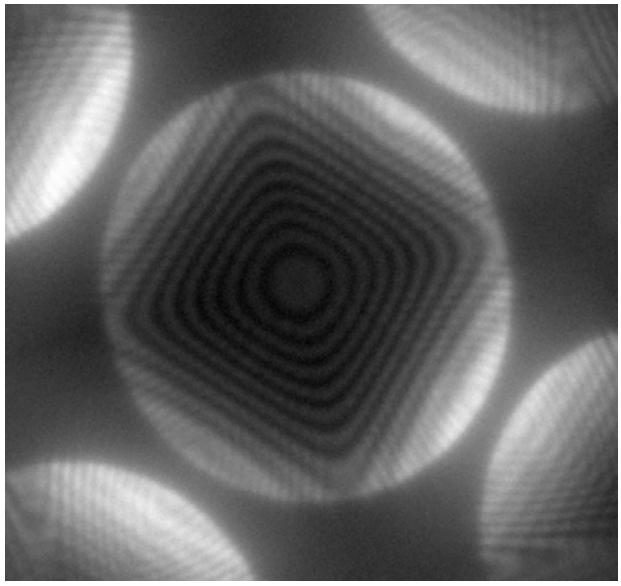

Figure 4.14 – Experimental CBED pattern from a <100> axis in silicon.

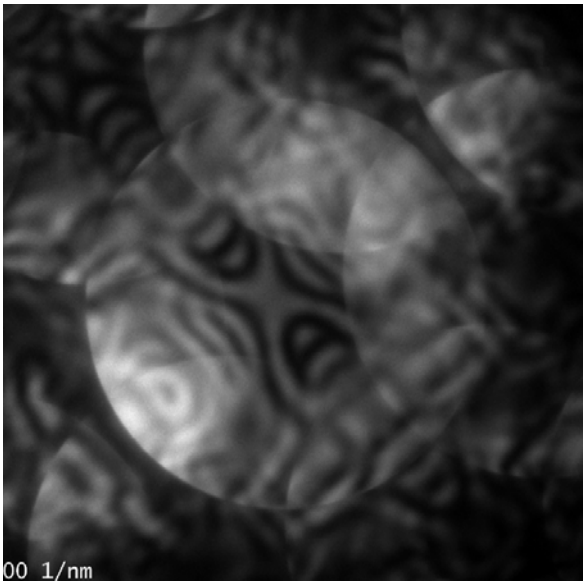

Figure 4.15 – Experimental CBED pattern from a <110> axis in silicon.

patterns. For example, in the <230> zone axis CBED pattern, first and second order Laue zone deficit lines are visible, whereas third order Laue zone deficit lines are not. This cutoff point corresponds to a scattering angle of roughly 4.6° (2θ in Figure 4.13).

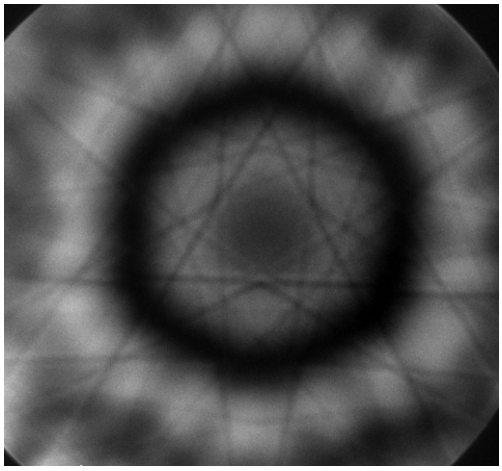

(a) Experimental <111> axis.

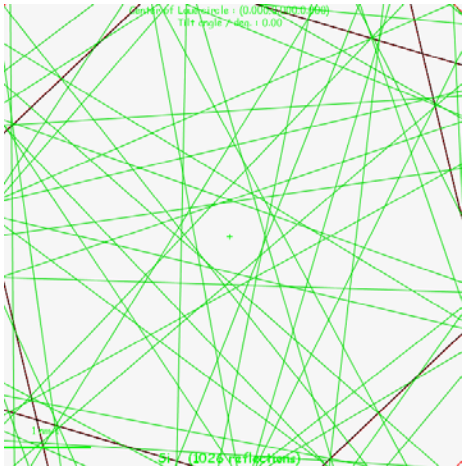

(b) Simulated <111> axis.

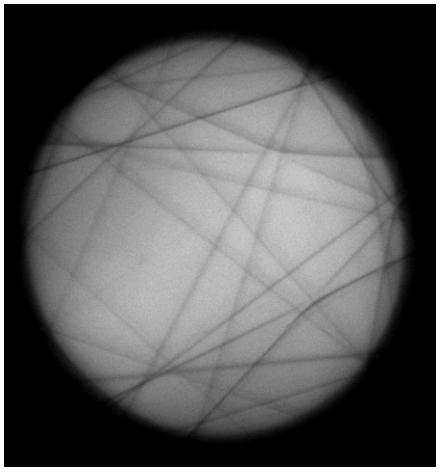

(c) Experimental <120> axis.

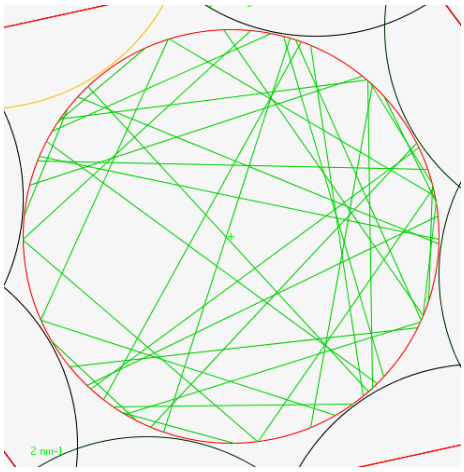

(d) Simulated <120> axis.

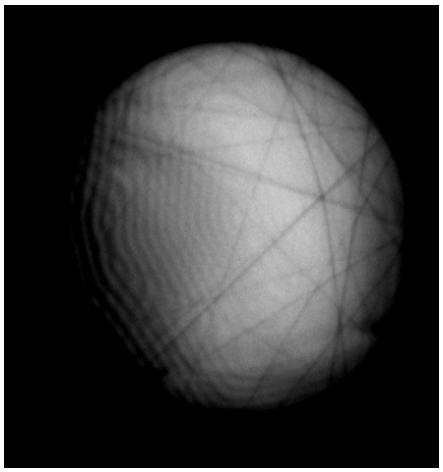

(e) Experimental <130> axis.

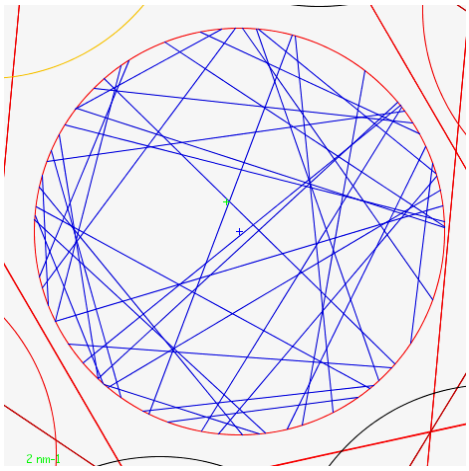

(f) Simulated <130> axis.

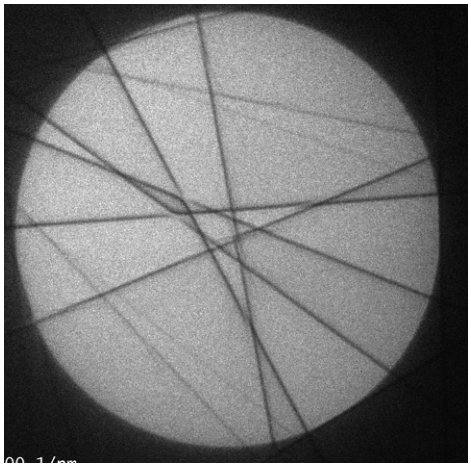

(g) Experimental <230> axis.

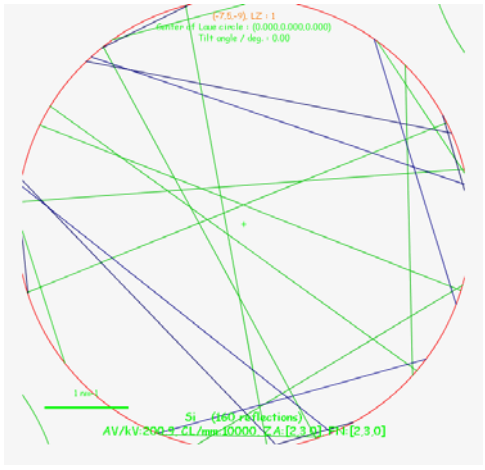

(h) Simulated <230> axis.

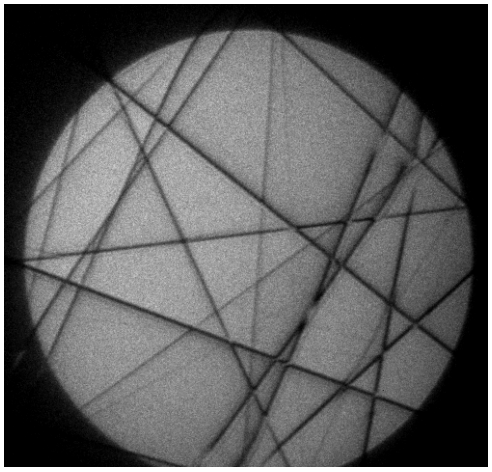

(i) Experimental <340> axis.

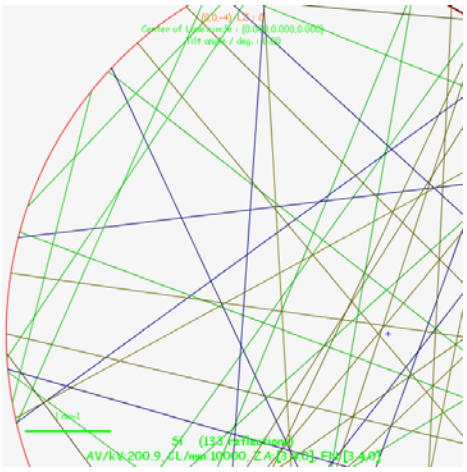

(j) Simulated <340> axis.

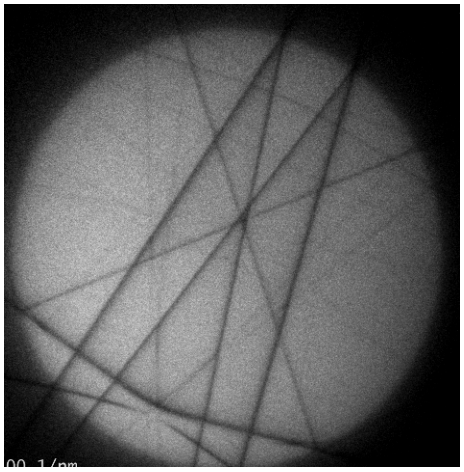

(k) Experimental <450> axis.

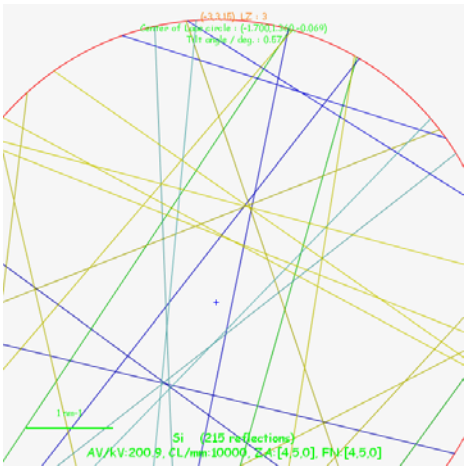

(l) Simulated <450> axis.

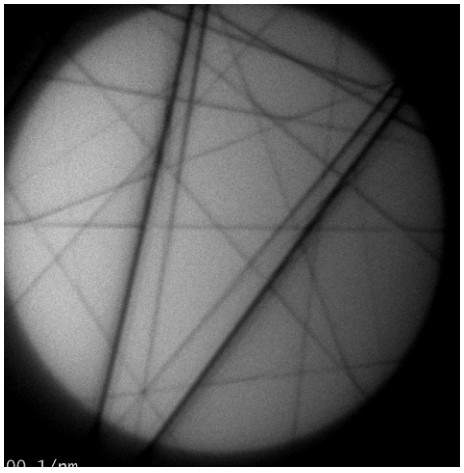

(m) Experimental <560> axis.

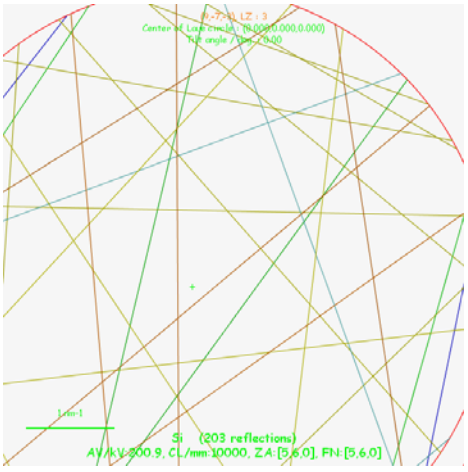

(n) Simulated <560> axis.

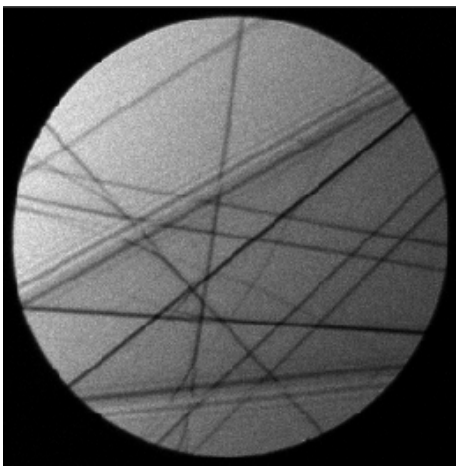

(o) Experimental <670> axis.

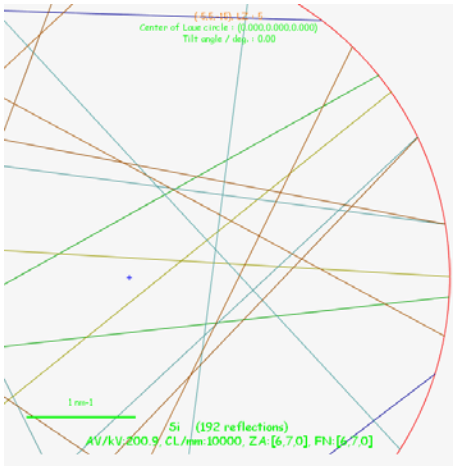

(p) Simulated <670> axis.

Figure 4.16 – Experimental and kinematically simulated CBED patterns for silicon with a 200 kV accelerating voltage from several axes. The deficit lines for the different Laue zones appear in the following colors in the simulation images: 1st order – green, 2nd order – dark blue, 3rd order – yellow, 4th order – light blue, 5th order – red.

Each zone axis therefore has different sensitivities to different lattice parameters and also has different spatial resolution. The former issue will be addressed for each of the axes in a later section, the latter issue is addressed next.

4.1.2.2 Spatial Resolution

For two-dimensional features such as films, tilting parallel to the film will not affect the spatial resolution because the stresses from the film are uniformly applied to the adjacent layers. For this reason, early work using HOLZ lines for strain measurements in Si/SiGe multilayers was concerned primarily with finding axes that had high sensitivities to changes in strain and minimal dynamical effects for ease of simulation. Simulating HOLZ line patterns for measuring strain will be discussed in more detail later.

The two axes that were found to work best were the <130> and <120> [41-45]. These were used to measure the strain in silicon under nitride films [43], in heterostructures [42-43], around shallow trench isolation structures [41,44], and in silicon films [45].

For measuring strain around three-dimensional structures, such as MOSFETs, it was recognized that such high tilts from the primary <110> axis in silicon-based devices could not be used for strain measurement. At a <130> axis the lateral distance the beam traverses through a 300nm thick specimen (along the measurement axis) relative to the <110> axis is 134 nm. For the <120> axis, it is 95 nm. Therefore the <230> axis became the main direction for strain analysis around three-dimensional structures using HOLZ lines. As the features and the distance between features continue to decrease, however, even smaller tilts from <110> are necessary to attain the desired resolution. This is shown in Table 4.3. A schematic of this resolution limitation is shown in Figure 4.17.

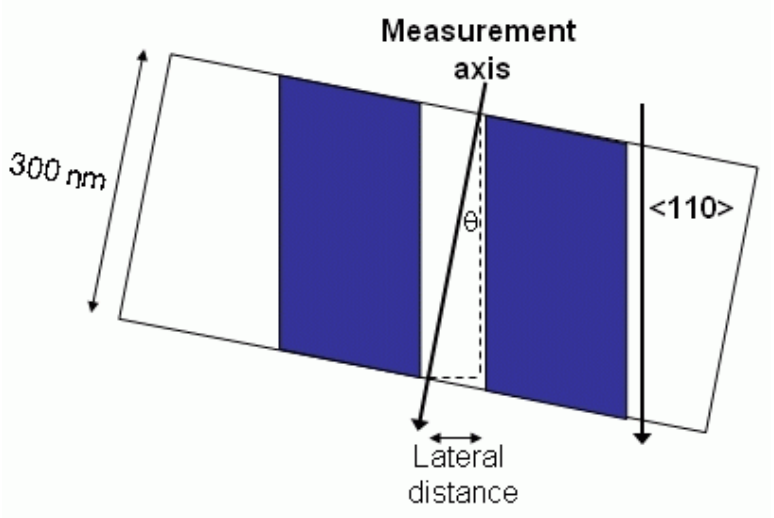

Figure 4.17 – Schematic of the relationship between the measurement axis angle (θ) relative to the <110> direction and the lateral resolution between two structures (in blue).

Table 4.3 – Several zone axes with the angles relative to <110> and their lateral resolution through a 300 nm thick specimen, assuming no beam spreading.

Axis	Angle to <110>	Lateral distance through 300 nm thick specimen
<130>	26.57	134 nm
<120>	18.43	95 nm
<230>	11.31	59 nm
<340>	8.13	42 nm
<450>	6.34	33 nm
<560>	5.19	27 nm
<670>	4.40	23 nm

Additionally, it was shown in the previous section that for the 3° convergence angle used in this research, additional scattering leads to an ultimate scattering angle of about 4.6°. The result of this is a 12 nm radial spreading of the beam through a 300 nm thick specimen.

4.1.2.3 HOLZ Line Measurements – Thickness and Distance Effects

For the SiGe01 and SiGe02 blanket wafers, detailed studies of the HOLZ line patterns as a function of specimen thickness and distance from the SiGe/silicon interface were carried out. These were performed at two zone axes slightly off of a <110> direction: a <560> axis and a <230> axis.

The specimens were prepared with three different techniques as described in the Experimental Procedure section. Typical CBED patterns are shown in Figures 4.18 and 4.19. As can be seen, the HOLZ lines exhibit splitting, the magnitude of which was found to depend on distance from the SiGe layer and the specimen thickness. As a basis for comparison of the splitting behavior, the degree of splitting of the $\bar{1}17$ HOLZ line was measured. Figure 4.20 shows the $\bar{1}17$ HOLZ line from the <560> axis in the

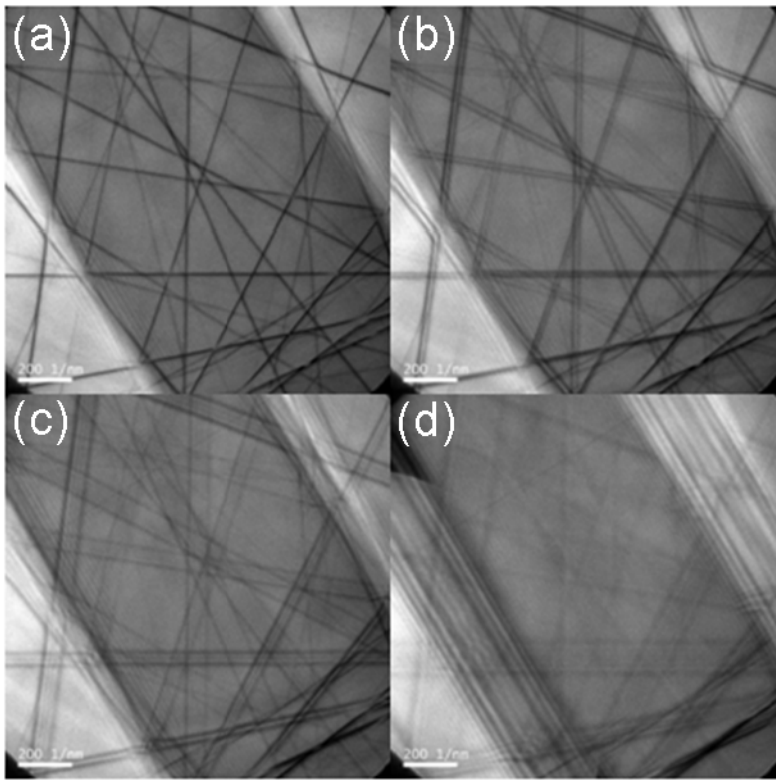

Figure 4.18 – HOLZ line patterns collected from a <230> axis in a 412 nm thick SiGe01 specimen (a) 400 nm from the SiGe/silicon interface, (b) 300 nm from the interface, (c) 200 nm from the interface, and (d) 100 nm from the interface.

split and unsplit conditions. The degree of splitting of this line is plotted as a function of both specimen thickness and distance from the SiGe/silicon interface for both blanket wafers in Figures 4.21 - 4.24 for the <560> zone axis, which is ~5° from the <110> and parallel to the SiGe/silicon interface. For both the <560> and <230> zone axes, it is clear that the amount of splitting decreases with increasing distance from the Si/SiGe interface and with decreasing thickness. It is also noted that not all HOLZ lines are split to the same extent; in fact, the lines that show the largest separation at a given position, correspond to planes that more closely parallel the Si/SiGe interface. The implications of this finding will be discussed further below.

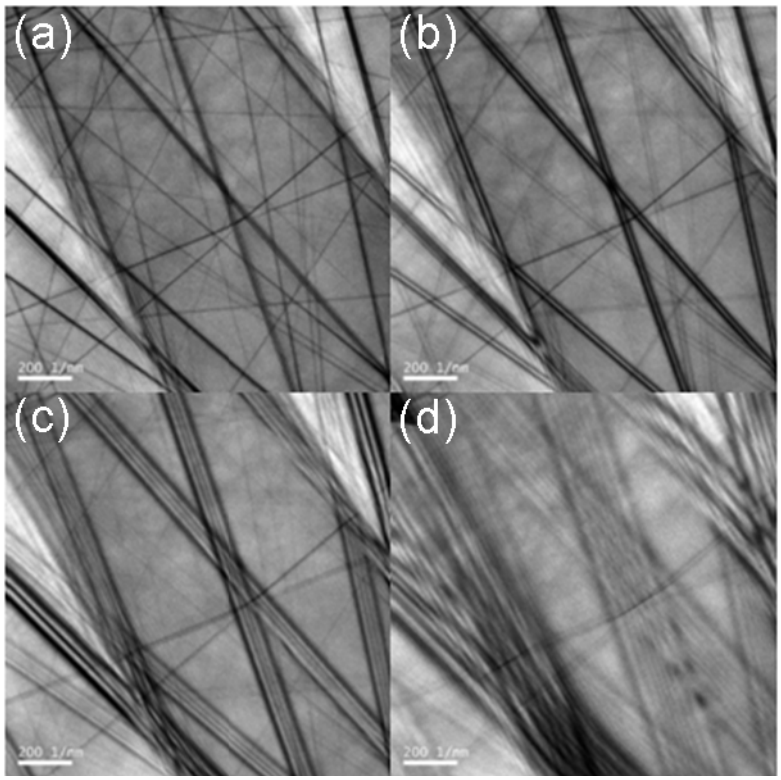

Figure 4.19 – HOLZ line patterns collected from a <560> axis in a 465 nm thick SiGe01 specimen (a) 400 nm from the SiGe/silicon interface, (b) 300 nm from the interface, (c) 200 nm from the interface, and (d) 100 nm from the interface.

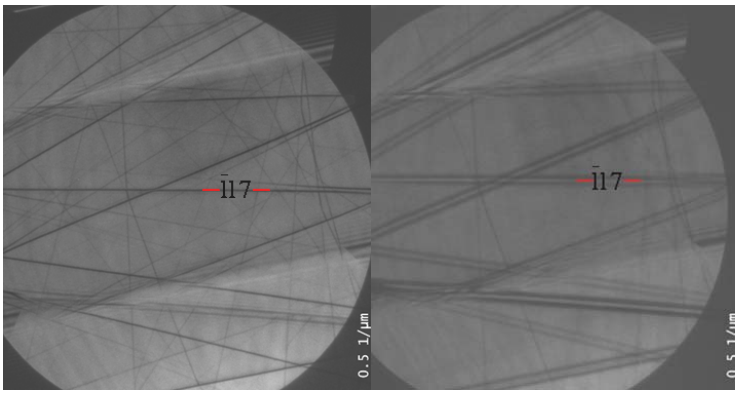

Figure 4.20 – <560> CBED pattern showing the $\bar{1}17$ HOLZ line (a) in the unsplit condition and (b) exhibiting splitting.

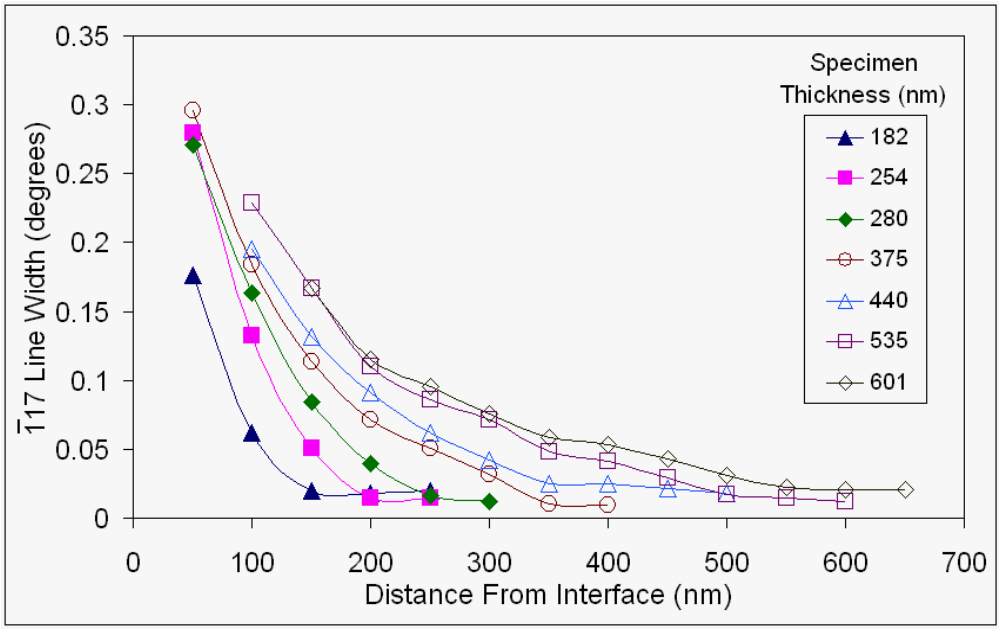

Figure 4.21 – Width of the split $\bar{1}17$ HOLZ line in <560> CBED patterns from SiGe01 as a function of distance from the SiGe/silicon interface for several specimen thicknesses.

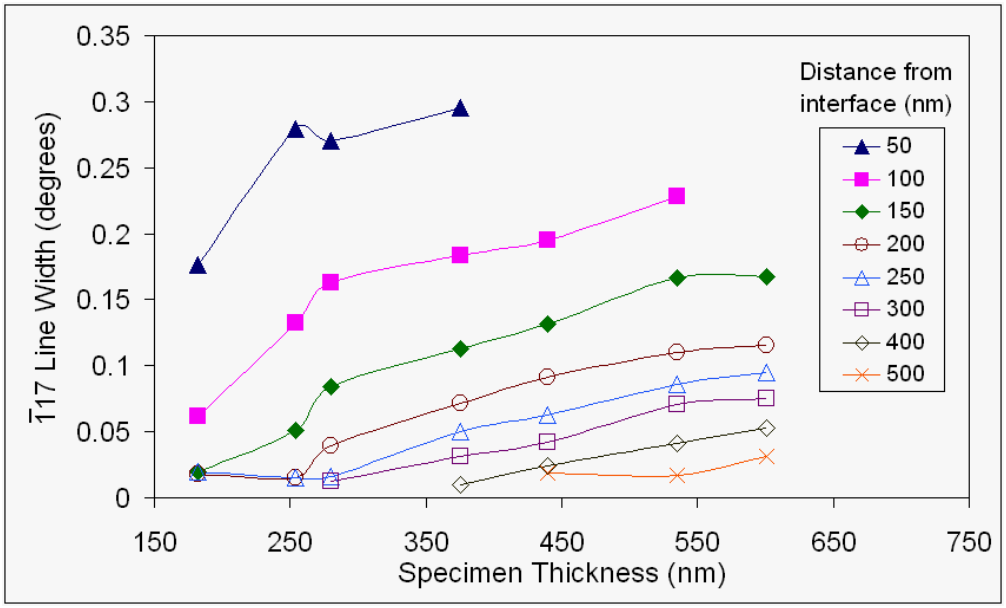

Figure 4.22 – Width of the split $\bar{1}17$ HOLZ line in <560> CBED patterns from SiGe01 as a function of specimen thickness for several distances from the SiGe/silicon interface.

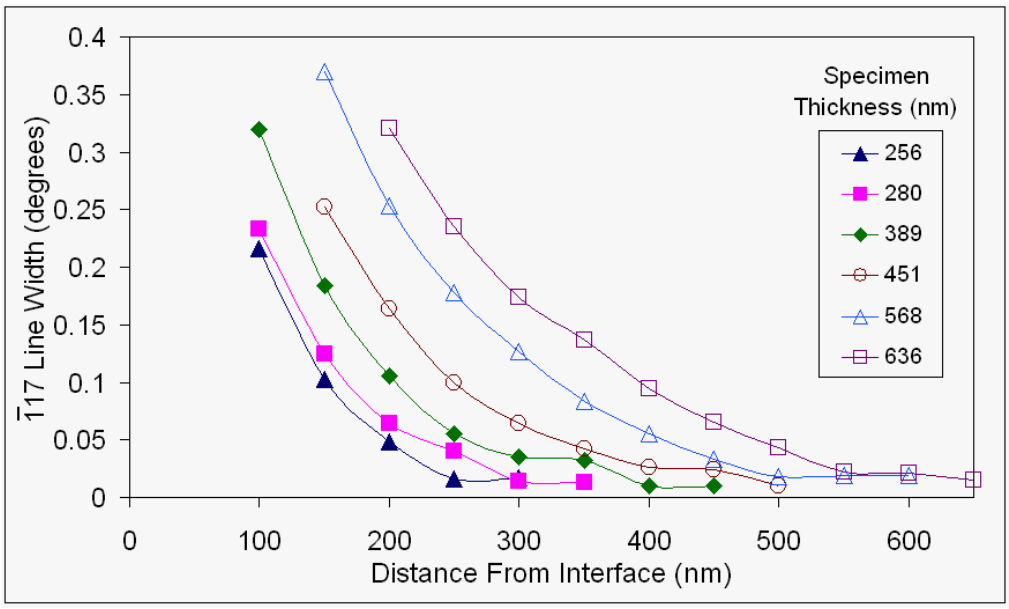

Figure 4.23 – Width of the split $\bar{1}17$ HOLZ line in <560> CBED patterns from SiGe02 as a function of distance from the SiGe/silicon interface for several specimen thicknesses.

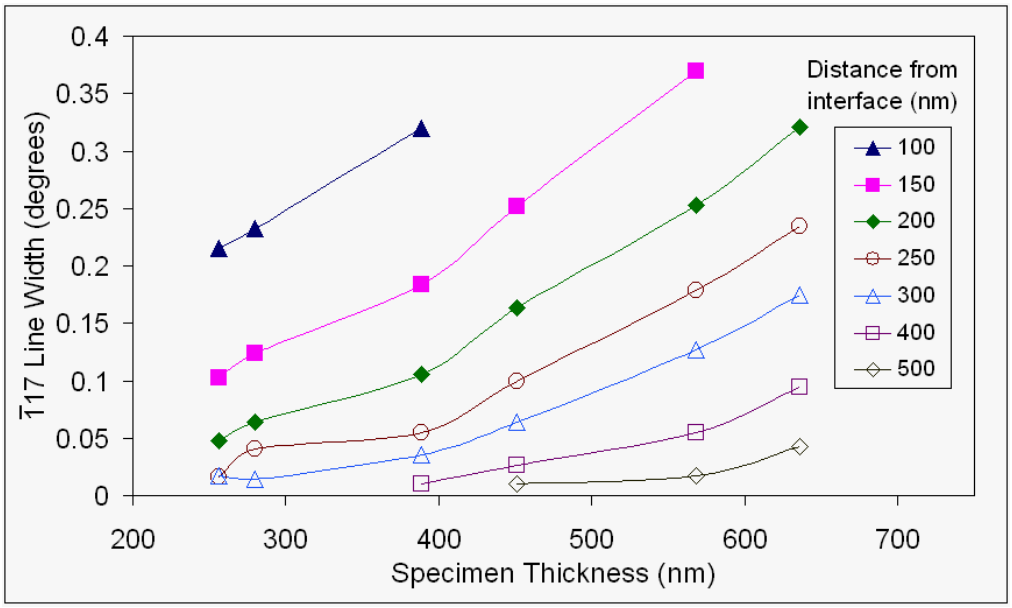

Figure 4.24 – Width of the split $\bar{1}17$ HOLZ line in <560> CBED patterns from SiGe02 as a function of specimen thickness for several distances from the SiGe/silicon interface.

Finally, it is also observed that the HOLZ lines that split do so symmetrically about the original position of the unsplit line. However, no measurable shifting of the

HOLZ line positions/intersections was observed, regardless of thickness or distance from the interface.

4.1.2.4 Causes of Higher Order Laue Zone Line Splitting

HOLZ line splitting can arise from several causes including strain gradients, dislocations, and stress relaxation [46-49]. For line splitting caused by dislocations, the splitting is localized to specimen regions around the dislocation. The HOLZ line splitting observed here was not confined to localized regions in the specimen, nor were dislocations observed in the areas from which the patterns were collected. The strain in the blanket wafer samples results from the forcing the SiGe to lattice match the silicon in the (001) plane. Tilting parallel to this plane, such as was performed here, should not cause the electron beam to pass through any appreciable strain gradients due to the lattice mismatch. With neither dislocations nor strain gradients being the observed source, it is apparent that the splitting of the HOLZ lines in this case indicates stress relaxation. Berbezier et al. [48] and Clement et al. [49] have observed similar HOLZ line splitting behavior but have attributed it to different relaxation behaviors. Berbezier et al. have suggested that the relaxation they observed occurred normal to the substrate surface, with the splitting resulting from changes in tetragonal distortion of the SiGe through the specimen thickness. Clement et al. have explained the behavior of their NiSi on silicon system as a relaxation in the thinned direction of the specimen, resulting in a rotational displacement. The HOLZ line splitting is then a result of the electron beam sampling slightly different orientations of the crystal lattice as it passes through the thickness of the specimen. In the present research, the lack of relative HOLZ line shifting and the symmetrical splitting about the original line position suggest a rotational

relaxation behavior. The next section discusses further experimentation that was performed to confirm this idea.

4.1.2.5 Confirmation of Rotational Relaxation

When initially deposited on the silicon wafer, the SiGe, which when unstrained has a slightly larger lattice parameter than silicon, is tetragonally distorted from its preferred diamond cubic structure with the elongated direction being orthogonal to the wafer while being in compression parallel to the plane of the wafer/blanket interface as shown by the XRD reciprocal space map data.

Several researchers have investigated surface relaxation effects in SiGe/silicon systems [50-52]. Treacy and Gibson [50] have shown that surface relaxation in compositionally-modulated crystalline materials can result in significant local bending of the lattice especially approaching interfaces. Their model is an application of linear elastic theory for anisotropic cubic materials. Since they looked at structures with repeating composition oscillations, the relaxation in the layers was evaluated based on the ratio of the specimen thickness to the period of the structure. It was found that thicknesses on the order of the composition modulation wavelength led to the most significant bending of planes. A similar behavior has been shown for SiGe layers on silicon mesas [52].

It is therefore apparent that the thinning of a blanket wafer specimen to make a TEM foil may allow the constrained epitaxial layer to relax in the thinned direction. This relaxation of the SiGe in the thinned direction, while still being epitaxial with the underlying silicon, may result in the rotational displacement of the silicon.

In order to verify that rotational displacement of the silicon in the thinned direction is the cause of the HOLZ line splitting, the splitting for the lines corresponding to particular planes can be compared. For this type of relaxation, it would be expected that the planes orthogonal to the [001] direction (parallel to the SiGe/silicon interface) would be affected the greatest and those planes parallel to the [001] direction would be affected the least. Figure 4.25 shows the relationship of these directions and planes for thinning along a [110] direction.

One test of this was an analysis of the HOLZ line splitting on a <100> cross-sectional specimen prepared from the SiGe01 specimen. For this geometry, symmetric zone axes near the [100] zone axis were compared, the [910] and [901] zone axes, both ~6° from the [100] zone axis. These axes have the same families of planes but the planes are oriented 90° from each other. For both of these zone axes, the HOLZ lines corresponding to the planes nearly parallel to the SiGe/silicon interface exhibited

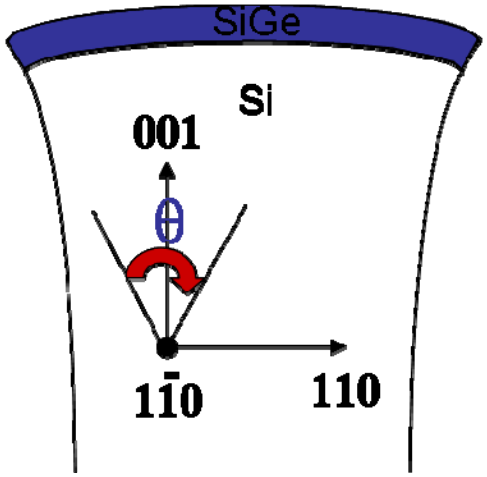

Figure 4.25 – The coordinate system for the blanket wafer geometry showing rotational relaxation about an angle θ for a specimen thinned along a [110] direction.

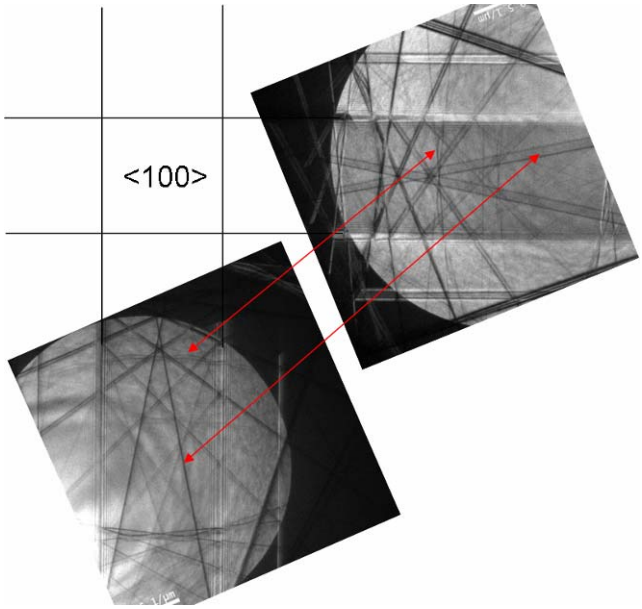

Figure 4.26 – CBED patterns from the [901] and [910] axes showing their relationship to each other. The arrows point to planes from the same family. In both cases, the HOLZ lines for planes most nearly parallel to the SiGe/silicon interface exhibited the greatest splitting while those nearly perpendicular to the interface exhibited little splitting.

splitting, while those at high angles to the interface did not (Figure 4.26).

Additionally, for pure rotational relaxation in the thinned direction, the degree of splitting can be calculated. The matrix for rotation of a plane by an angle θ about the $[1\bar{1}0]$ zone axis (as depicted for the blanket wafer schematic in Figure 4.25) is given by:

$$\begin{bmatrix} \frac{1}{2}+\frac{1}{2}\cos\theta & -\frac{1}{2}+\frac{1}{2}\cos\theta & \frac{\sqrt{2}}{2}\sin\theta \\ -\frac{1}{2}+\frac{1}{2}\cos\theta & \frac{1}{2}+\frac{1}{2}\cos\theta & \frac{\sqrt{2}}{2}\sin\theta \\ -\frac{\sqrt{2}}{2}\sin\theta & -\frac{\sqrt{2}}{2}\sin\theta & \cos\theta \end{bmatrix} \qquad (4.8)$$

By comparing the angular distance between the normal vectors for a given plane before and after this rotation, the anticipated degree of splitting can be calculated. This

is shown graphically for a 0.08° rotation about the $[1\bar{1}0]$ axis for several planes in Figure 4.27. In order to compare the calculated degree of splitting to that experimentally observed, the degree of splitting was measured for several planes in a <560> CBED pattern from an approximately 330 nm thick specimen of the SiGe02 wafer shown in Figure 4.28. This pattern was taken at a distance of 200 nm from the SiGe/silicon interface. For the calculated values, the measured degree of splitting of the $\bar{1}17$ HOLZ line was used as the basis from which the other split HOLZ line values were calculated. The results of this comparison are shown in Table 4.4. The good agreement of the calculated and experimental values indicates that the observed relaxation is indeed a rotational relaxation occurring in the thinned direction. Additionally, since the HOLZ lines that split do so symmetrically about the original position of the unsplit line, it can be inferred that the relaxation is also symmetric, i.e. relaxation occurs to the same extent on both sides of the thinned specimen.

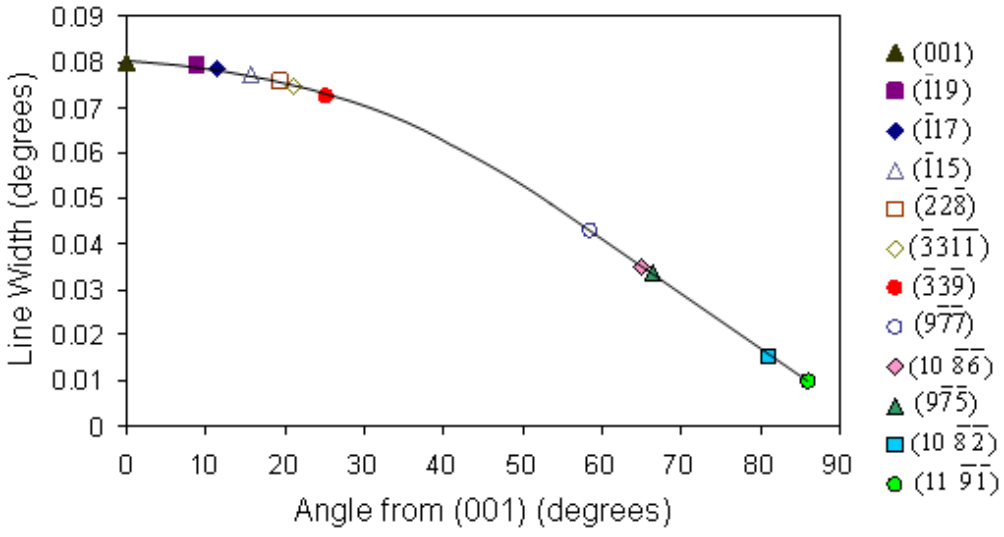

Figure 4.27 – Calculated degree of HOLZ line splitting versus planar angle from (001) for a 0.08° rotation about the $[1\bar{1}0]$ axis.

Based on the above discussion, the curves in Figures 4.21– 4.24 therefore show the rotational behavior of the thinned specimens as a function of specimen thickness and distance from the interface. Since these reflect a physical phenomenon that the material is undergoing, it should be possible to calculate physical values associated with these relaxations and compare them to theoretically expected values.

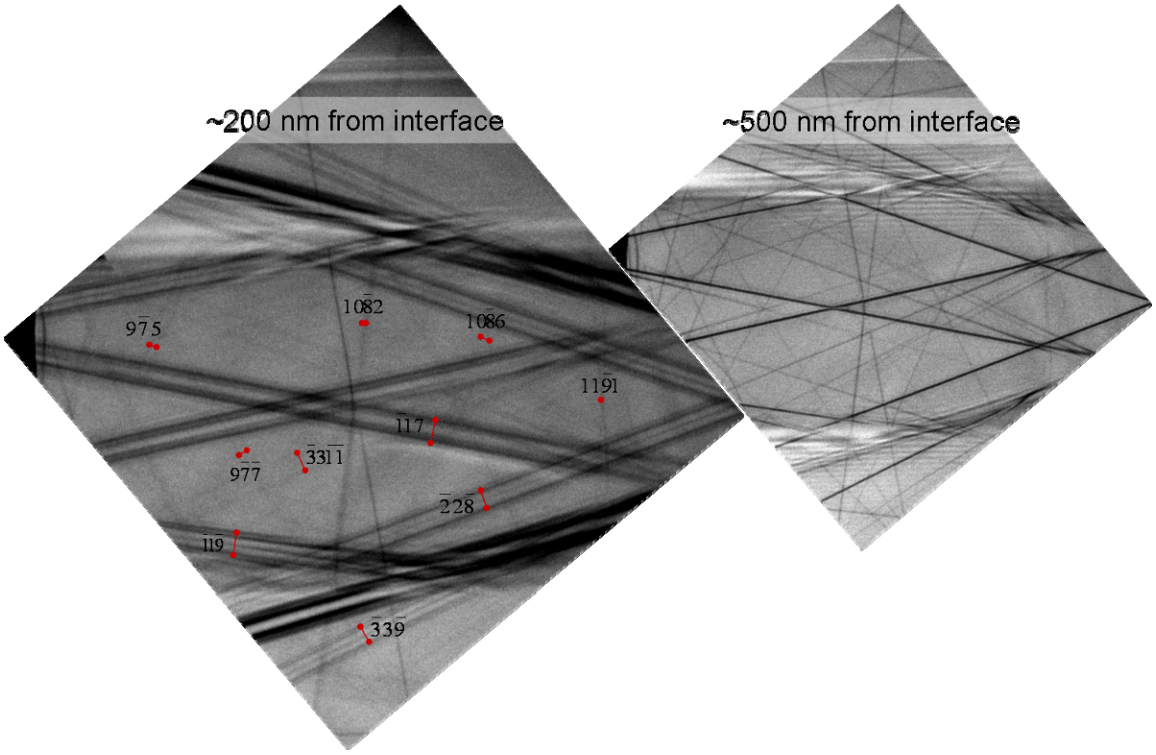

Figure 4.28 – <560> CBED patterns at two different distances from the SiGe/silicon interface in a 330 nm thick specimen of the SiGe02 wafer. Table 4.4 shows the degree of line splitting for the labeled lines.

Table 4.4 – The degree of line splitting measured for the HOLZ lines labeled in Figure 4.28 and the calculated degree of HOLZ line splitting expected for a rotational relaxation of 0.08°.

	$\bar{1}\bar{1}\bar{9}$	$\bar{1}\bar{1}7$	$\bar{2}\bar{2}\bar{8}$	$\bar{3}\bar{3}\bar{1}\bar{1}$	$\bar{3}\bar{3}\bar{9}$	$\bar{9}\bar{7}\bar{7}$	$10\bar{8}\bar{6}$	$\bar{9}\bar{7}5$	$10\bar{8}\bar{2}$	$11\bar{9}\bar{1}$
Measured (±.003)	.081	.078	.074	.078	.071	.043	.037	.031	.013	.009
Calculated	.079	.078	.075	.075	.072	.043	.035	.033	.015	.010

4.1.2.6 Numerical Values of Relaxation

While there is no known physical reason why a second order polynomial should describe the splitting width vs. distance from the interface curves for this geometry, it provides a reasonable fit to the curves and is useful for extrapolating an approximate degree of rotation for regions close to the interface where clear CBED patterns cannot be obtained. A quadratic equation also appears to provide a good fit for the relaxation data of Clement et al. for NiSi films on Si [49].

Using this method, the y-intercept values from the curves numerically approximate the total rotation angle in the thinned direction at the SiGe/silicon interface. Also, since the curves represent the angular rotational values as a function of distance from the interface, integration of these curves can lead to an approximate value for the change in length in the thinned direction between the unstrained region far from the interface and the stress relaxed region at the interface. The methodology of these calculations is shown in more detail in Appendix A.

Based on these results, schematic cross-sections are shown in Figure 4.29 for two different specimen thicknesses of the SiGe01 specimen and the additional length of the silicon at the interface (strain in the [110] direction) normalized by the specimen thicknesses is shown in Figure 4.30.

It is seen from the curves in Figure 4.21 and these schematic cross-sections that the angle of rotation of silicon at the interface appears to be nearly independent of specimen thickness. This is apparent in Figure 4.21 from the convergence of the curves as the distance from the interface approaches zero. This value appears to be around 0.4°. Since the relaxation is occurring on both sides of the specimen, this

means a rotation angle of ~0.2°on each side. It appears that the additional stress of thicker specimens is accommodated by the persistence of the rotational relaxation to greater distances from the interface.

Wilkinson found using electron backscatter diffraction (EBSD) that for epitaxial $Si_{.85}Ge_{.15}$ layers on high aspect-ratio silicon mesas there was significant rotational relaxation in the SiGe in the more narrow direction [53]. For mesas greater than 1 μm wide, this relaxation occurred on the outer 500 nm of the mesa. For those mesas less than 1 μm wide, the angular change in orientation persisted across the entire mesa width in a linear manner. In all cases, this relaxation led to a decrease in the SiGe strain in the [001] and [110] axial directions relative to SiGe on bulk silicon; the rotation about the $[1\bar{1}0]$ axis was the only significant shear strain. The strain in the $[1\bar{1}0]$ direction was only slightly decreased (less than a 5% change). The angles of rotation for the SiGe on the narrowest mesas, which are slightly larger than the thickest TEM specimens in this research, were 0.23°on each side. This is within 15% of the value calculated here. Khan et al. found similar relaxation behavior in 200 nm high, chemical vapor deposited $Si_{.8}Ge_{.2}$ lines on silicon using x-ray diffraction [54]. While they did not measure rotational values, they found that for lines less than 3 μm wide, the relaxation of the SiGe along the length ($[1\bar{1}0]$ axis) was less than 5%, while that in the narrow direction ([110] axis) was around 50%.

Finite element stress calculations have been performed for a range of specimen thicknesses with a 100nm film of $Si_{.83}Ge_{.17}$ on Si [55]. The film and substrate were assumed to be defect-free and only plane-strain was considered, i.e. no relaxation in the $[1\bar{1}0]$ direction as it is depicted in Figure 4.25. In these simulations the boundary

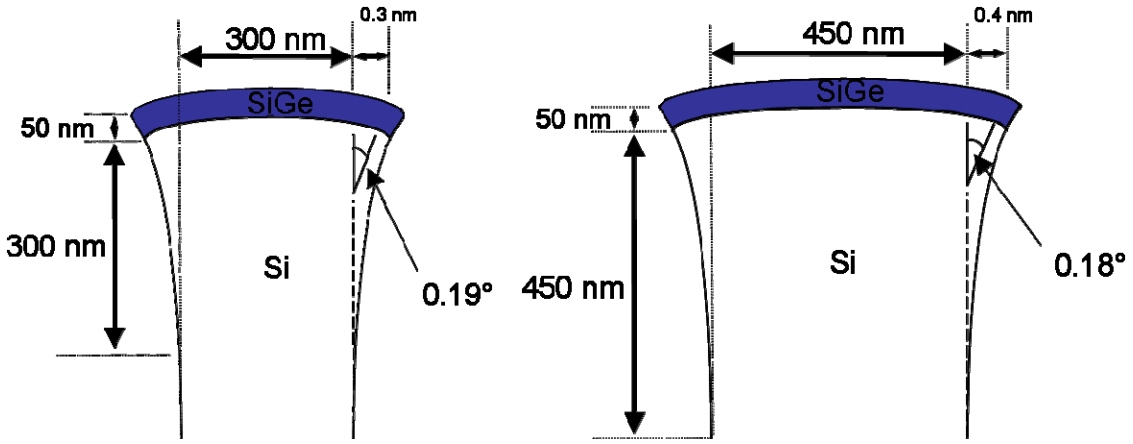

Figure 4.29 – Schematic illustrations of cross-sections of the SiGe01 wafer for two different specimen thicknesses.

conditions were that the bulk material (>5μm thick) had the full stress of -1860 MPa on the film at the interface and very thin specimens (<100nm thick) were completely relaxed (no stress).

For comparison between the stress values of the simulation and the strain values calculated from the experimental curves, it was assumed that the stress-free condition in the simulation was accommodated by the lattice parameter at the interface being the average of the unstrained Si and $Si_{.83}Ge_{.17}$ lattice parameters (0.32% strain on the Si). For the bulk condition, it was assumed that the $Si_{.83}Ge_{.17}$ lattice parameters were forced to match the Si (0% strain on the Si). For specimen thicknesses between the two boundary conditions, an inverse linear relationship between the compressive stress on the $Si_{.83}Ge_{.17}$ film and the strain on the Si substrate was assumed. The comparison between the simulation and experimental results are shown in Figure 4.30.

The experimental results of the SiGe01 blanket wafer specimen match quite well what is predicted by the simulation both for the strain values and the trend in strain as a function of thickness. The simulated conditions, while close to the experimental blanket

wafer, are not the exact same germanium concentration or film thickness. If the relaxation in the simulation is purely a function of the germanium concentration, then the simulated curve in Figure 4.30 would be shifted down about 0.02% for a $Si_{.85}Ge_{.15}$ composition. It is not clear how much of an effect the film thickness plays in this relaxation, but given these SiGe thicknesses relative to the substrate, not much difference in strain energies is expected between 50 and 100 nm thick films [56]. Additionally, a few assumptions of how to convert the simulated stress values to strain values were necessary as stated above. In general however, what is experimentally observed is consistent with behavior predicted by the model over the range of thicknesses examined. A comparison of the values calculated from HOLZ line splitting to the full range of the finite element calculated values (i.e. from fully relaxed to fully strained) is not possible due to the limited range of specimen thicknesses that can be examined in the TEM, i.e. thinner specimens do not have sufficient material to produce the number of diffraction events necessary for sharp HOLZ lines whereas in thicker specimens the transmitted electron intensity is insufficient for clear images.

For the SiGe02 specimens, the quantitative strain behavior was somewhat different as shown in Figure 4.31. The normalized [110] strain values are about 0.10 – 0.15% higher than for the SiGe01 specimens, which is expected due to the greater germanium content. However, the strain behavior doesn't show the same slight downward trend that the SiGe01 values do. This may be related to differences in the relaxation behavior or, more likely, is the result of an incomplete data set. For the specimen thicknesses analyzed, the line splitting versus distance curves (Figure 4.23) don't appear to converge to a common rotational value at the interface as the for the

SiGe01 wafer. This is perhaps due to a lack of data for distances closer to the interface than 100nm. The HOLZ line splitting at these distances was so great that the width of the splitting was unclear and not able to be measured. The polynomial fits without these data may not result in a good assumption of the strain behavior at the interface. This is supported by the fact that the data for specimens less than 500 nm thick do show the same slight downward trend as the SiGe01 wafer. The thickest SiGe02 specimens did not allow for HOLZ line splitting measurements closer to the interface than ~150 nm, increasing the uncertainty of a polynomial fit over those regions. Additionally, there may be better equations to match the rotation relaxation behavior than the simple polynomial method used here.

As shown in Figure 4.30, the relaxation of the SiGe01 specimens result in an additional length of Si at the interface of ~0.16 to 0.20% as compared to far away from

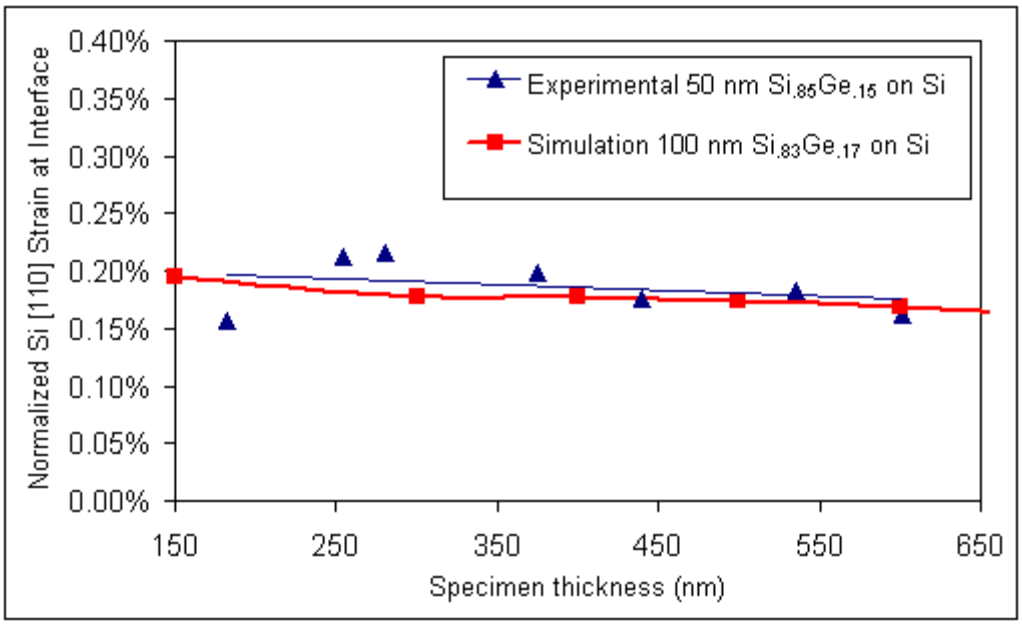

Figure 4.30 – Finite element calculated (Ref [55]) and experimentally determined [110] strain values for silicon at the SiGe/silicon interface in similar blanket wafer specimens.

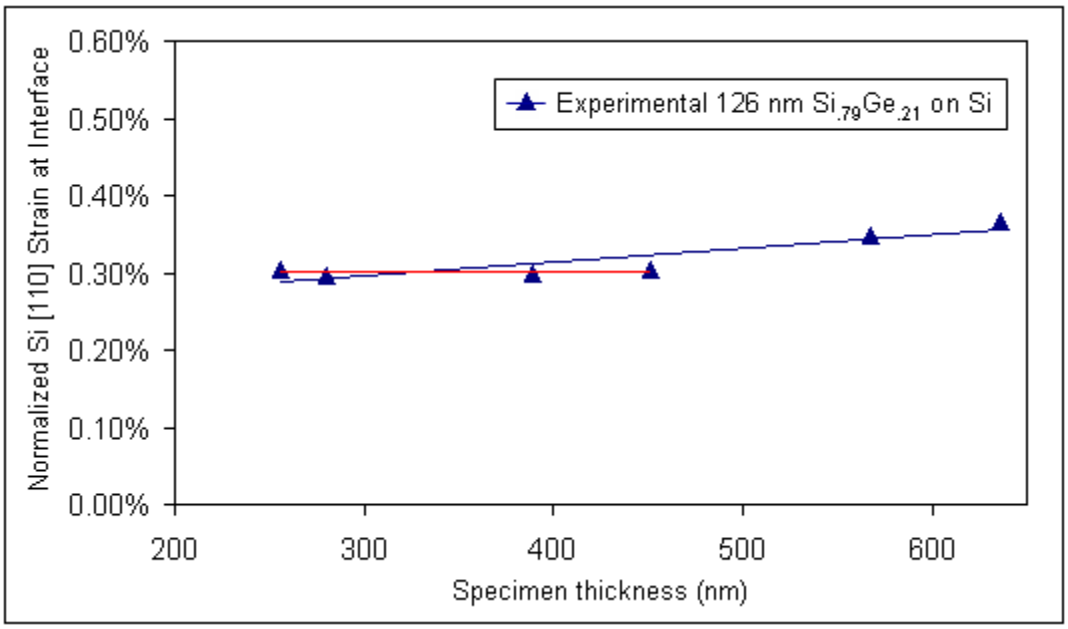

Figure 4.31 – Experimentally determined [110] strain values for silicon at the SiGe/silicon interface in the SiGe02 specimen. Trend lines are shown for the whole data set and for just the thinner specimens where the data are more certain.

the interface for the range of specimen thicknesses examined. The difference in the lattice parameters between unstrained $Si_{.85}Ge_{.15}$ and Si is 0.56%. The stress is accommodated more by the compression of the SiGe film in the [110] direction than the extension of the silicon substrate in that direction. This is not surprising given the larger amount of silicon and that the SiGe film is free to extend in the [001] direction to relieve some of the mismatch. This behavior also appears to be confirmed by the simulation data. Between unstrained $Si_{.78}Ge_{.22}$ and Si the difference in lattice parameters is 0.83%. The additional length at the interface experimentally measured for this sample ranged from 0.30 to 0.37%. Similar to the lower germanium content blanket wafer, the stress is accommodated more by the compression of the SiGe film in the [110] direction than the extension of the silicon substrate in that direction.

These values indicate that the observed relaxation results in a lattice parameter in the [110] direction at the interface that is intermediate to that of Si and $Si_{1-x}Ge_x$ in their unstrained states with a value slightly closer to that of the unstrained silicon. The SiGe film maintains 55 to 71% of its bulk [110] strain compared to the unstrained value. Stated differently, the silicon is extended 29-45% of the way from its unstrained state to the value of the unstrained SiGe.

4.1.2.7 Higher Order Laue Zone Line Profiles

While the width of the split HOLZ lines approximates the angular range of rotation of the relaxed specimen, there are also alternating light and dark fringes between the outermost split lines (see Figure 4.19). Other researchers have performed sophisticated finite element modeling [57], dynamical diffraction simulations [58], and multislice simulations [59] and shown that these can be attributed to the electron beam passing through different rotational and elastic strain states. Because these lines result from diffraction events through the thickness of the specimen, these analyses shed additional light on not only the additional length in the thinned direction due to relaxation but also on the relaxation behavior through the thickness of the material.

While that analysis has not been undertaken in this research, the results from the above cited research appear to be qualitatively consistent with what is observed here. None of those studies has explicitly stated the angles of rotation or overall [110] strain of the silicon due to relaxation, which could provide quantitative comparisons with the results here. This area merits further investigation.

4.1.3 Blanket Wafer Summary

For the SiGe blanket wafer systems, XRD showed that the SiGe01 sample has a 50 nm thick $Si_{.149}Ge_{.851}$ film lattice-matched to the silicon substrate. The SiGe02 sample has a 126 nm thick $Si_{.212}Ge_{.788}$ film also lattice-matched to the silicon substrate. Both samples exhibit a sharp interface between the film and substrate.

In the TEM, splitting of the HOLZ lines as a function of specimen thickness and distance of the electron beam from the SiGe/silicon interface was observed. This behavior was shown to result from rotational displacement of the crystal lattice caused by stress relaxation in the thinned specimens. The HOLZ line splitting behavior as a function of specimen thickness appears to provide a reasonable quantitative estimate of angular displacement and strain in the thinned direction resulting from stress relaxation effects. However, the variation in relaxation through the specimen thickness and the complete role of film thickness and germanium concentrations on these relaxation values is not clear and demands further investigation.

4.2 MOSFET Samples

The MOSFET samples analyzed consist of seven poly-silicon gates with 40 nm gate lengths bounded by rounded recessed regions of $Si_{.85}Ge_{.15}$ approximately 80 nm deep, 100 nm wide, and 950 nm long. SEM and TEM images of the structure are shown in Figures 3.8 and 3.9.

Two different samples of this structure were analyzed. In one sample, the wafer was removed from production just after the formation of the gate structures, prior to metallization. The other sample is that of the fully-processed wafer containing the

MOSFET gate. These samples will subsequently be referred to as the partially-processed wafer and the fully-processed wafer, respectively.

4.2.1 Relaxation Measurements

4.2.1.1 HOLZ Line Measurements – Thickness and Distance Effects

Similar to what was done with the blanket wafer specimens, HOLZ line patterns were collected at several distances from the gate/silicon interface for different specimen thicknesses. Splitting of HOLZ lines was also observed for these specimens but there was a difference in the splitting behavior for patterns collected under the SiGe region versus those collected under the gate.

4.2.1.1.1 Partially-Processed Wafer

The HOLZ line splitting data for the regions under the SiGe and under the gate for the partially processed wafer are shown in Figures 4.32 - 4.33. The splitting behavior under the SiGe regions is qualitatively similar to that of the blanket wafer specimens. The splitting under the gate regions is identical to that under the SiGe regions for distances greater than 200 nm from the gate/silicon interface. At distances closer than 200 nm, the width of the HOLZ splitting continues to increase but not as greatly as that under the SiGe regions. At approximately 80 nm from the interface, the degree of HOLZ line splitting under the gates reaches a peak. Upon closer approach to the interface, the width of the splitting decreases. Figure 4.34 compares the distance versus HOLZ line splitting curves for regions under the gate and under the SiGe of about the same specimen thicknesses.

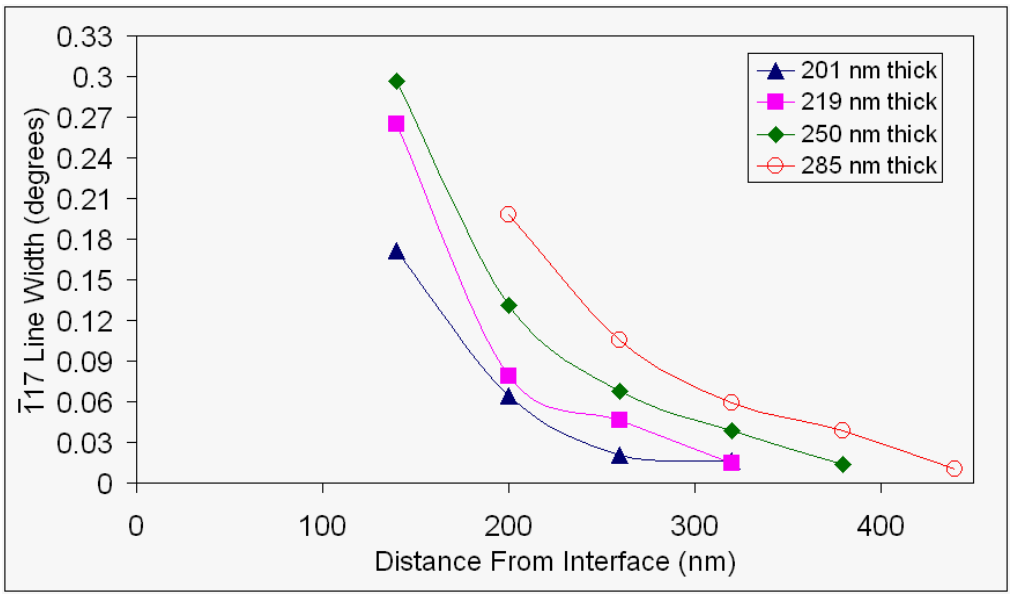

Figure 4.32 – Width of the split $\bar{1}17$ HOLZ line in <560> CBED patterns collected under the SiGe regions in the partially processed wafer as a function of distance from the gate/silicon interface for several specimen thicknesses.

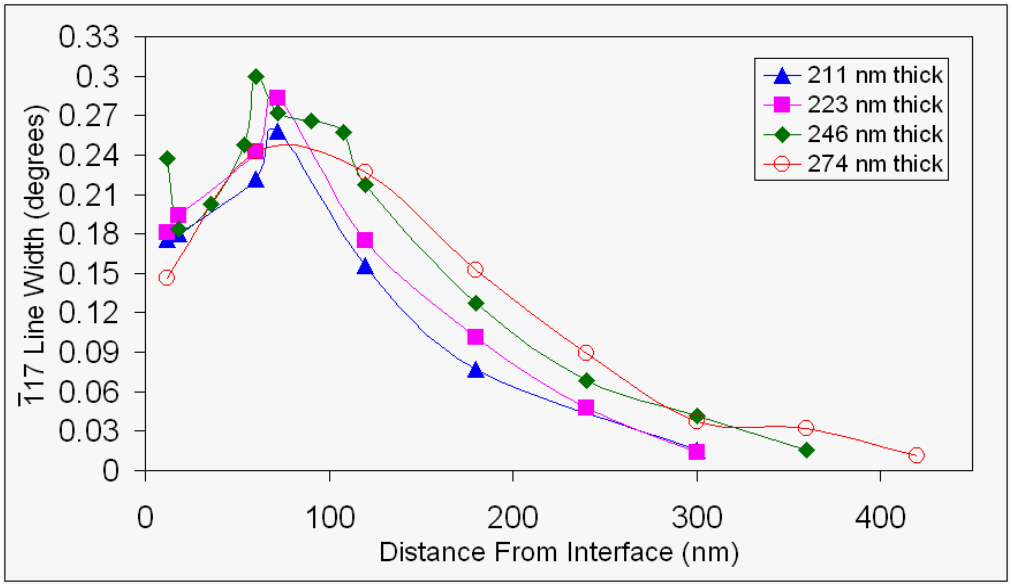

Figure 4.33 – Width of the split $\bar{1}17$ HOLZ line in <560> CBED patterns collected under the gates in the partially processed wafer as a function of distance from the gate/silicon interface for several specimen thicknesses.

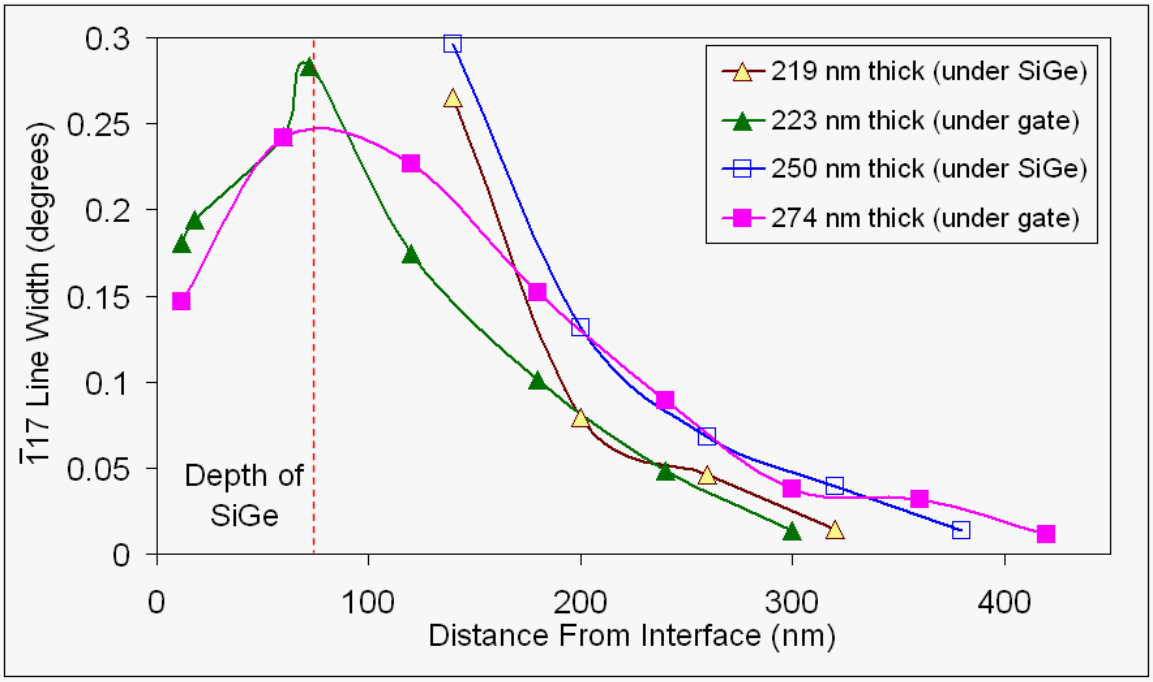

Figure 4.34 – Comparison of the HOLZ line splitting under the SiGe and under the gates as a function of distance from the gate/silicon interface in the partially processed wafer.

4.2.1.1.1.1 Comparison to Blanket Wafers

The HOLZ line splitting data suggest that this structure undergoes a more complex relaxation than the blanket wafers. However, it is useful to compare the two geometries. From the data in Figures 4.21 and 4.32, it can be seen that in the MOSFET specimens, a larger degree of HOLZ line splitting is observed for a given specimen thickness and distance from the interface. In order to explain this difference, it should be noted that, while the germanium concentration and SiGe thicknesses are similar for the specimens, the nature of the constraint of the SiGe regions is not. In the blanket wafers, the SiGe film is free to relax along the c-axis, as evidenced by the tetragonal distortion in the bulk blanket wafers. The thinning of these specimens allows another direction for the material to relax. In the MOSFET structures, since the SiGe regions

are recessed, they are considerably constrained by the silicon in all directions. Thus, the thinned direction for these specimens is the only direction for the significant relaxation of stress. This is illustrated in Figure 4.35.

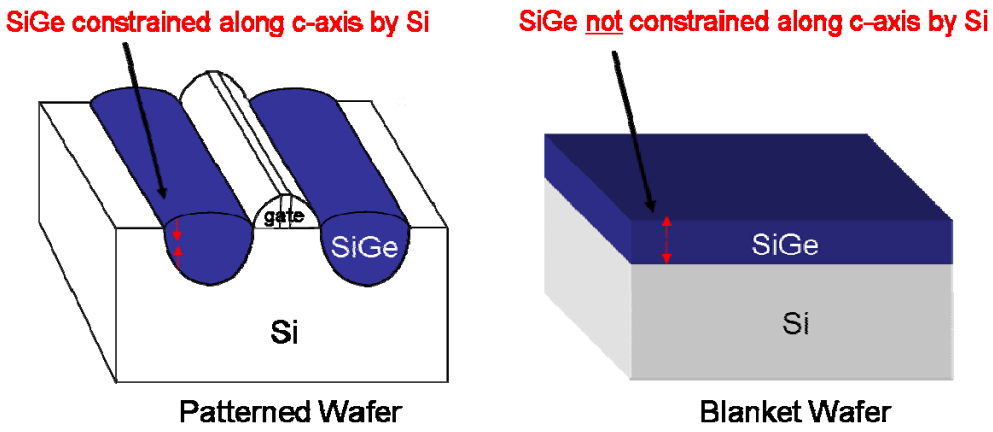

Figure 4.35 – Schematic showing the difference in the constraint of the SiGe between the patterned wafer and the blanket wafer.

The difference in the HOLZ line splitting curves between the regions under the SiGe and under the gate suggests that the stress relaxation, and therefore the stresses, in these two regions are different. This is further supported by the bright field and dark field TEM images (Figures 4.36 and 4.37) from these structures, which show strong bending contrast.

The peak in the degree of HOLZ line splitting at 80 nm from the interface corresponds with the depth of the SiGe regions. This is additional evidence that the distortion in the silicon caused by the relaxation of the SiGe regions is primarily responsible for the observed HOLZ line splitting in the silicon.

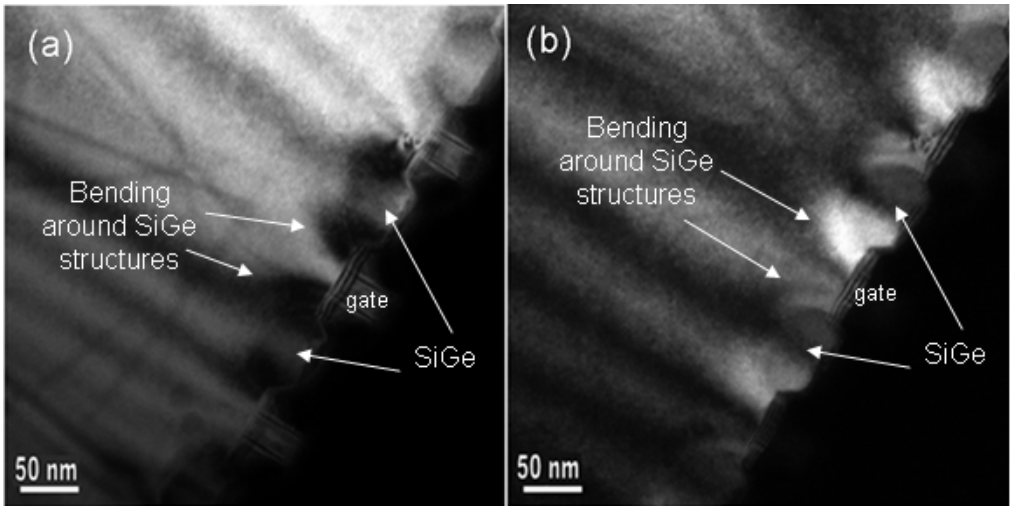

Figure 4.36 (a) bright field and (b) dark field images from a (220) two beam condition.

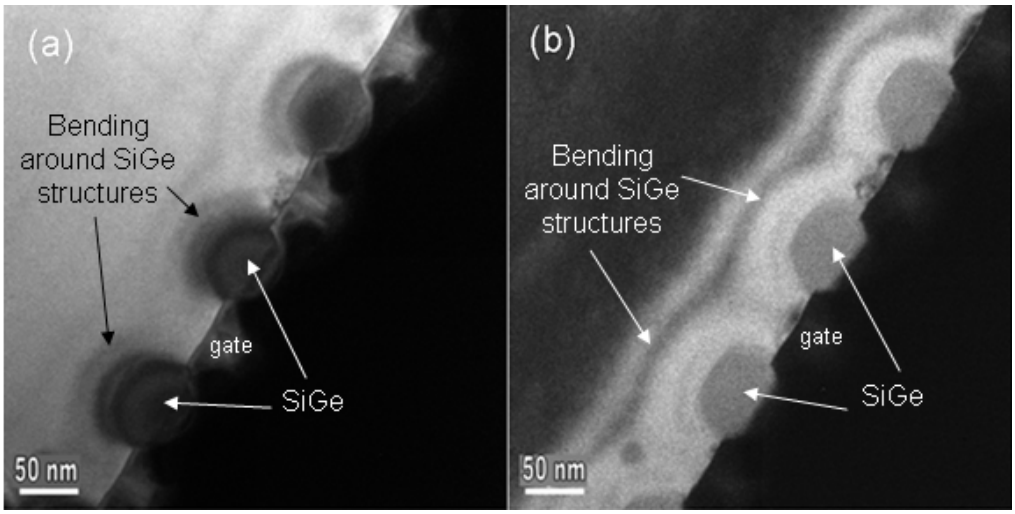

Figure 4.37 – (a) bright field and (b) dark field images from a (004) two beam condition.

4.2.1.1.2 Fully Processed Wafer

HOLZ line splitting data for the regions under the SiGe and under the gate for the fully processed wafer are shown in Figure 4.38. As compared to the partially processed wafer specimens, the difference in the line splitting behavior between the SiGe regions and gate regions is less pronounced. However, the regions under the SiGe still exhibited a somewhat greater degree of line splitting for regions less than 300 nm from

the interface. The most notable difference in the curves for the fully processed wafer specimens is that the splitting essentially disappears at a distance around 150 nm from the interface. This occurs both for the regions under the SiGe and the regions under the gate. This is shown in the CBED patterns in Figures 4.39 and 4.40.

From these data, it is obvious that the additional material above the MOSFET plays a significant role in the nature of the relaxation. The peak values of the widths of the split HOLZ lines are smaller in the fully processed wafer specimens than for the partially processed wafer specimens. Additionally, unsplit CBED patterns from the gate channel region can be obtained, allowing for strain measurements in this region as will be discussed in section 4.2.2. However, it is also apparent that having these layers does not eliminate the relaxation.

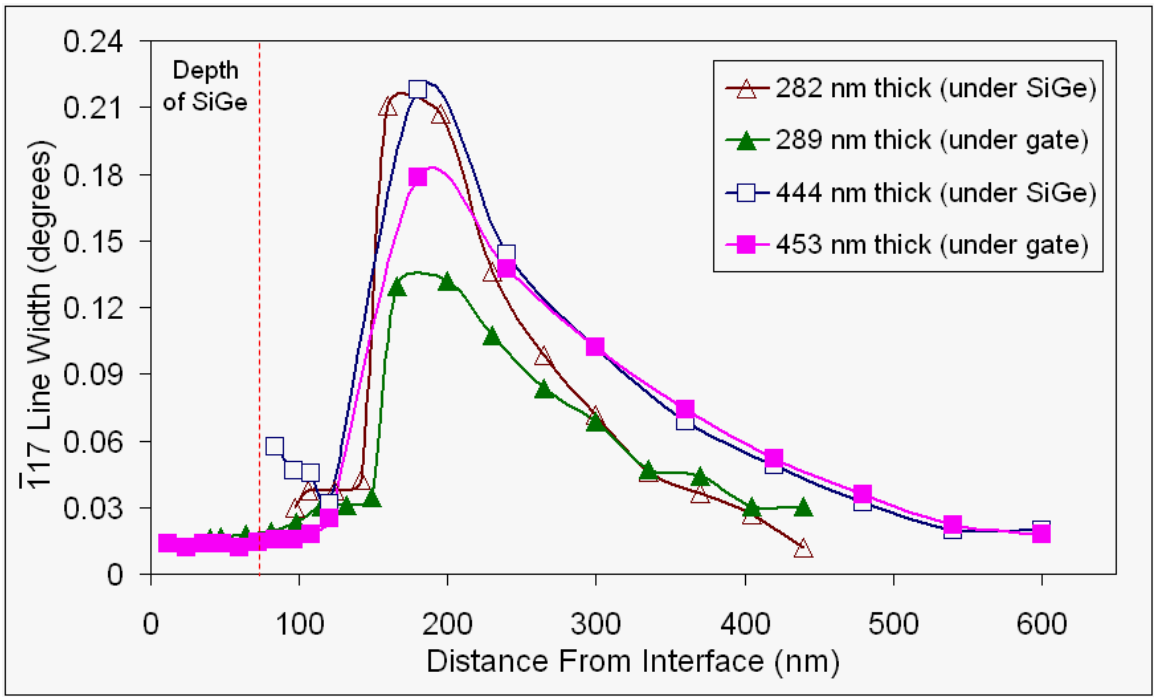

Figure 4.38 – Comparison of the HOLZ line splitting under the SiGe and under the gates as a function of distance from the gate/silicon interface in the fully processed wafer.

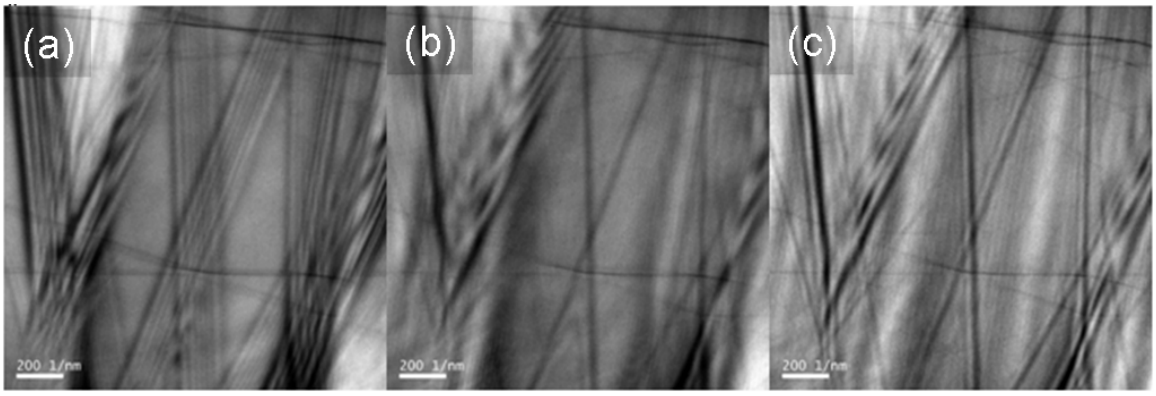

Figure 4.39 – <560> CBED images from the silicon under the SiGe regions at (a) 200 nm, (b) 150 nm, and (c) 100 nm from the silicon/gate interface.

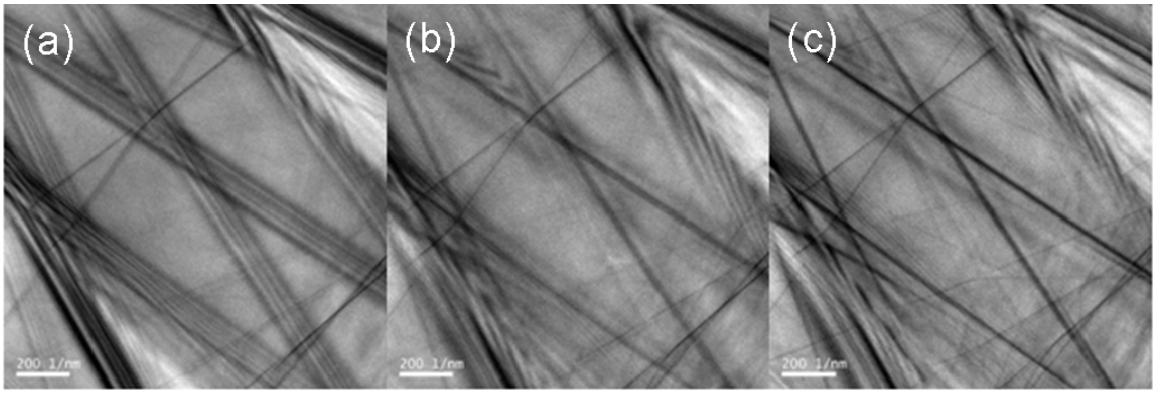

Figure 4.40 – <560> CBED images from the silicon under the gate regions at (a) 200 nm, (b) 150 nm, and (c) 100 nm from the silicon/gate interface.

4.2.1.1.2.1 The Nature of the Relaxation

Additionally, it was observed that CBED patterns collected not directly under the center of the SiGe region or the center of the gate exhibited HOLZ line splitting closer to the interface than 150 nm. For these patterns, a change in the nature of the HOLZ line splitting occurred around 150 nm from the interface. The HOLZ line patterns from distances greater than this were split symmetrically, that is, the pattern maintained its

mirror symmetry. However, around 150 nm from the interface, these patterns developed an asymmetry. This is shown in the images in Figure 4.41.

The reason for this behavior has been suggested already in the blanket wafer splitting analysis. The symmetry of the split pattern in that case was ascribed to the symmetry of the relaxation on both sides of the specimen. So it also appears that in the MOSFET specimens for distances greater than about 150 nm from the interface that the relaxation is symmetric, independent of location. But closer to the interface, the observed asymmetry means that for TEM beam locations not positioned symmetrically with regard to the SiGe structures, the beam samples regions whose relaxation behavior is different on the two sides of the specimen. This is shown schematically in Figure 4.42.

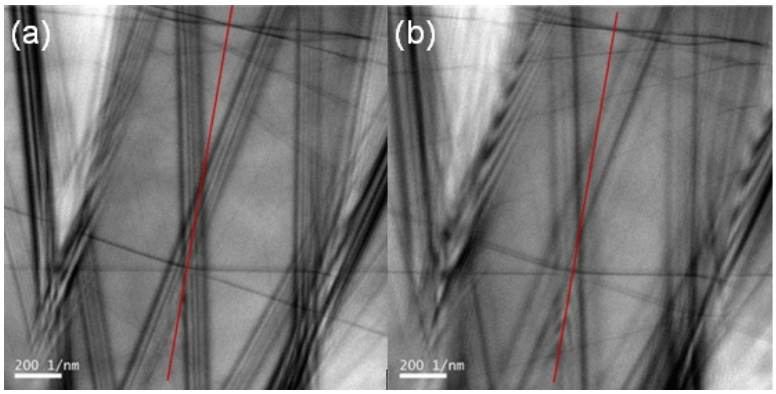

Figure 4.41 – <560> CBED patterns taken from a position not directly under the center of the gate at (a) 230 nm and (b) 140 nm from the silicon/gate interface. The red line in each picture indicates the mirror symmetry of the unsplit CBED pattern. The HOLZ line splitting in (a) maintains that mirror symmetry, whereas it does not in (b).

In the situation depicted in Figure 4.42, the relaxation of the SiGe is causing the silicon to rotate not only around the $[1\bar{1}0]$ axis below the SiGe, but also around the [001] axis to the side of the SiGe. If this is the case, it would be expected that the HOLZ

lines that exhibit splitting would change. Below the SiGe regions, the HOLZ lines corresponding to planes parallel to the (001) interface exhibited splitting as seen in Figure 4.41(a). Therefore, to the side of the SiGe regions in the gate channel, it should be expected that the HOLZ lines for the planes parallel to the $(1\bar{1}0)$ planes would exhibit splitting. Figure 4.44 shows that this is indeed observed in these regions. CBED patterns, such as Figure 4.41(b), captured from a location that is both below and to the side of the SiGe channels exhibit a combination of these effects.

Based on the above observations, a complete schematic model of the relaxation can be constructed. Figure 4.44 shows a three-dimensional representation and a cross-sectional slice through the center of the gate channel. A cross-sectional slice through the SiGe region looks similar, but exhibits a greater overall change in length in

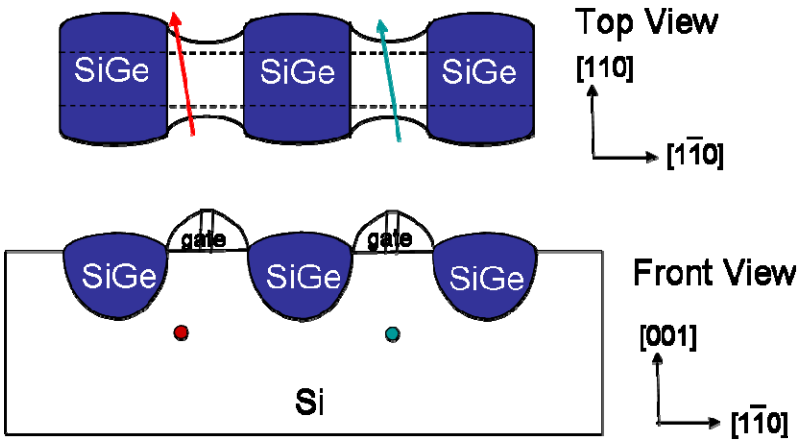

Figure 4.42 – In the top view image, the TEM beam, represented by the left arrow, passes through regions on the two sides of the specimen that do not have identical relaxation behavior, whereas the right arrow does. These arrows are represented in the front view image by dots. The dot on the left is asymmetric with respect to the gate and SiGe structures; the dot on the right is symmetric with respect to them.

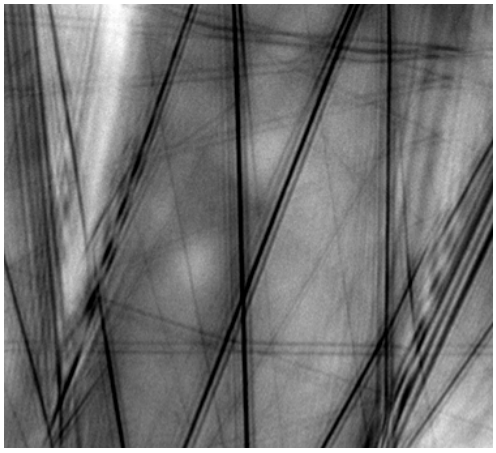

Figure 4.43 – <560> CBED pattern taken from beside the SiGe in the gate channel, 40 nm from the silicon/gate interface. The HOLZ lines for planes parallel to the (001) interface (nearly vertical in this image), do not exhibit splitting, while those orthogonal to this plane (nearly horizontal in this image) do.

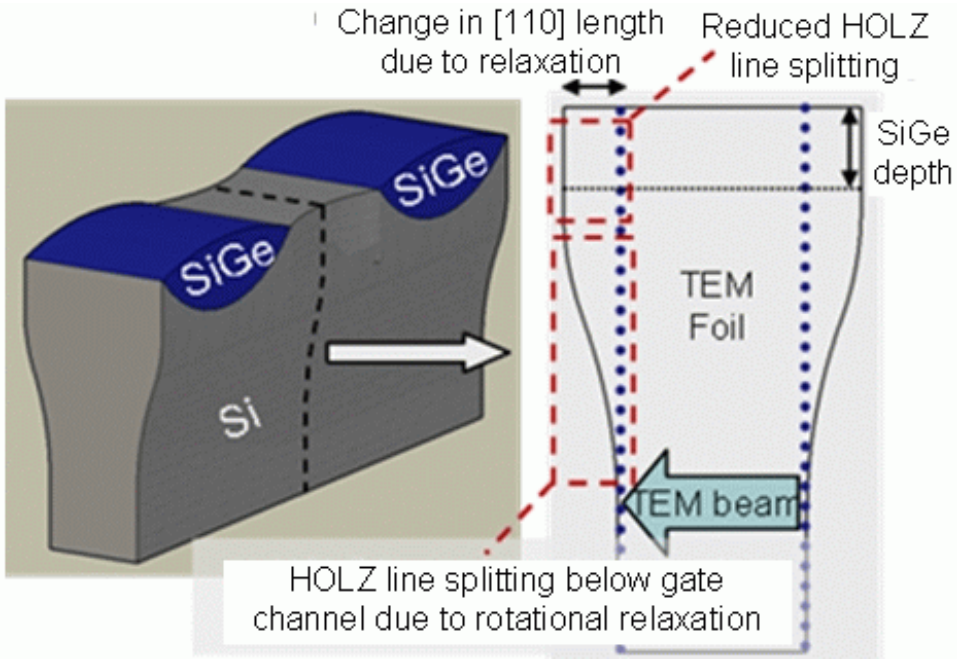

Figure 4.44 – Schematic image representing the MOSFET structure after relaxation due to thinning for TEM analysis. The figure on the right depicts a cross-section through the gate channel.

the [110] direction. The regions between the center of the gate channel and the center of the SiGe exhibit a gradual transition between those values as shown in the top view in Figure 4.42.

4.2.1.1.2.2 Methods Attempted to Avoid Relaxation

Since relaxation of the TEM specimen is undesirable for the quantitative analysis of strain, several alternative specimen preparation methods were tried in order to determine if this relaxation could be prevented.

One method was to mount the specimen such that the ion beam could be used to thin it from the side, thus leaving the bulk of the material above the gate channels. An SEM image of such a specimen is shown in Figure 4.45. While suitable TEM specimens were prepared in this manner, relaxation was not prevented (Figure 4.46).

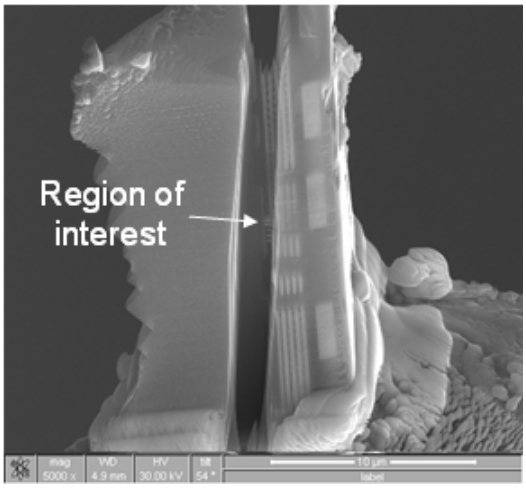

Figure 4.45 – SEM image of a TEM specimen prepared by FIB milling a channel parallel to the wafer surface, leaving intact the structure above and below the gate channel region.

Another method was attempted, namely, thinning only a very narrow region of the specimen to electron transparency. The thinnest such region that was successfully created had a width of approximately 110 nm. Due to the narrowness of the region, tilting in the TEM was extremely limited. Thus CBED analysis was confined to whatever direction allowed the beam to pass through the thin region. Even in this case, split HOLZ lines indicative of stress relaxation were still observed (Figure 4.47).

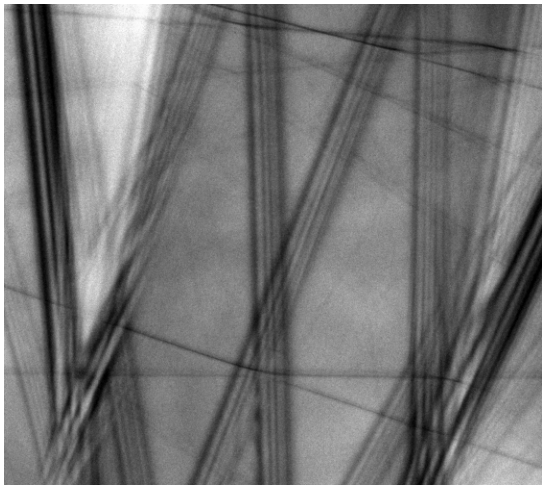

Figure 4.46 – HOLZ line image from the TEM specimen in Figure 4.45. This was taken using a <560> axis at a point 230 nm below the gate.

A third preparation was that of a plan view of the MOSFET structures. An image of this is shown in Figure 4.48(a). The CBED image from a SiGe region in Figure 4.48(b) shows splitting of the HOLZ lines. Similar to what was observed for the other specimen preparation methods, this is indicative of relaxation of the specimen in the thinned direction.

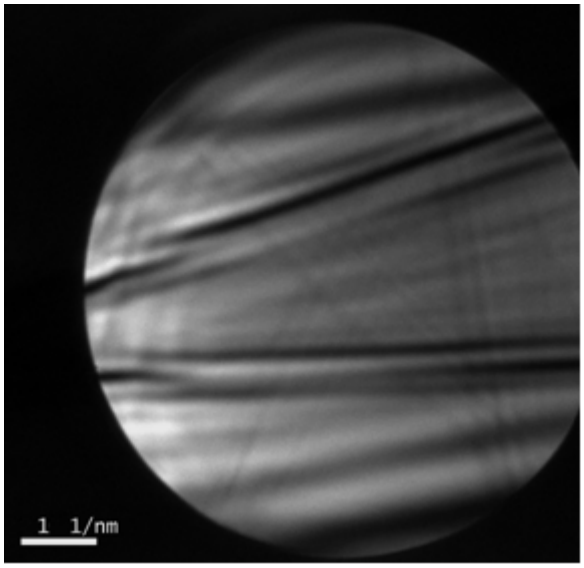

Figure 4.47 – HOLZ line image from an unknown incident beam direction in a specimen with a 110 nm wide thinned region.

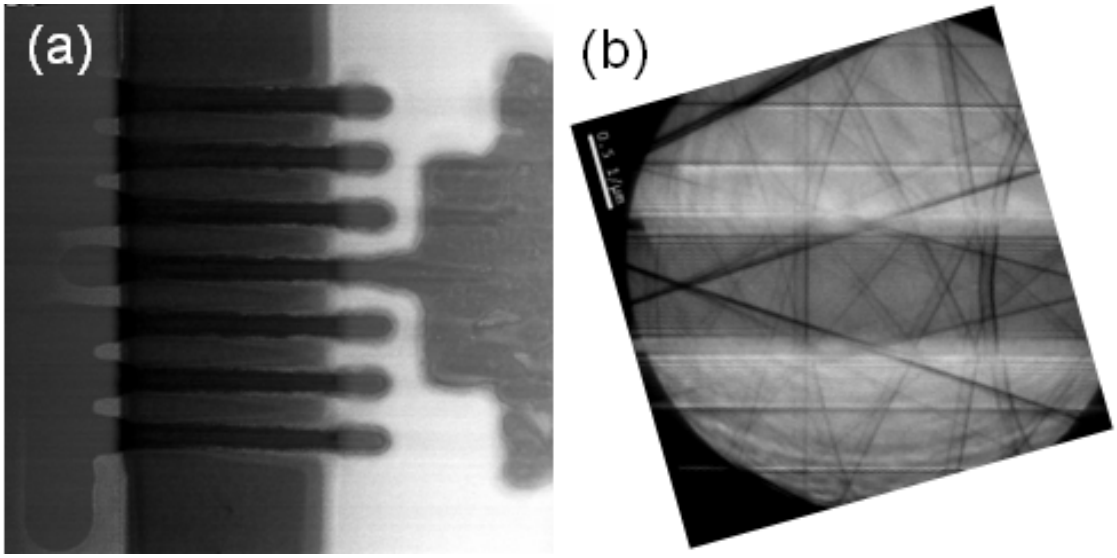

Figure 4.48 – (a) Bright field TEM image from a plan view MOSFET specimen. (b) CBED pattern from a SiGe area, showing HOLZ line splitting indicative of relaxation.

4.2.1.1.2.3 Numerical Values of Relaxation

Since relaxation of these specimens apparently cannot be avoided in the TEM specimen preparation process, it is important to quantify the relaxation.

As was done for the blanket wafer specimens, the amount of the relaxation can be calculated based on the curves of the HOLZ line splitting. This is described in Appendix A. However, as has been shown for these curves, the HOLZ line splitting disappears around 150 nm from the gate/silicon interface. Therefore, the relaxation calculations take into account only the values up to the disappearance of the HOLZ line splitting. It is assumed in that there is no further significant relaxation occurring in regions closer to the interface. These data for under the gate channel of the fully processed wafer specimens are shown in Figure 4.49. For several specimens analyzed with thicknesses between 225 and 475 nm, the values of the additional length due to relaxation were 0.09% $\pm$ 0.02% greater than the unstrained region far from the interface. These data do not indicate a clear trend, but this additional length in the [110] direction appears to be essentially independent of the specimen thickness with some sample to sample variability. The values of the additional length due to relaxation under the SiGe shown in Figure 4.50 are 0.11% $\pm$ 0.03% greater than the unstrained region far from the interface. In general the [110] strain under the SiGe due to relaxation appears to be 0.02 to 0.03% greater than that under the gate channel. It is expected that the values from both of these regions should trend toward zero as the structure thickness approaches the bulk structure. However, since only a relatively small range of specimen thicknesses can be sampled via this method, these trends are not clearly apparent.

4.2.2 Strain Measurements

The primary goal of performing CBED analysis on these transistors is to determine stress and strain. As mentioned in section 1, strain is being intentionally introduced into

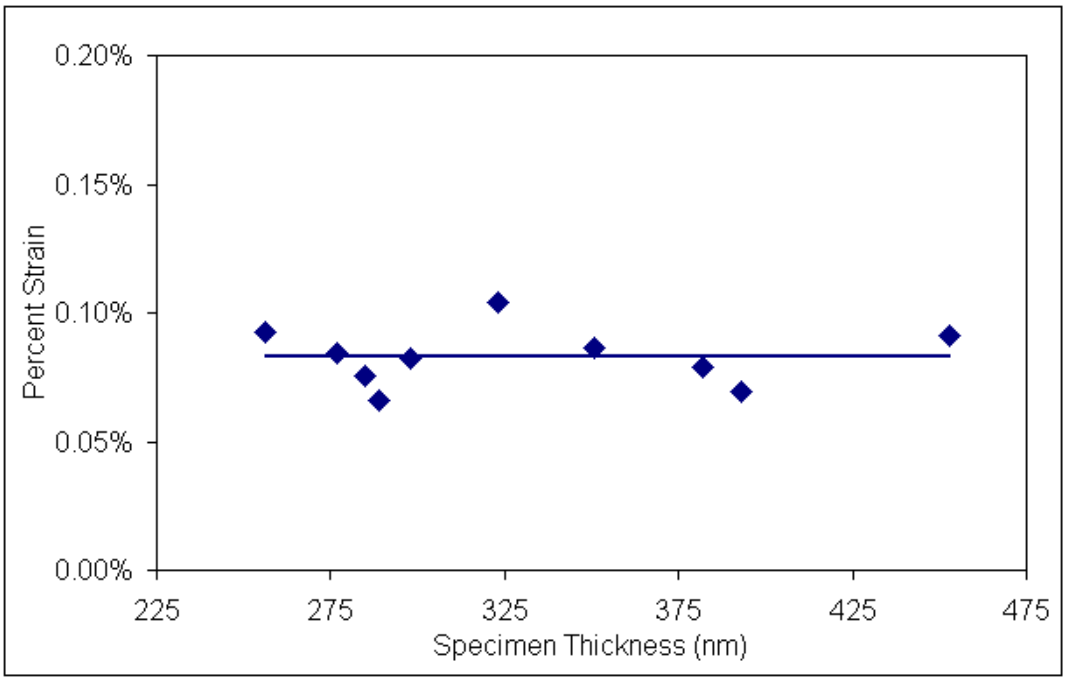

Figure 4.49 – Experimentally determined [110] strain values for silicon under the gate channel in the fully processed MOSFET structures.

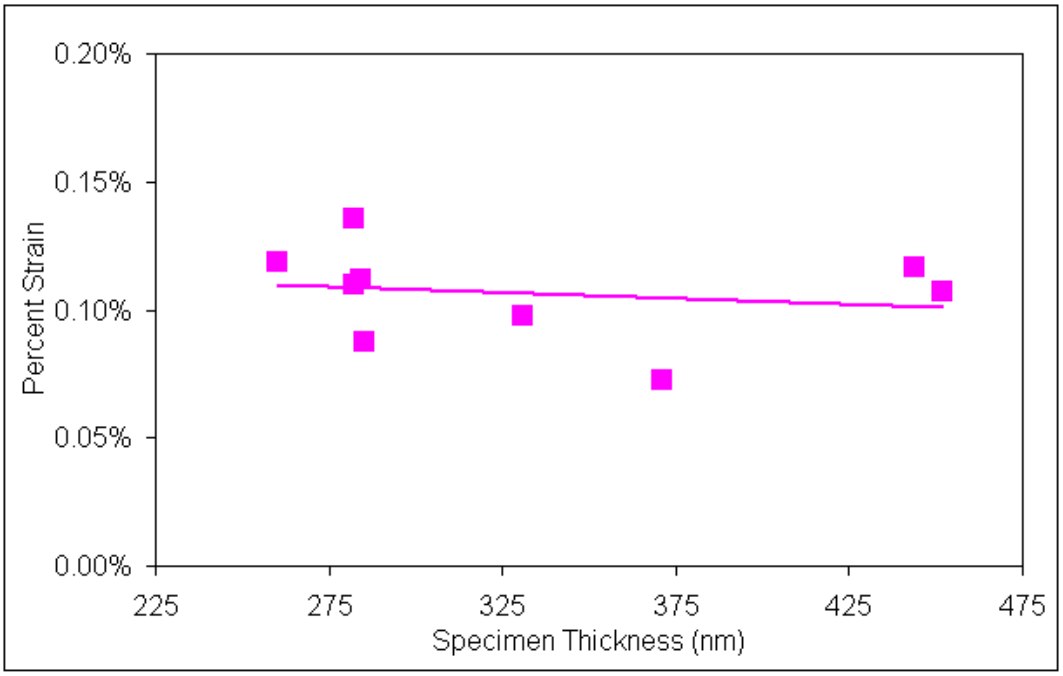

Figure 4.50 – Experimentally determined [110] strain values for silicon under the SiGe structures in the fully processed MOSFET structures.

the gate channels as a means of improving the mobility of the charge carrier. The ability to reliably measure the strain and correlate it with electrical measurements and processing conditions would prove highly valuable to the microelectronics industry.

4.2.2.1 Higher Order Laue Zone Line Pattern Simulations

HOLZ line patterns are considered a potentially effective way to measure strain in these devices because the electron beam can be focused locally to a spot size of approximately 1 nm and the shifts in HOLZ lines have been shown to have sensitivities to changes in strain down to around 10^{-4} [26-27]. These sensitivities are dependent on the HOLZ lines being used for the measurement because the strain determination in based on shifts relative to the unstrained pattern. As a result, some orientations are more sensitive to particular changes in a material's strain state and, therefore, more useful than others.

In order to assess the relative HOLZ line shifts due to strain in an effective manner, software programs that simulate the HOLZ line patterns from CBED have been developed [28-30]. These simulations can assume either kinematical or dynamical behavior of the electrons in the specimen.

A kinematical approach assumes that each electron undergoes only one diffraction event in the specimen. Which planes diffract is then determined entirely by the direction of incidence, beam convergence angle, and the deviation parameter. Due to the simplicity of this method, kinematical simulation programs can calculate shifts in HOLZ lines nearly instantaneously. This is advantageous when trying to fit an unknown pattern. The validity of the kinematical assumption varies for each reflection and is highly dependent on the zone axis.

Dynamical simulations better reflect the true behavior of the electron beam in the specimen. Most of these programs rely on the Bloch wave method of computing the resultant diffraction pattern. In this method, waves of periodic potential (Bloch waves), representative of the propagation of the electron through the periodic crystal lattice, are summed together as given by the equations:

$$b(\mathrm{r}) = \sum_{g} \mathrm{C_g} \exp(2\pi i(\mathrm{k} + g)\cdot r) \qquad (4.9)$$

$$\Psi^{total} = \sum_{1}^{n} A \cdot b(r) \qquad (4.10)$$

where b(r) is the Bloch wave function, C_g the plane wave amplitudes, k a reciprocal lattice vector, r a real space vector, ψ^{total} the Bloch wave function summation, and A the Bloch wave excitation coefficients. Applying the periodicity of the crystal potential to the Schrödinger equation is done through the following expression:

$$V(r) = \frac{h^2}{2me} \sum_{g} U_g \exp(2\pi i g \cdot r) \qquad (4.11)$$

where V(r) is the inner potential, h Planck's constant, m the electron mass, e the charge on the electron, and U_g the Fourier coefficients of the crystal potential. The Schrödinger equation becomes:

$$\nabla^2\Psi(r) + \frac{8\pi^2 me}{h^2}(E + \frac{h^2}{2me}\sum_{g} U_g \exp(2\pi i g \cdot r))\Psi(r) = 0 \qquad (4.12)$$

The solution of the Schrödinger equation in this form winds up being an eigenvalue equation:

$$M \cdot C_g = \gamma \cdot C_g \tag{4.13}$$

where M is an nxn matrix with n being the number of reflections, C_g is the eigenvector and γ are the eigenvalues. The matrix M is comprised of the following diagonal and off-diagonal components:

$$m_{gg} = 2Ks_g \tag{4.14}$$

$$m_{gh} = U_g \tag{4.15}$$

with

$$K^2 = \chi^2 + U_o \tag{4.16}$$

where s_g is the deviation parameter (see Figure 2.5), K the wave vector inside the crystal, χ the wave vector outside the crystal, and U_o the mean inner potential of the crystal.

The accuracy of the solution is increased as the number of reflections (Bloch waves) included in the total wave function is increased. However, including more waves in the calculations increases the calculation time. Therefore, the weaker waves are generally not included in the total Bloch wave function but instead are introduced into the crystal potential and deviation parameter using the Bethe potentials:

$$U_g^{eff} = U_g - \sum_h \frac{U_{g-h}U_h}{2Ks_h} \tag{4.17}$$

$$2Ks_g^{eff} = 2Ks_g - \sum_h \frac{U_{g-h}U_{h-g}}{2Ks_h} \tag{4.18}$$

for

$$\mathrm{K} \cdot \mathrm{s_h} >> \left|U_g\right|_{\max} \tag{4.19}$$

Equation 4.19 is the weak wave definition that is generally used [60].

This assumption treats the weak waves as having a perturbational effect on the strong waves. Even with the Bethe potential assumption, a typical dynamical simulation pattern takes several hours to complete.

Another dynamical simulation technique used to calculate HOLZ line patterns is the multislice method [29]. In this, the crystal is considered to be comprised of a series of thin slices separated by an infinitesimally small vacuum layer. Each slice contains a planar crystal potential that acts on the incident electron wave. The exit wave of each slice is then considered as the incident wave for the next slice.

4.2.2.1.1 Comparison of Kinematic, Dynamical, and Experimental Patterns

In this research the jems simulation program [28] was used to produce both kinematical and dynamical HOLZ line patterns. The dynamical patterns were created using the Bloch wave method and the Bethe potential assumption. Kinematical, dynamical, and experimental patterns from the <230>, <340>, and <670> axes are shown in Figures 4.51 through 4.53. From these it can be seen that the dynamical simulations accurately reproduce the positions and line intensities seen in the experimental patterns, whereas no variation in line intensity can be created by the kinematical simulations.

4.2.2.2 Calculating Strain Experimentally Using HOLZ Lines

Strain analyses in silicon CMOS devices using HOLZ lines in recent years have typically been performed using a <230> axis [32-35]. In addition to the strain sensitivity of the lines, one main reason cited for using that axis is the good match with kinematic

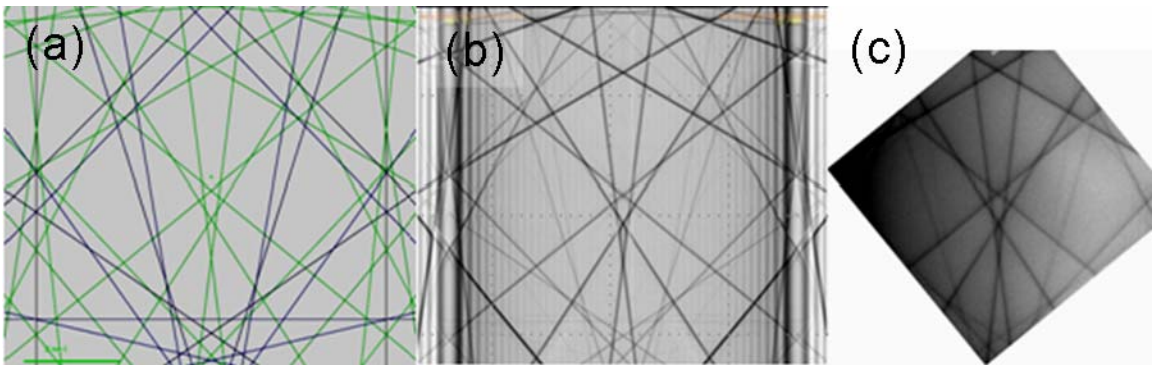

Figure 4.51 – (a) Kinematical, (b) dynamical, and (c) experimental <230> HOLZ line patterns for unstrained silicon.

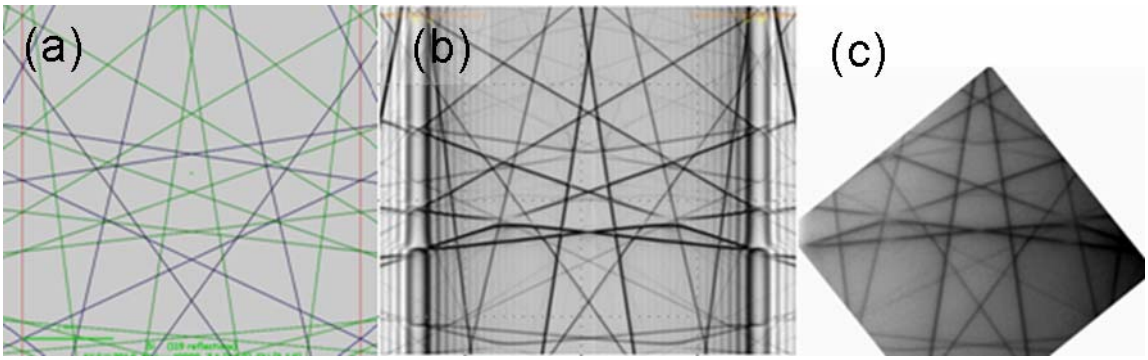

Figure 4.52 – (a) Kinematical, (b) dynamical, and (c) experimental <340> HOLZ line patterns for unstrained silicon.

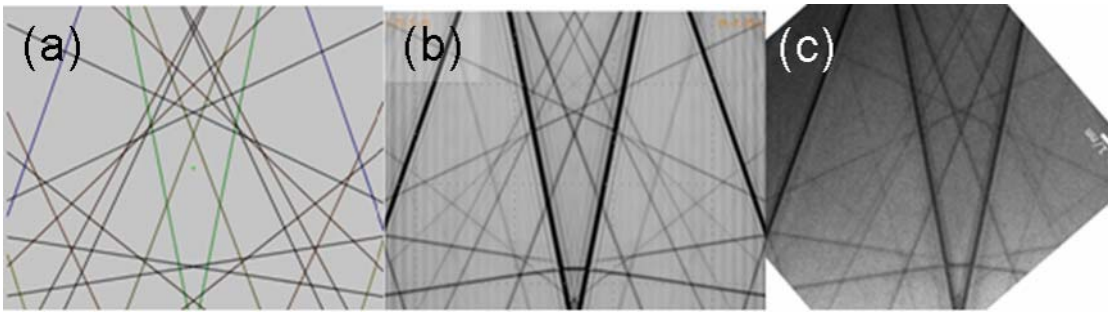

Figure 4.53 – (a) Kinematical, (b) dynamical, and (c) experimental <670> HOLZ line patterns for unstrained silicon.

simulations [32-33, 35]. Some research has also demonstrated the potential of using a <340> axis [61-62]. One goal of this research is to determine the effectiveness of a

<670> axis for strain determination in <110>-oriented silicon structures. The benefit of this is improved lateral resolution as has been previously discussed in section 4.1.2.2.

The <670> axis was decided upon after analysis of several zone axes along the (004) Kikuchi band. It was deemed important to stay along the (004) Kikuchi band for these analyses because for these orientations the electron beam maintains a constant distance from the gate through the specimen thickness. Simulations of several strain states were performed for these axes to ascertain the sensitivities of the HOLZ lines to the anticipated lattice distortions for the MOSFET structures. Comparisons between the kinematical, dynamical, and experimental patterns were also performed as seen in Figures 4.51 - 4.53.

4.2.2.2.1 Methods of Strain Determination

Strain state calculations from the HOLZ line patterns have been performed by several researchers using a variety of methods – distance between HOLZ line intersections [22, 63], normalized distance between HOLZ line intersections [64], normalized area bounded by HOLZ lines [65-66], and distances in Hough transform space [67-69]. The results from these measurements are typically compared to simulations. Normalization by using the ratios of feature sizes (distance or area) is used to adjust for differences in magnification between the experimental and simulated patterns. When comparing the distance method and the area method for measuring strain, it is possible to envision individual scenarios where either method will fail (Figures 4.54 and 4.55). This is overcome by making measurements which include several HOLZ lines and choosing HOLZ lines which have different sensitivities to the lattice variables of interest.

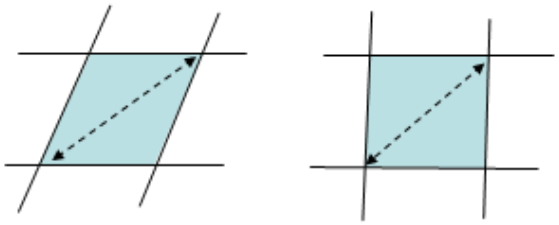

Figure 4.54 – Illustration of two regions having the same area but different distances between a pair of intersections.

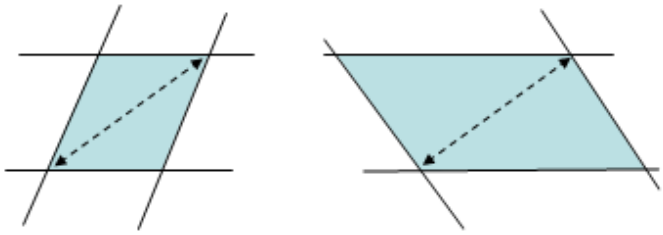

Figure 4.55 – Illustration of two regions having different areas but the same distances between a pair of intersections.

Regardless of the method used to evaluate the changes in the HOLZ line patterns, chi-squared minimization is the typical refinement method for producing the best match between the simulated and experimental patterns [22]. This equation is:

$$\chi^2 = \frac{1}{N-p}\sum_i \frac{1}{d_i^{simul}}(d_i^{simul} - d_i^{\exp})^2 \qquad (4.20)$$

where N is the number of data points, p the number of parameters, d^{simul} the simulated distance (area), and d^{exp} the experimental distance (area).

4.2.2.2.2 Defining the Variables of Interest

While, in principle, one HOLZ line pattern contains information about all six lattice parameters, it has been shown that it is generally not possible in practice to extract all of the lattice parameter values from a single pattern [65-66,70]. The area of reciprocal space from which the three-dimensional information is produced is confined to planes

within a very small range of angles from the incident beam direction (about 4.6° in this work, from section 4.1.2.1). Thus, some changes in strain state have been shown to be essentially indistinguishable for a given zone axis [70]. Additionally, algorithms that attempt to solve all six lattice parameters from a single pattern have been shown to be unable to produce a unique solution [65-66]. Only by reducing the number of unknown parameters to three was a unique solution produced. Instead, three or more different zone axis patterns from the same area can be required for simultaneous determination of all six lattice parameters [64]. In many cases of localized strain measurements, this is not possible or effective, as changing the incident direction changes the sampled volume of the material and, therefore, the patterns collected from the different orientations may not be sampling the same localized strain state. Therefore, assumptions about the strain state are typically made to reduce the number of variables so that a unique fit to the pattern can occur.

One assumption that has typically been made is that of plane strain [30, 71-72]. That is, the strain of the specimen is confined to occurring in one plane. This plane is usually assumed to be the plane orthogonal to the thinnest direction of the TEM specimen. In the case of <110> silicon-based devices, this is a {110} plane. By making this assumption, the number of lattice parameter variables can be reduced to three: a, c, and α. This is because $\Delta a/a = \Delta b/b = \Delta\gamma/2$ and $\alpha + \beta = 180°$ with this assumption. It has been shown that a unique fit to strained HOLZ line patterns from the <230> and <340> axes can be obtained with having only these three variables [61,72-73].

However, as has been shown in the present research, there is stress relaxation of the MOSFET device specimens orthogonal to the (110) plane. The assumption of the strain in the gate channel of the MOSFET devices being confined to just one plane appears invalid. Therefore, for strain measurement in this research, different assumptions about the strain state must be made.

Instead of plane strain, the strain was defined as occurring along three principal axes: the $[1\bar{1}0]$ (compression due to the SiGe structures), the [110] (relaxation normal to thinned specimen), and the [001] (relaxation in the plane of the thinned specimen). Translating these to the lattice parameters of the silicon crystal structure, it was assumed that α and β would remain 90° as the one-dimensional compressive force from each side would be equal in the center of the gate channel and the relaxation would be the same on both sides of the specimen. For the same reasons it was assumed that a equals b. These assumptions result in three independent variables: a, c, and γ. The result is the following strain tensor:

$$\begin{bmatrix} \varepsilon_{11} & \varepsilon_{12} & 0 \\ \varepsilon_{12} & \varepsilon_{22} & 0 \\ 0 & 0 & \varepsilon_{33} \end{bmatrix} \qquad (4.21)$$

Figure 4.56 shows the relationship of the device structure with the silicon lattice.

The shifting of HOLZ lines is sensitive not only to changes in the lattice parameters, but also to changes in the accelerating voltage of the electron microscope. Changes in voltage alter the wavelength of the incident electron beam. This makes it necessary to account for this variable as well. One method for doing this is to collect a HOLZ line pattern from an unstrained region of the material. All of the lattice parameter

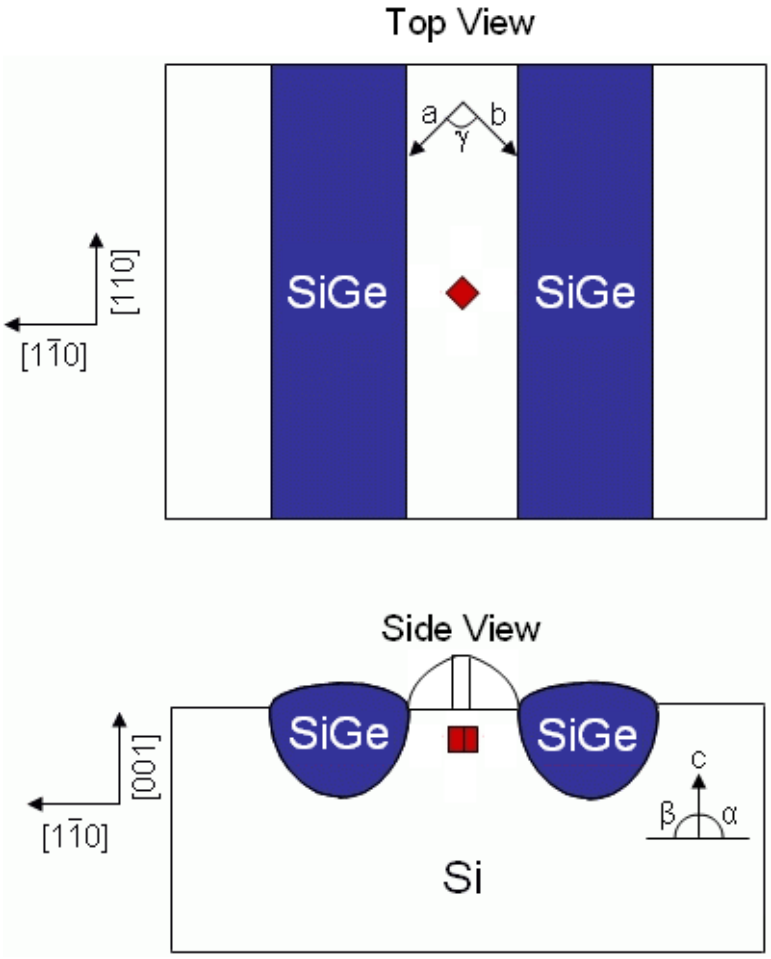

Figure 4.56 – The orientation of the silicon crystal lattice within the device structure.

values are known, therefore the fitting of the experimental HOLZ line pattern is performed simply by finding the accelerating voltage that provides the least deviation between the simulated and experimental patterns. Because electron microscopes may exhibit fluctuations in their accelerating voltages, this determination should be performed each time the microscope operating conditions have changed.

4.2.2.2.3 HOLZ Line Sensitivity to Strain

The sensitivities of HOLZ line shifts to strain in a particular material are dependent on the particular HOLZ lines examined and the incident zone axis. Therefore, the choice of both of these is crucial when determining whether the CBED method will provide the desired resolution for a given system. Studies on several systems using various zone axes indicate that through the judicious choice of these criteria, measurable HOLZ line shifts can correspond to changes in strain state as small as 1 - $2x10^{-4}$ [26-27,66,69].

The following is a description of the strain study of the <670> axis using dynamical simulations that preceded its use for strain measurement in the MOSFET devices. The changes in distance between several intersection points of HOLZ lines were measured as a function of different lattice parameters. The labeled HOLZ lines and the intersection points used for the strain analysis are shown in Figure 4.57.

Dynamical simulations were performed for a detailed analysis separating out the individual contributions of each of the four variables, voltage, the [110] axis, the $[1\bar{1}0]$ axis, and the [001] axis, to the change in distances between the HOLZ line intersection points. This was performed using a 4x2 design of experiments with a regression analysis used to separate out the individual variable contributions. No significant higher order variable interactions were found in the analysis. That is, each variable was found to have an independent, linear effect on the distance between intersection points. Assuming that changes equal to half of the HOLZ line width (approximately .042 nm^{-1} or 0.003 degrees) in the unstrained pattern are detectable, the corresponding sensitivities of each of the 16 distances used in the strain calculations were determined. They all

have strain sensitivities between $1x10^{-4}$ and $4x10^{-4}$ for each of the three principal strain axes. The sensitivities of each set of intersection points for each axis are shown in Appendix B. Similar analyses were done for the <230> and <340> axes and their results are also given in Appendix B.

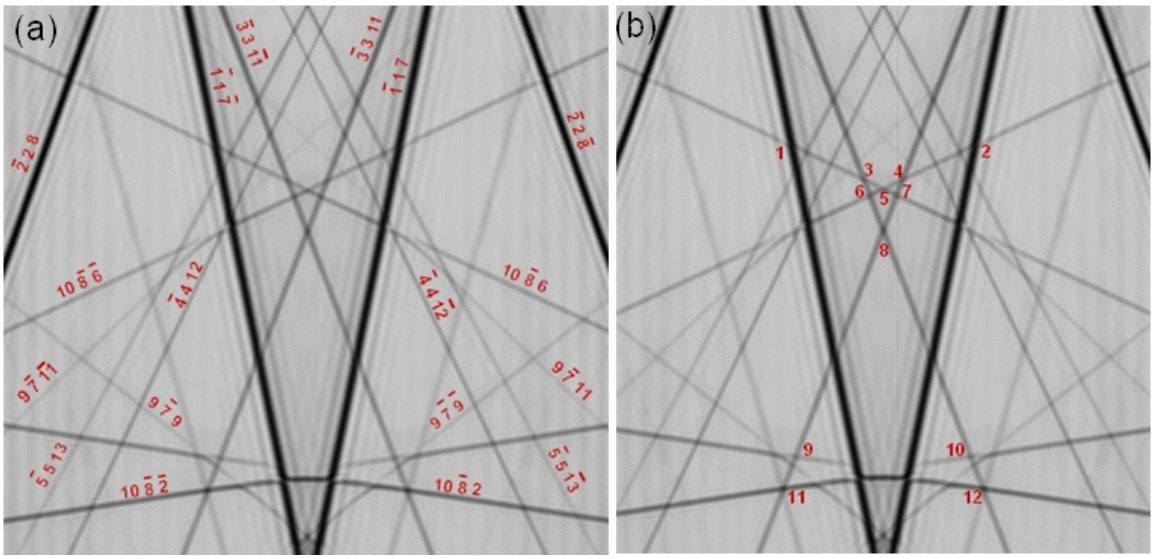

Figure 4.57 – Dynamically simulated <670> HOLZ line patterns showing (a) the labeled HOLZ lines and (b) the HOLZ line intersections used for strain analysis.

4.2.2.3 Fitting of Experimental Patterns

With the simulation results of the individual variable effects, the strains in the experimental patterns could be determined. An experimental pattern from an unstrained region of the specimen was used to find the correct accelerating voltage parameter as previously described. A scaling factor was also introduced due to magnification differences between the simulated and experimental patterns. The scaling factor was adjusted to produce the value that gave the smallest standard deviation in the accelerating voltage values determined from each of the individual

distances between HOLZ line intersections. This calculation also then output the accelerating voltage. This voltage value was then used in subsequent calculations from the strained regions. As mentioned previously, some researchers have used ratios of distances instead of scaling the images to account for magnification differences. However, a scaling factor should be less error prone since it uses all of the distances, not just one, to determine the ratio. The experimental accelerating voltages were all found to be between 201.10 and 201.20 keV with standard deviations around 0.06keV.

4.2.2.3.1 Non-Uniqueness of Patterns with Three Variables

The number of lattice variables that can be independently determined from a given HOLZ line pattern was previously mentioned in section 4.2.2.2.2. Previous research has shown that it is not possible with six variables, but is possible with three [65]. However, this is highly dependent on the crystal system, zone axis, and which variables are kept independent. Studies of a fitting algorithm have shown that even after a satisfactory solution has been attained, further iterations may produce different, equally good solutions, resulting in what the authors have described as “drifting” through parameter space [67]. They found that changes in two variables at a set ratio produced equivalent simulated HOLZ line patterns. In other words, there is not necessarily a unique set of variables which produces the HOLZ line pattern.

Similarly, in this research it has been found for all three zone axes of interest, that having a, c, and γ as the independent variables does not produce a unique solution. Instead a series of solutions occurs whereby changes having the ratio of the variables a : c : γ as 0.145 nm : 0.095 nm : 1° produce identical patterns. This is shown for all three

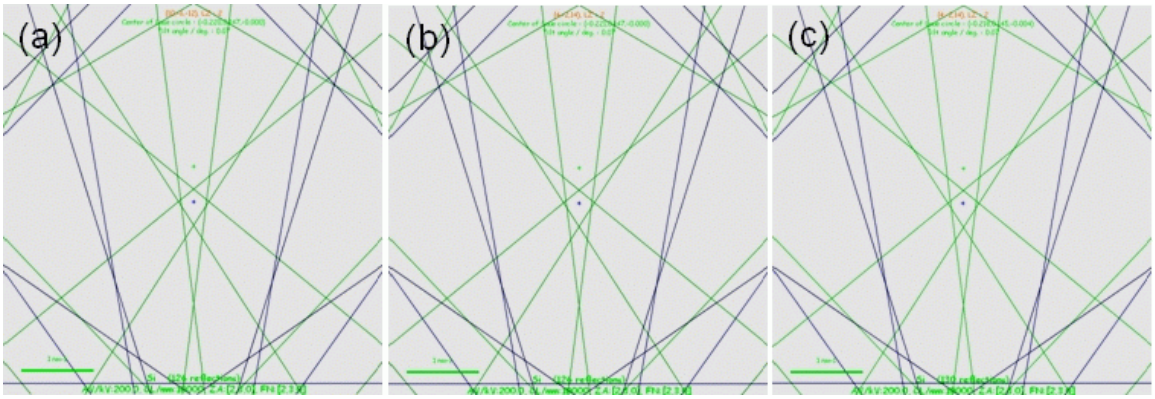

Figure 4.58 – Kinematical simulations of the <230> axis with (a) a=0.54019 nm, c=0.54119 nm, and γ=90.2°, (b) a=0.54309 nm, c=0.54309 nm, and γ=90.0°, and (c) a=0.54599 nm, c=0.54499 nm, and γ=89.8°.

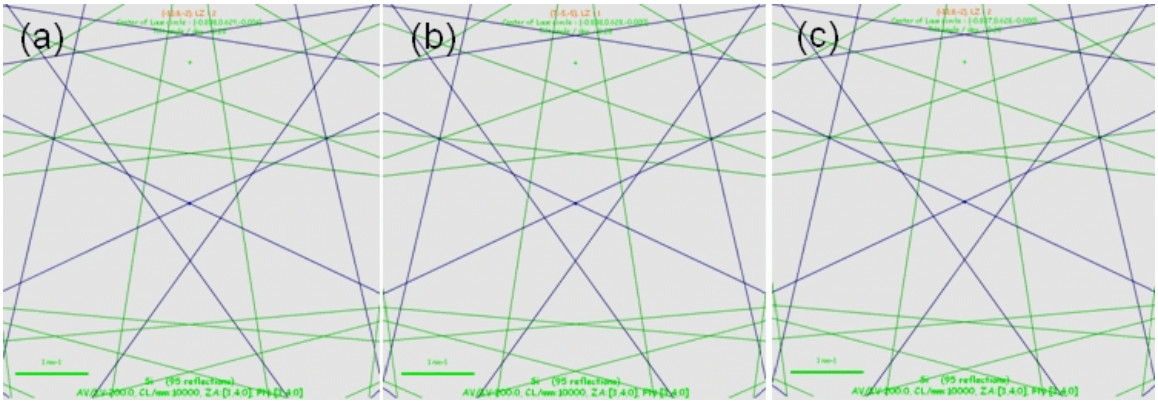

Figure 4.59 – Kinematical simulations of the <340> axis with (a) a=0.54019 nm, c=0.54119 nm, and γ=90.2°, (b) a=0.54309 nm, c=0.54309 nm, and γ=90.0°, and (c) a=0.54599 nm, c=0.54499 nm, and γ=89.8°.

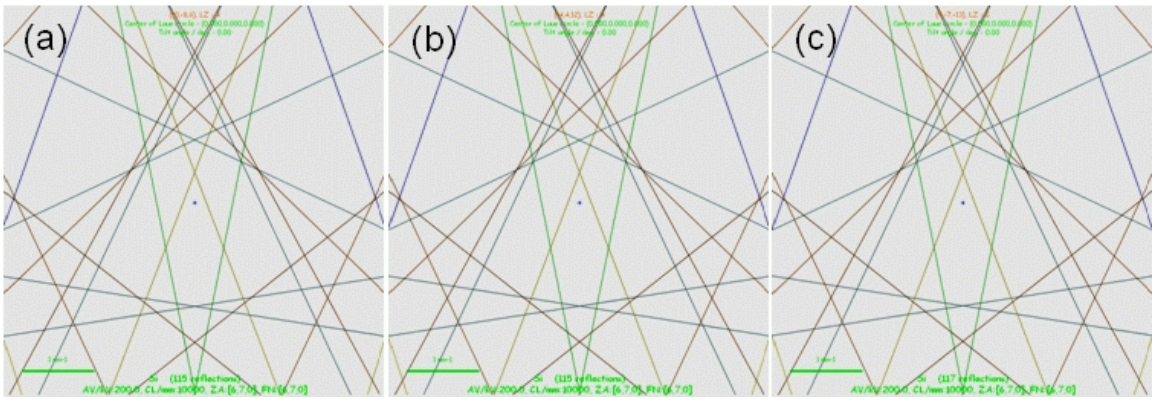

Figure 4.60 – Kinematical simulations of the <670> axis with (a) a=0.54019 nm, c=0.54119 nm, and γ=90.2°, (b) a=0.54309 nm, c=0.54309 nm, and γ=90.0°, and (c) a=0.54599 nm, c=0.54499 nm, and γ=89.8°.

zone axes in Figures 4.58 – 4.60.

The significance of this is that for the specimen geometry of interest in this research, an additional variable needs to be fixed prior to fitting the HOLZ line pattern. For this reason, the amount of relaxation in the [110] (thinned) direction was calculated from the split HOLZ line patterns as was demonstrated in section 4.2.1. A chi-squared

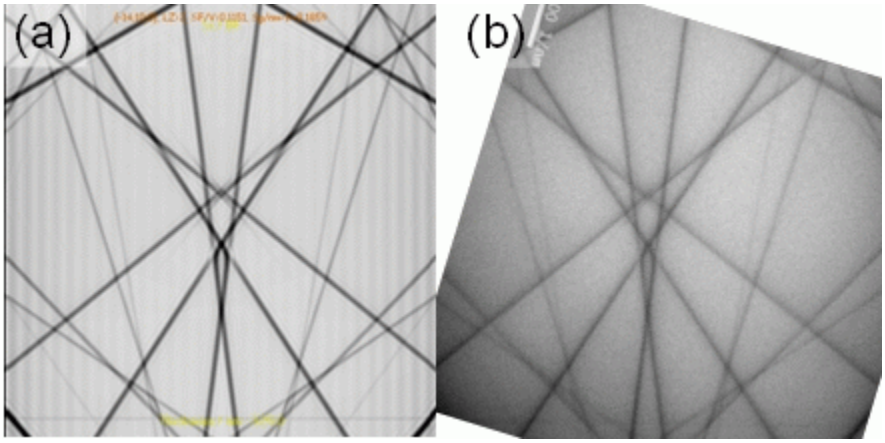

Figure 4.61 – (a) <230> Dynamical simulation of the HOLZ line pattern from the unstrained silicon using the best fit accelerating voltage calculated based on measurements from the experimental pattern shown in (b).

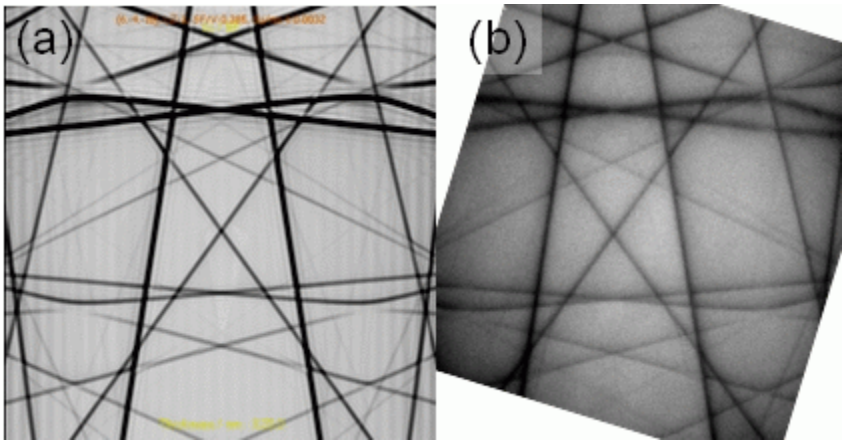

Figure 4.62 – (a) <340> Dynamical simulation of the HOLZ line pattern from the unstrained silicon using the best fit accelerating voltage calculated based on measurements from the experimental pattern shown in (b).

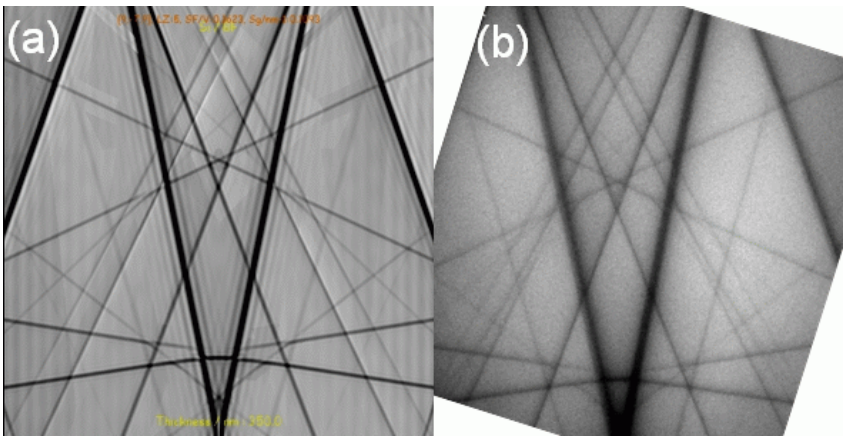

Figure 4.63 – (a) <670> Dynamical simulation of the HOLZ line pattern from the unstrained silicon using the best fit accelerating voltage calculated based on measurements from the experimental pattern shown in (b).

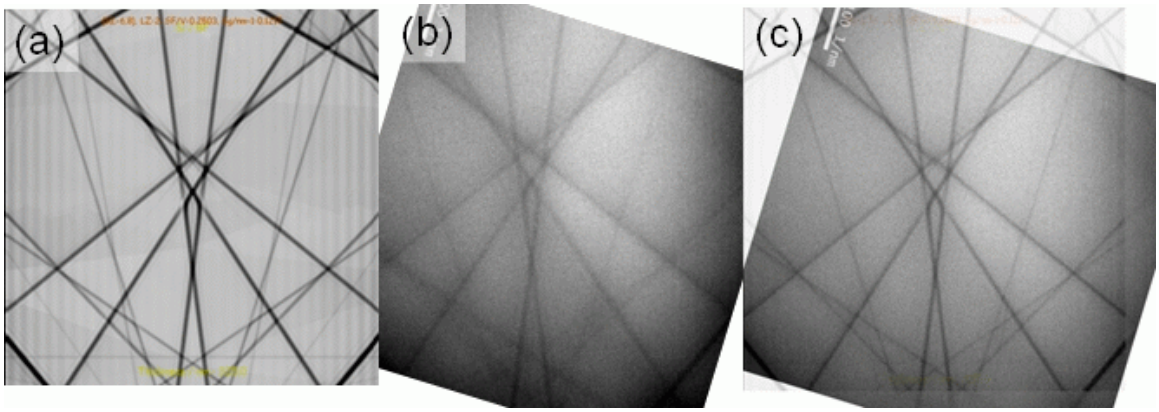

Figure 4.64 – (a) <230> Dynamical simulation, (b) experimental pattern, and (c) overlay of the dynamical simulation and experimental pattern from a strained region of the silicon 62 nm from the silicon/gate interface.

minimization was then performed using the other two variables as fitting parameters.

Dynamical simulations using the calculated values were compared with the experimental patterns to verify the goodness of fit. These are shown for the unstrained patterns in Figures 4.61 – 4.63. Some examples from the strained region of the sample are shown in Figures 4.64 – 4.66. Overlays of the experimental images on the dynamical images indicate excellent agreement.

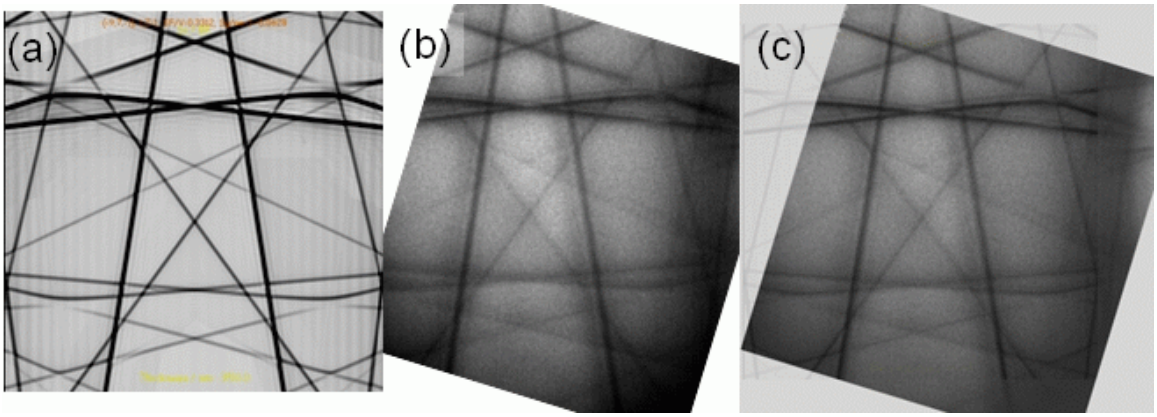

Figure 4.65 – (a) <340> Dynamical simulation, (b) experimental pattern, and (c) overlay of the dynamical simulation and experimental pattern from a strained region of the silicon 63 nm from the silicon/gate interface.

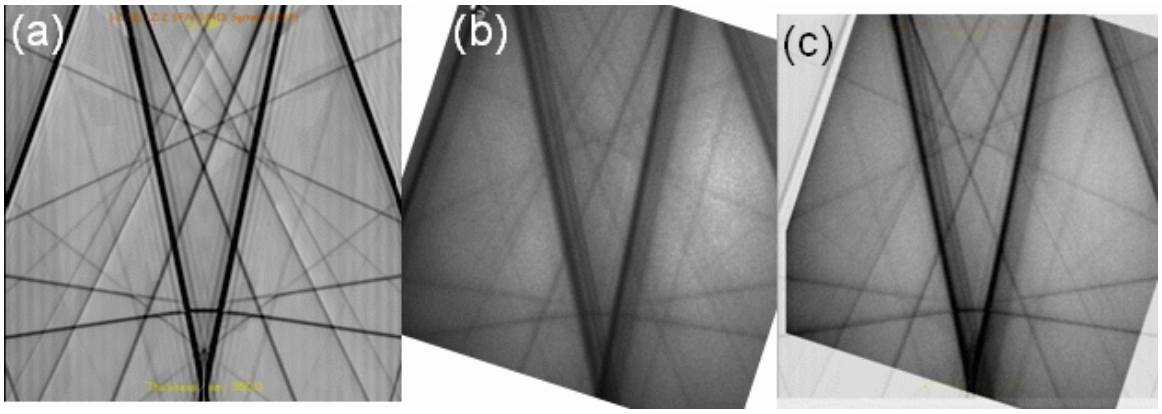

Figure 4.66 – (a) <670> Dynamical simulation, (b) experimental pattern, and (c) overlay of the dynamical simulation and experimental pattern from a strained region of the silicon 31 nm from the silicon/gate interface.

4.2.2.3.2 Strain Values in the MOSFET

Unsplit HOLZ line patterns showing shifts in positions from the unstrained state were collected at distances ranging 107 nm to 13 nm from the gate under the center of the gate. As mentioned in section 4.2.1.1.2.1, patterns that were collected from spots not centered under the gate channel exhibited HOLZ line splitting that suggests a variable strain state through the thickness of the specimen. Therefore strain values

could not be calculated from these patterns. Also, at distances less than 13 nm from the gate, clear patterns could not be collected from any of the zone axes.

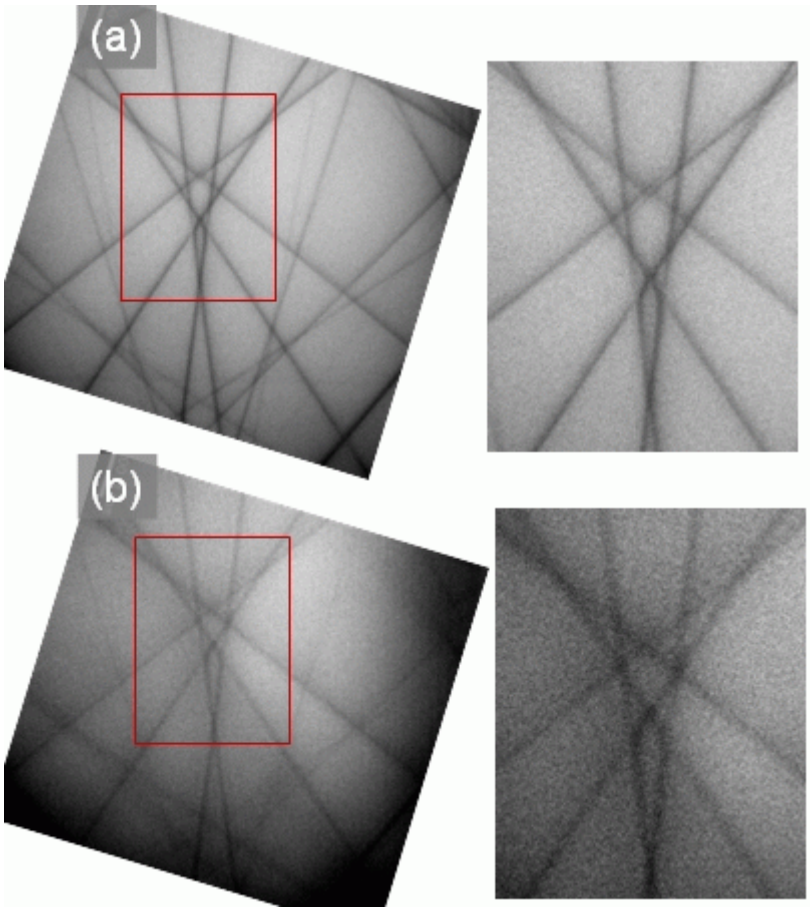

Figure 4.67 – Experimental <230> HOLZ line patterns from (a) the unstrained silicon and (b) a strained region of the silicon. The pictures on the right are magnified areas of a region where HOLZ line shifts are readily visually apparent.

Figures 4.67 – 4.69 compare HOLZ line images from the unstrained and strained regions of the MOSFET, indicating regions where the HOLZ line shifts are readily visually apparent. A series of the HOLZ line images at different distances from the gate for each zone axis are shown in Figures 4.70 - 4.72.

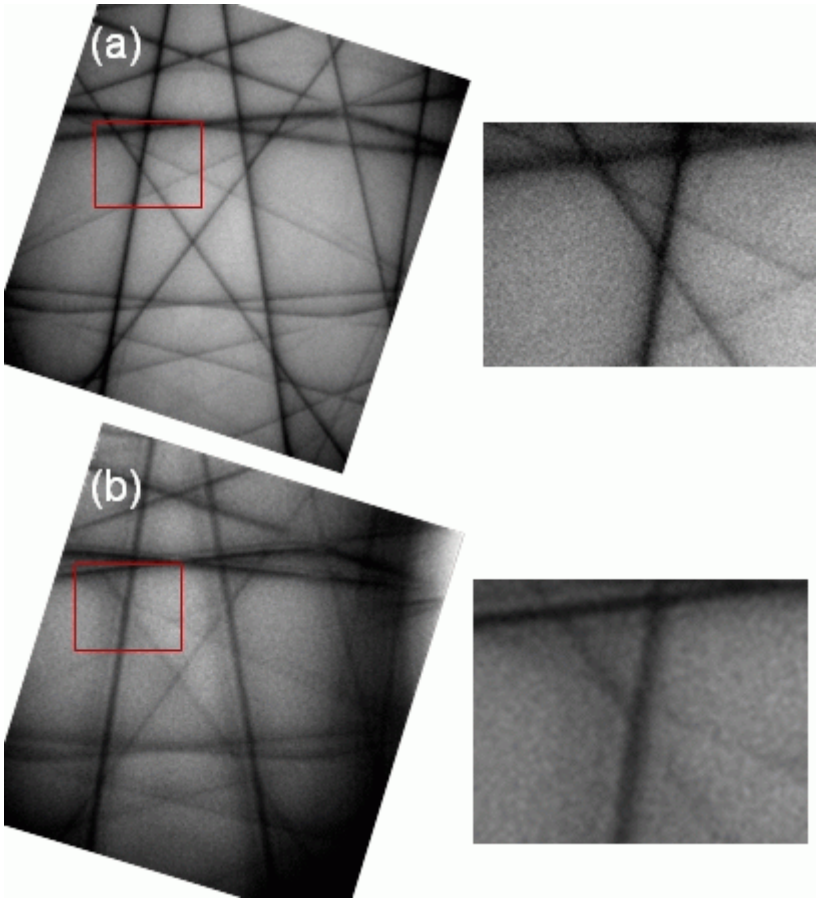

Figure 4.68 – Experimental <340> HOLZ line patterns from (a) the unstrained silicon and (b) a strained region of the silicon. The pictures on the right are magnified areas of a region where HOLZ line shifts are readily visually apparent.

While the nature of the relaxation through the thickness of the specimen far from the interface was uncertain from just the split HOLZ line patterns, the fact that clear, unsplit HOLZ line patterns could be collected near the gate suggests that the strain state through the thickness in this region is close to uniform.

From these images, the distances between the HOLZ line intersection points shown in Appendix B were measured. The relaxation measured from the split HOLZ line patterns farther from the interface was used to fix that variable, and the strain in the $[1\bar{1}0]$ and [001] directions were fit using a chi-squared minimization.

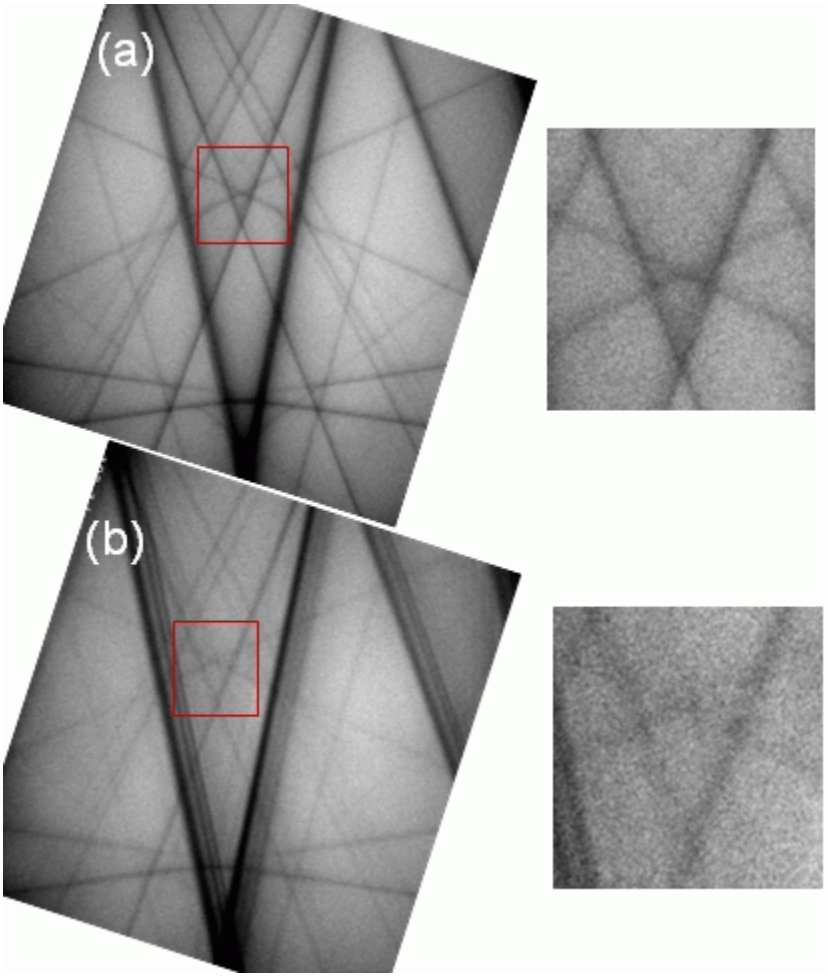

Figure 4.69 – Experimental <670> HOLZ line patterns from (a) the unstrained silicon and (b) a strained region of the silicon. The pictures on the right are magnified areas of a region where HOLZ line shifts are readily visually apparent.

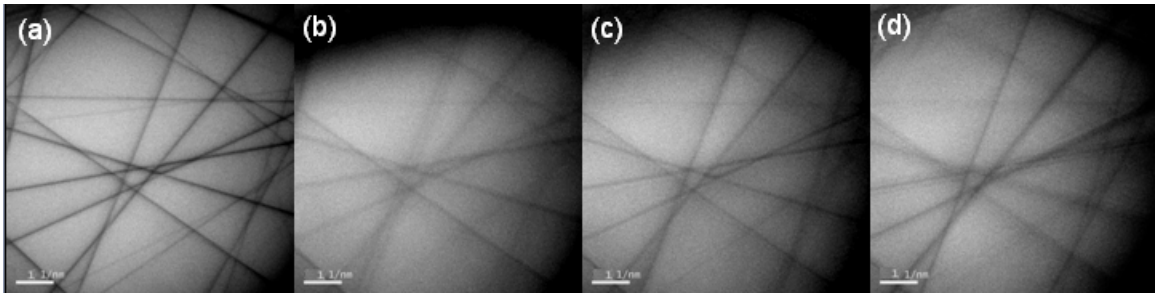

Figure 4.70 – Experimental <230> HOLZ line patterns with the electron beam centered under the gate from (a) unstrained silicon, (b) 95 nm, (c) 62 nm, and (d) 35 nm from the silicon/gate interface.

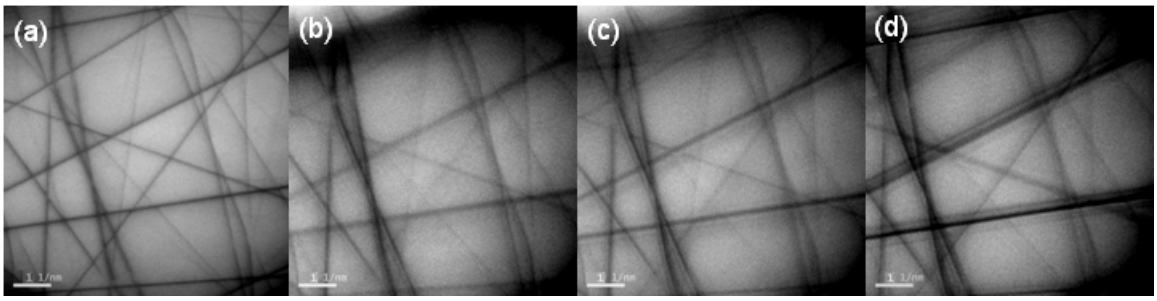

Figure 4.71 – Experimental <340> HOLZ line patterns with the electron beam centered under the gate from (a) unstrained silicon, (b) 101 nm, (c) 63 nm, and (d) 19 nm from the silicon/gate interface.

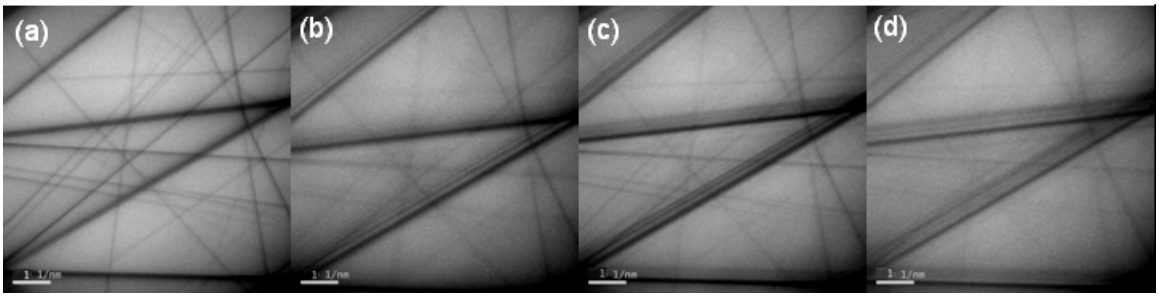

Figure 4.72 – Experimental <670> HOLZ line patterns with the electron beam centered under the gate from (a) unstrained silicon, (b) 50 nm, (c) 31 nm, and (d) 13 nm from the silicon/gate interface.

Graphs of the strain in the $[1\bar{1}0]$ direction as determined from the individual zone axes are shown in Figures 4.73 – 4.75. For each of the zone axes, the $[1\bar{1}0]$ strain was found to show a continuous increase in compressive strain as distance from the gate decreased. At distances greater than 80 nm from the interface, the strain values are around zero. The <340> axis measurements even indicate a slight tensile strain at these depths. For the regions closest to the gate for which clear HOLZ lines patterns were collected the measured strain was around -1.0%. Overall, all three zone axes show excellent agreement on the $[1\bar{1}0]$ strain values as shown in Figure 4.76

where all three data sets are combined. This strain behavior indicates that the desired compressive strain along the channel direction is achieved by this MOSFET structure.

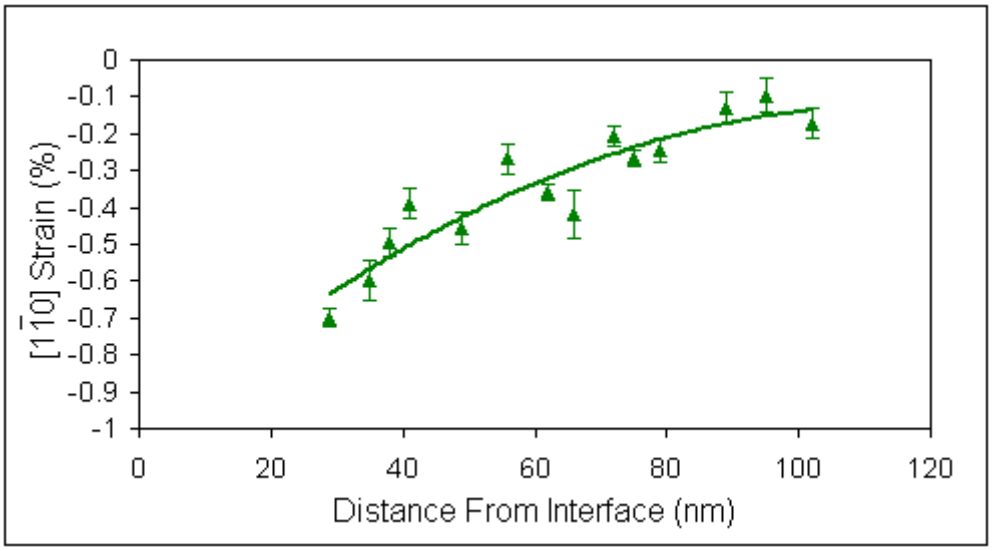

Figure 4.73 – The [1$\bar{1}$0] strain in the gate channel as a function of distance from the gate/silicon interface as measured using the <230> zone axis.

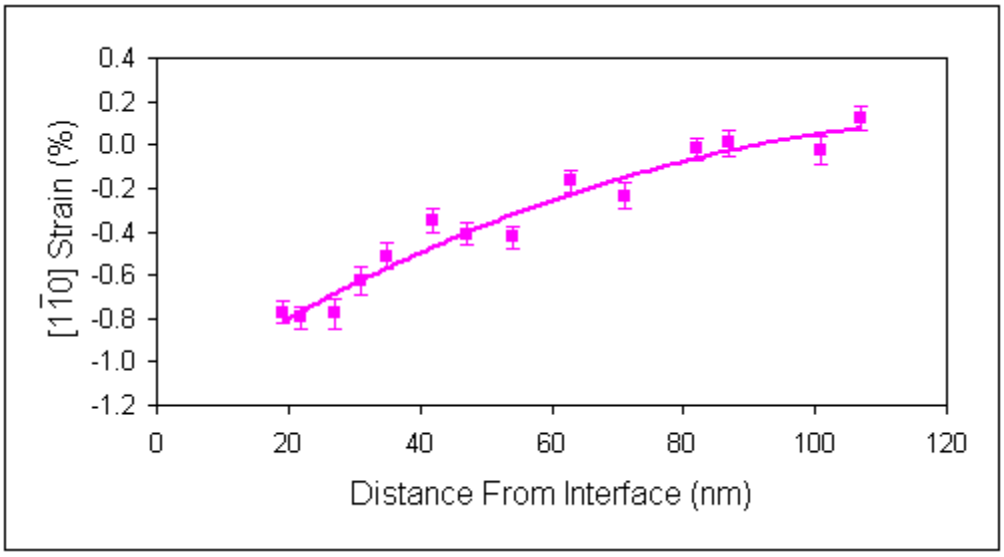

Figure 4.74 – The [1$\bar{1}$0] strain in the gate channel as a function of distance from the gate/silicon interface as measured using the <340> zone axis.

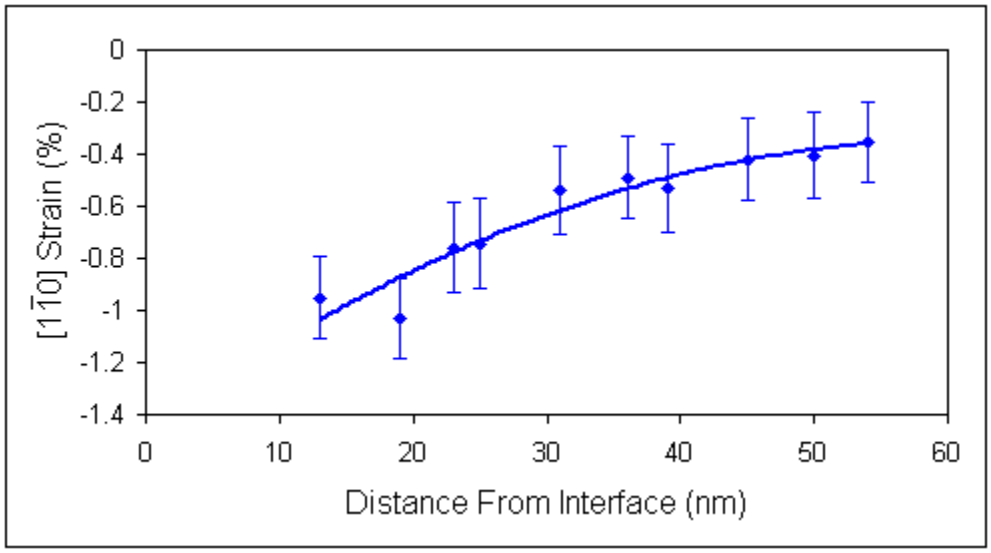

Figure 4.75 – The [1$\bar{1}$0] strain in the gate channel as a function of distance from the gate/silicon interface as measured using the <670> zone axis.

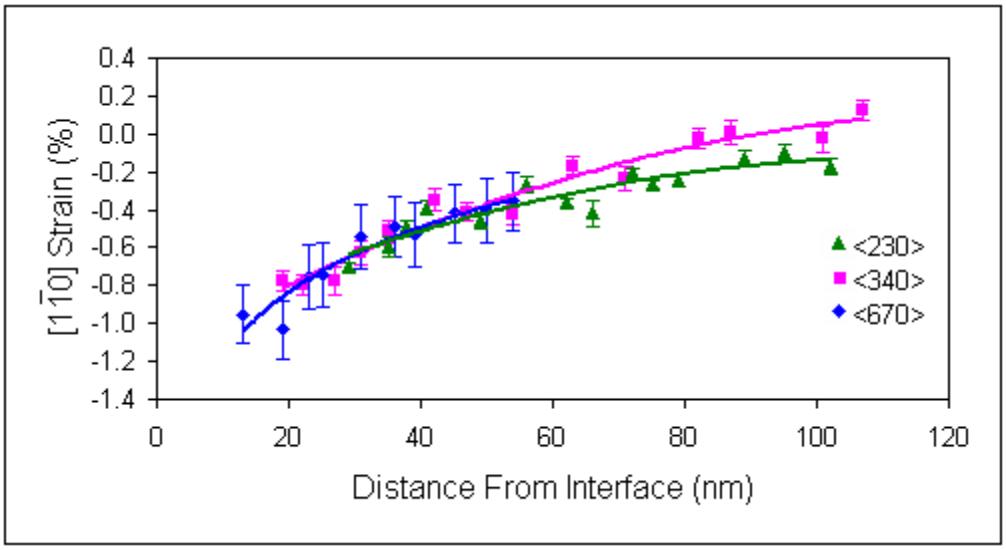

Figure 4.76 – The [1$\bar{1}$0] strain in the gate channel as a function of distance from the gate/silicon interface showing the combined results of all three zone axes.

Graphs of the strain in the [001] direction as determined from the individual zone axes are shown in Figures 4.77 – 4.79. In this direction, the strain starts out as compressive far from the interface and gradually shifts to tensile around 50 nm from the interface, with a maximum tensile strain around 0.3% close to the gate. The different

zone axes all show the same trend in the [001] strain, but do show some differences in value as shown in Figure 4.80. The <670> zone axis values exhibited the least change

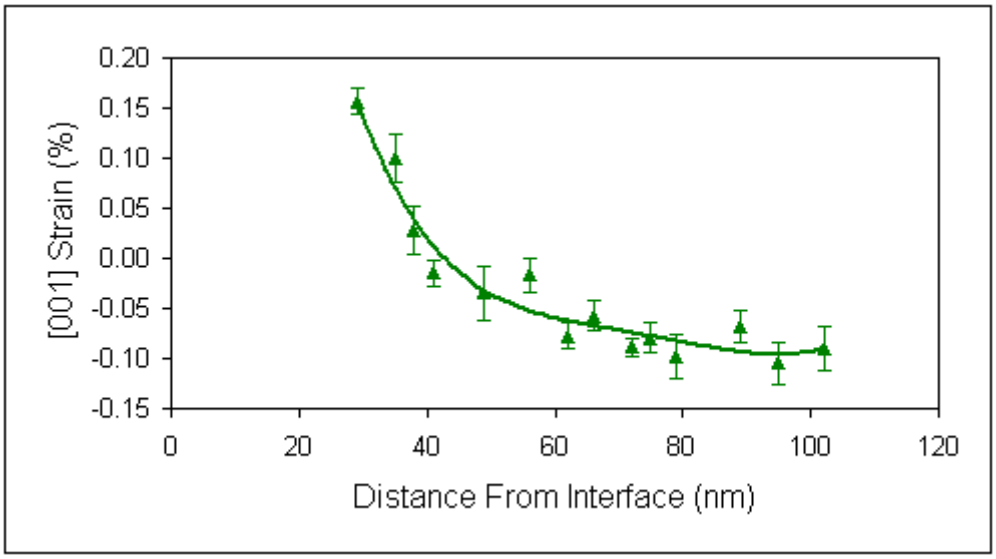

Figure 4.77 – The [001] strain in the gate channel as a function of distance from the gate/silicon interface as measured using the <230> zone axis.

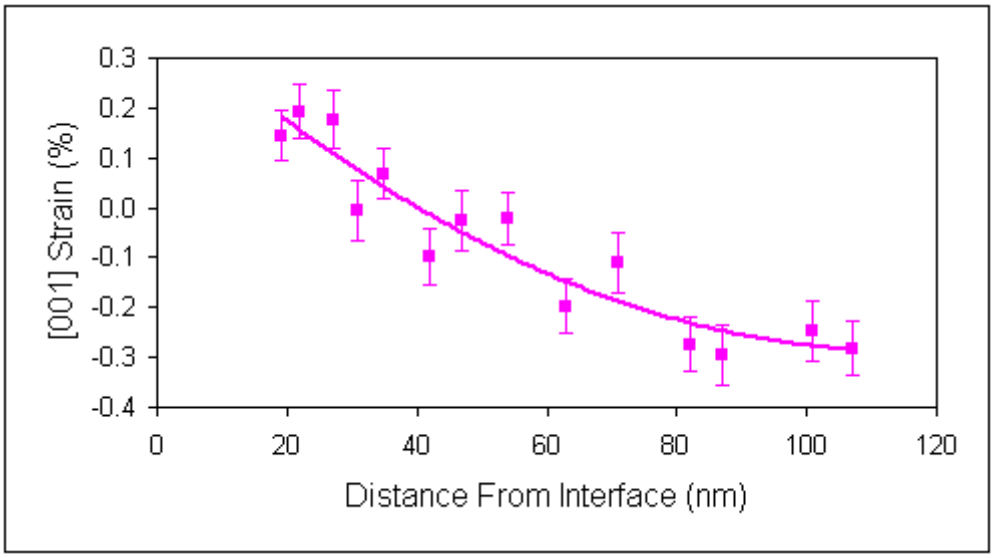

Figure 4.78 – The [001] strain in the gate channel as a function of distance from the gate/silicon interface as measured using the <230> zone axis.

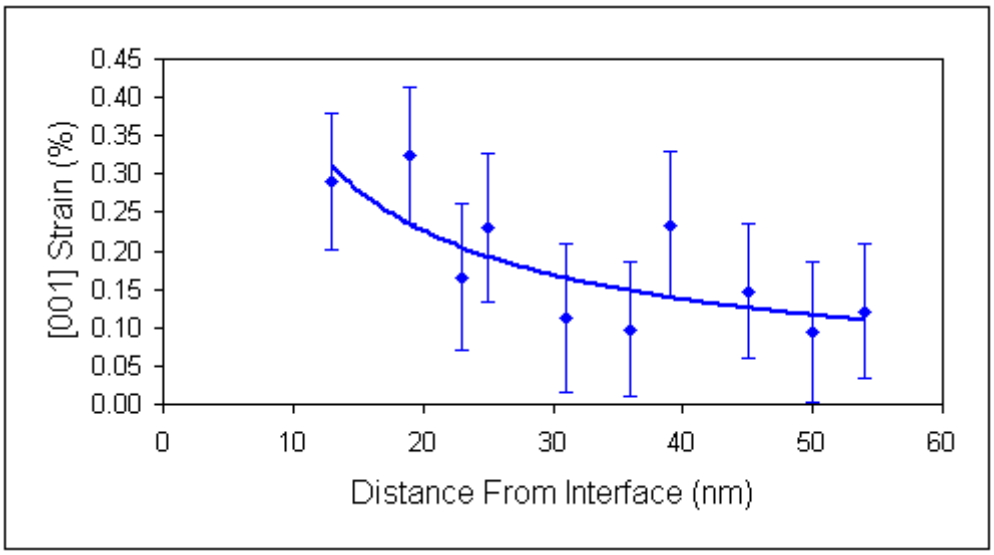

Figure 4.79 – The [001] strain in the gate channel as a function of distance from the gate/silicon interface as measured using the <230> zone axis.

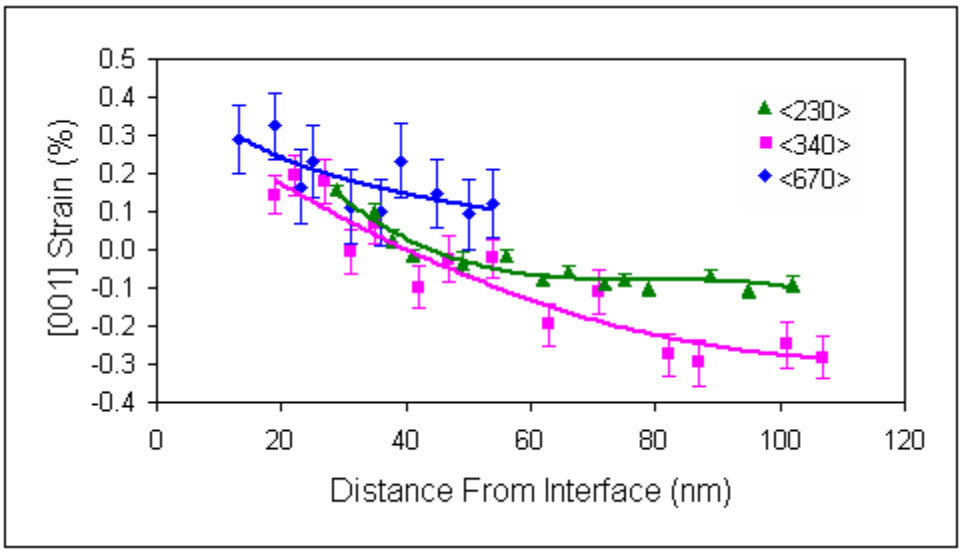

Figure 4.80 – The [001] strain in the gate channel as a function of distance from the gate/silicon interface showing the combined results of all three zone axes.

over the measured range, and were slightly more tensile than the values from the other zone axes for distances greater than 40 nm from the interface. The <340> zone axes values were slightly more compressive than those from the <230> zone axis at distances greater than 80 nm from the interface.

Finite element (FE) calculations can be used to simulate the stress and strain behavior in complex geometries. While FE calculations were not performed on this particular geometry for this research, the findings from FE studies on a similar system provide a useful basis for comparison.

Yeo and Sun [74] found that for 20 nm deep $Si_{.75}Ge_{.25}$ stressors with a 50 nm gate length, the major strain components were lateral and vertical, corresponding to the $[1\bar{1}0]$ and [001] directions in this work, respectively. The strains were fairly uniform across the gate channel, with sharp changes in the strain state being confined to the outer 20% of the gate channel.

Similar strain trends as this experimental work were also seen in the finite element simulation, shown in Figure 4.81. In that simulation, the $[1\bar{1}0]$ strain showed a continuously increasing compressive value upon approaching the gate. Below the depth of the stressors, a slight tensile strain was apparent. The [001] strain showed a change from compressive to tensile strain within the channel region, with increasing tensile strains closer to the gate. All of these finite element simulated strain phenomena are consistent with what was experimentally determined in this research. Additionally, they make physical sense, as the SiGe near the top of the stressor is less confined in the $[1\bar{1}0]$ direction by the silicon substrate, thus producing a greater compressive strain. Also, the [001] tensile behavior closer to the gate is a result of a combination of the tensile force in that direction produced by the SiGe stressors and a Poisson effect due to the compressive strain along the $[1\bar{1}0]$ direction.

However, there are differences between the structure simulated by Yeo and Sun and the structure experimentally measured here. They looked at a germanium

concentration of 25%, a gate length of 50 nm, and 20 nm deep square shaped stressors. In this research, the germanium concentration was 15%, the gate length 40 nm, and the stressors were rounded and 80 nm deep. The greater depth of the stressors in the experimental structure could lead to larger $[1\bar{1}0]$ compressive strain

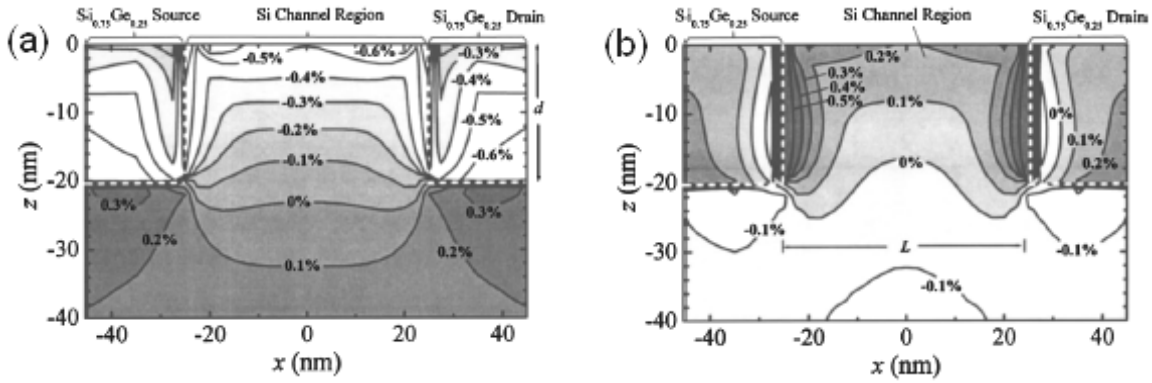

Figure 4.81 – Finite element simulations of (a) $[1\bar{1}0]$ strain and (b) [001] strain in a MOSFET structure with recessed SiGe stressors. Reprinted with permission from [74]. © 2005, American Institute of Physics.

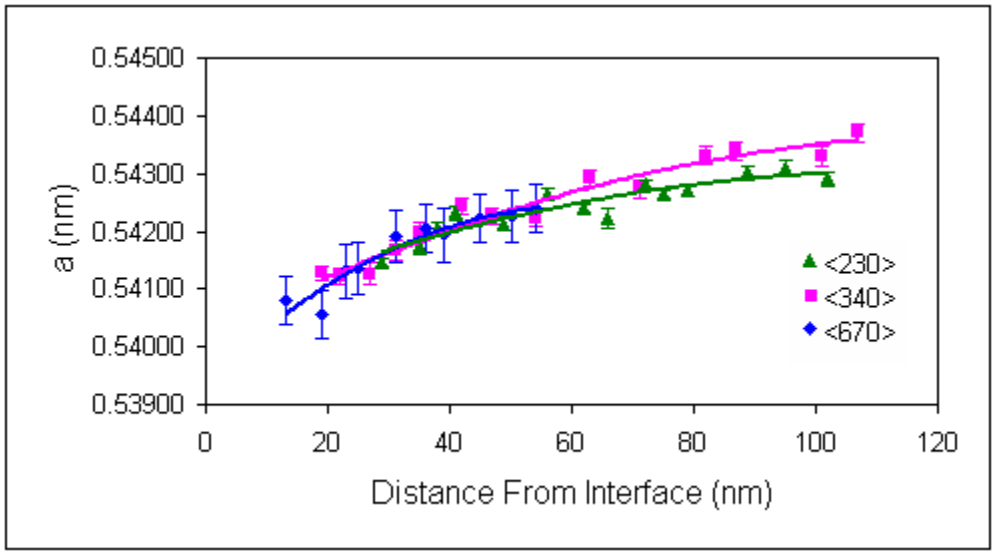

Figure 4.82 – The values of the a lattice parameter of the silicon unit cell calculated from the measured strain values as a function of distance from the silicon/gate interface.

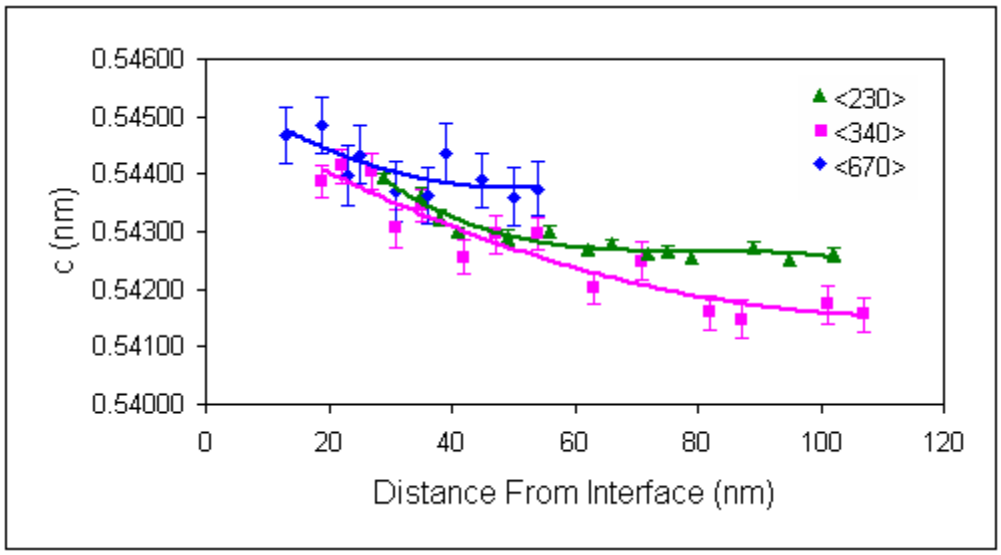

Figure 4.83 – The values of the c lattice parameter of the silicon unit cell calculated from the measured strain values as a function of distance from the silicon/gate interface.

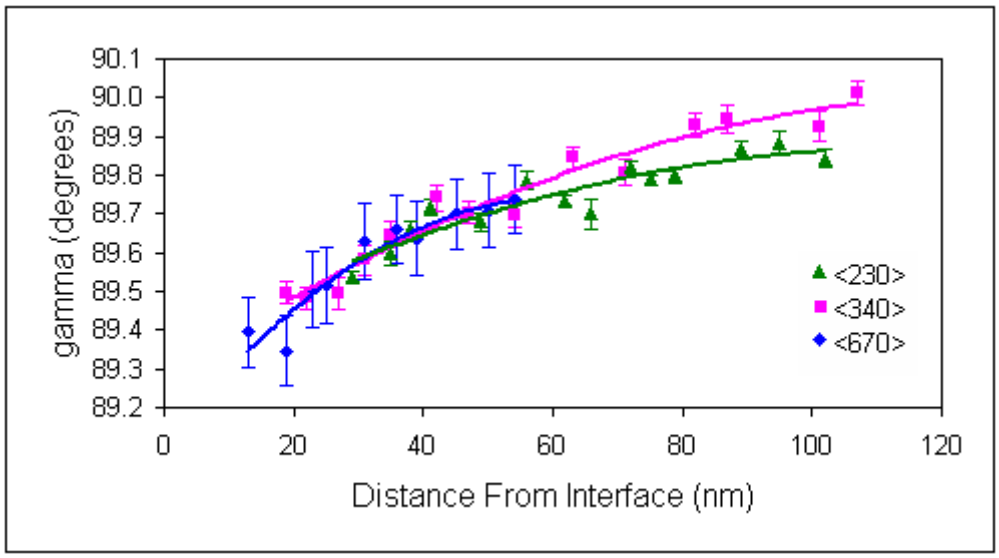

Figure 4.84 – The values of the γ lattice parameter of the silicon unit cell calculated from the measured strain values as a function of distance from the silicon/gate interface.

values and larger [001] tensile strain values near the gate than were seen in the simulation. Also, the rounded shape of the SiGe structures should result in these strain values decreasing faster than for square stressors as a function of the distance from the

gate. A finite element simulation better matching the experimental structure should be performed for exact quantitative comparison to these values measured by CBED. Conversion of the strains to the principal axes of the silicon allows for the determination

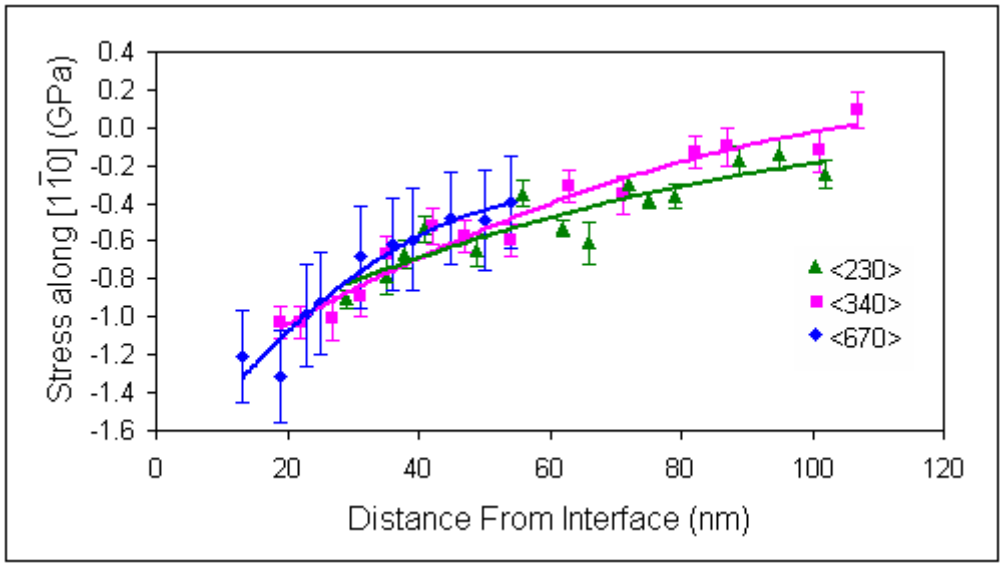

Figure 4.85 – The stress along the [1$\bar{1}$0] direction as a function of distance from the silicon/gate interface.

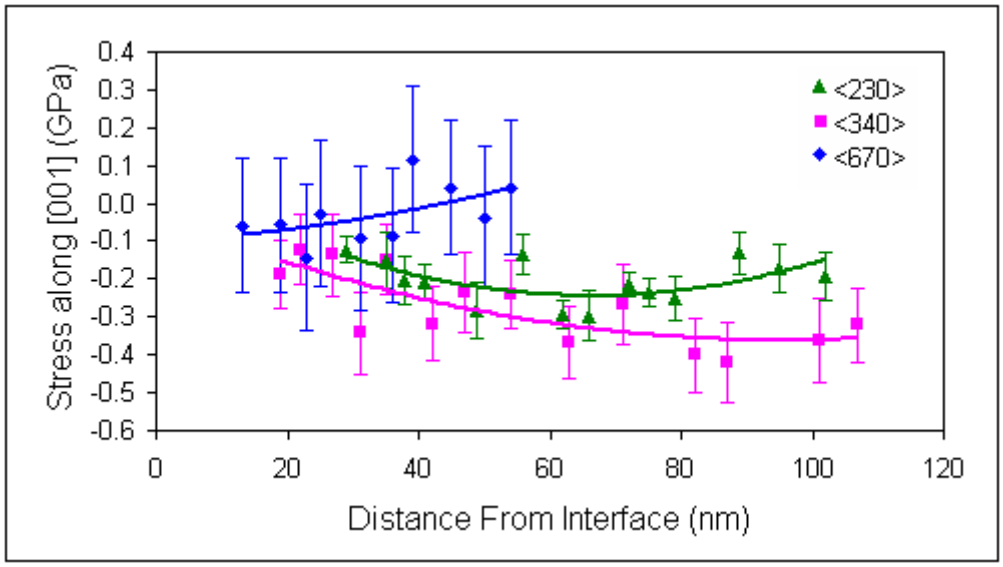

Figure 4.86 – The stress along the [001] direction as a function of distance from the silicon/gate interface.

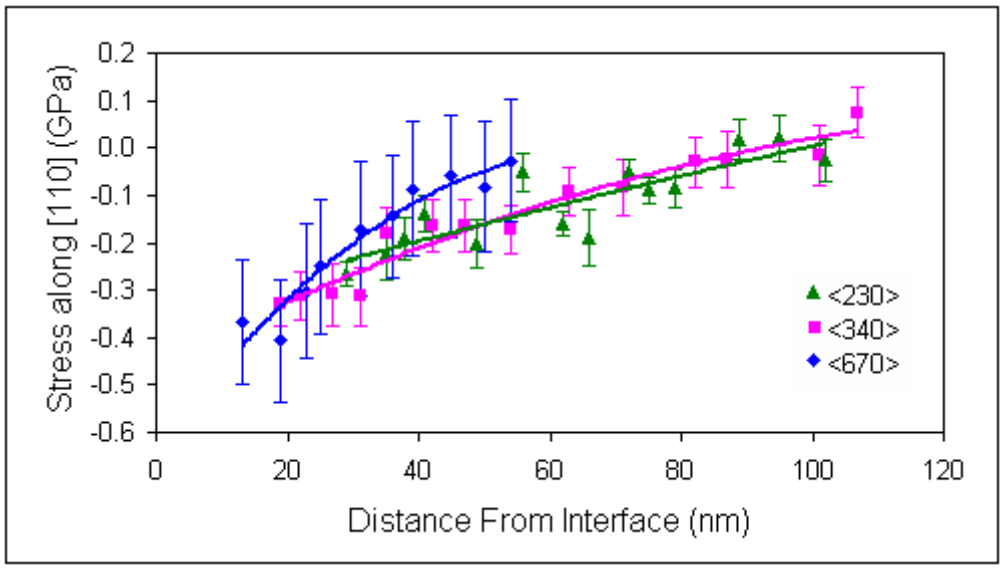

Figure 4.87 – The stress along the [110] direction as a function of distance from the silicon/gate interface.

of the lattice parameters a, c, and γ at each of these points. These results are shown in Figures 4.82 – 4.84.

The strain values can then be turned into estimates of stresses using the bulk elastic stiffness values for silicon:

$$\sigma_{11} = C_{11}\varepsilon_{11} + C_{12}\varepsilon_{22} + C_{12}\varepsilon_{33} \quad (4.22)$$

$$\sigma_{22} = C_{12}\varepsilon_{11} + C_{11}\varepsilon_{22} + C_{12}\varepsilon_{33} \quad (4.23)$$

$$\sigma_{33} = C_{12}\varepsilon_{11} + C_{12}\varepsilon_{22} + C_{11}\varepsilon_{33} \quad (4.24)$$

$$\sigma_{12} = \sigma_{21} = C_{44}\varepsilon_{12} \quad (4.25)$$

$$C_{11} = 165.8GPa \quad (4.26)$$

$$C_{12} = 63.9GPa \quad (4.27)$$

$$C_{44} = 79.6GPa \quad (4.28)$$

where σ_{ij} are the stress values, ε_{ij} the strain values, and C_{ij} the stiffness constants for silicon [40]. Figures 4.85 – 4.87 show the stress values along the principal strain axes.

The compressive stress along the $[1\bar{1}0]$ direction was found to increase as distance from the gate decreased with a maximum measured value around -1.3 GPa. The [110] axis was determined to also have an increasing compressive stress as a function of decreasing distance from the gate. This is due to the material above the gate channel and SiGe stressors restraining them from further expansion in this direction. The thinning of the specimen did reduce some of the constraint along this direction allowing for some relaxation as has been discussed. This could explain the near zero stress value at 80 nm, the depth of the SiGe structures. However, the compressive strain in the $[1\bar{1}0]$ direction increases upon closer approach to the gate, but no further expansion occurs in the [110] direction, therefore, an increasing compressive stress is seen. The [001] stress was found to be slightly compressive with the data from the <230> and <340> axes. The <670> axis measurements indicate virtually no stress in this direction. No clear trend in the [001] stress behavior as a function of distance is apparent.

4.2.2.3.3 Importance of Lateral Resolution

One of the goals of this research was to examine the importance of the zone axis used for strain measurement via CBED and to find a zone axis which improves the lateral resolution of strain measurement in silicon.

The <230>, <340>, and <670> zone axes produced generally similar trends, but there were some differences. With the <230> axis, the closest distance from the interface for which a clear HOLZ line pattern could be obtained was 29 nm. For the

<340> axis this distance decreased to 19 nm. And for the <670> axis it was 13 nm. This is clearly an effect of the improved lateral resolution by moving to smaller tilts away from the <110> axis. The finite element simulation in Figure 4.81 shows large strain gradients in the gate channel near the SiGe stressors. Since the SiGe structures examined in this research are rounded, the region of high stain gradient most likely moves closer to the center of the gate channel as the SiGe structure widens. This is shown schematically in Figure 4.88. Therefore, the images taken using larger tilts from <110> will blur at distances farther from the interface than those taken smaller tilts. At distances greater than 55 nm from the silicon/gate interface, useable patterns from the <670> were not able to be obtained. It is not clear why as this was not a problem with other two zone axes. Perhaps toward the center of the channel at those depths the strain gradient is higher. Additionally, the HOLZ lines from the <670> axis used for measurement were generally weaker and therefore more sensitive to decreased intensity.

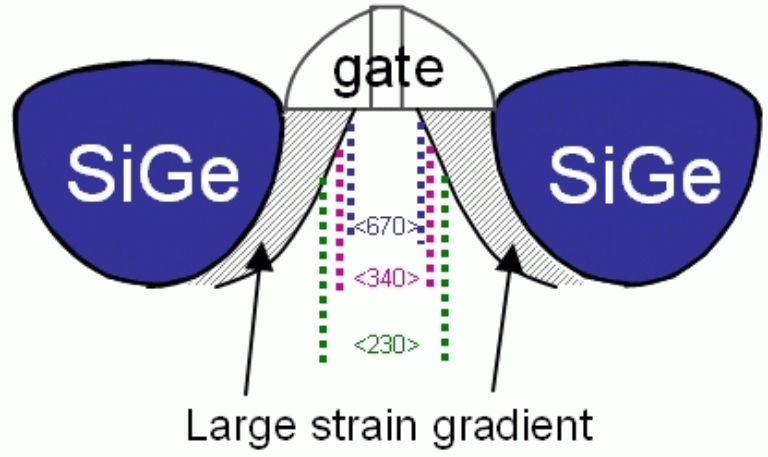

Figure 4.88 – Schematic illustration of how axes with smaller tilts from <110> allow for clear HOLZ line images closer to the silicon/gate interface. The dashed lines indicate the lateral distance covered by the electron beam through the specimen for each axis.

Another marked difference between the zone axes was the uncertainty in the measured values. The values determined from the <230> axis had the least uncertainty and those from the <670> axis had the greatest. The reasons for this are discussed in more detail in Section 4.2.2.3.5.

One additional issue is the potential for these zone axes actually to be sampling different strain states in the specimen due to the electron beam interacting with different volumetric regions. Small differences appear between the <230> and <340> axis $[1\bar{1}0]$ strain measurements greater than 80 nm from the interface (Figure 4.76). These may reflect real differences in the strain states of the two sampled regions. Figure 4.81 indicates that at regions below the depth of the SiGe stressors, the compressive strain switches to tensile and this tensile strain is greater toward the center of the channel than toward the edges. The <340> axis having a smaller tilt from <110> than the <230> axis samples a volume closer to the center of the channel and might, therefore, be expected to exhibit this result. That is indeed what was observed experimentally. These zone axes also exhibit slightly different strain results for the [001] direction (Figure 4.77). Figure 4.81 shows the simulated change in the [001] strain state is more compressive toward the center of the channel region at distances greater than the depth of the SiGe stressors. In this region, the experimental <340> measurements show a slightly greater compressive strain than the <230> axis. The <670> axis [001] strain values are slightly more tensile than the measurements from the other two zone axes at distances greater than 40 nm from the interface. The reason for this is not known. It is unclear if the rounded structure of the SiGe stressors may play a role in these small differences, so their effect on the strain state warrants further investigation.

4.2.2.3.4 Effect of Relaxation on Fitting HOLZ Line Patterns

As was discussed previously, it was necessary to fix the relaxation in the [110] direction in order to obtain a unique fit to the HOLZ line patterns. This was done by calculating the relaxation based on the HOLZ line splitting behavior. A more commonly employed approach is to assume a plane strain condition [30, 72], which would fix the relaxation value at 0. However, other researchers have found that taking relaxation into account when fitting HOLZ line patterns was necessary to obtain good agreement with strain values as determined by other methods [75-76]. This section looks at the error introduced in fitting the HOLZ patterns by assuming no relaxation of the specimen in the thinned direction.

The HOLZ line fits with this assumption were calculated in the same manner as before using the chi-squared minimization. Graphs comparing the values taking relaxation into account and those assuming no relaxation for the <230> zone axis are

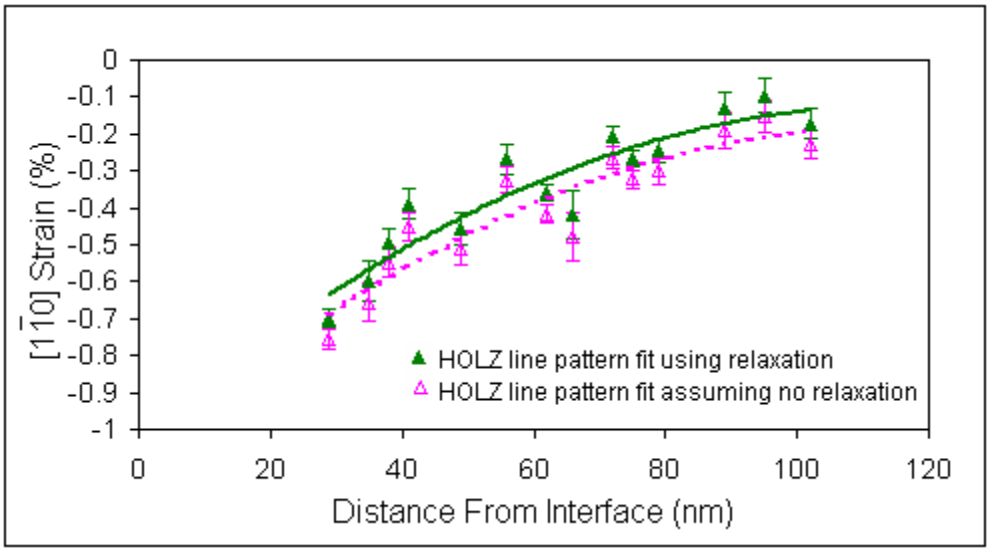

Figure 4.89 – [1$\bar{1}$0] strain as determined from the <230> HOLZ line patterns using the calculated [110] relaxation and the assumption of no [110] relaxation.

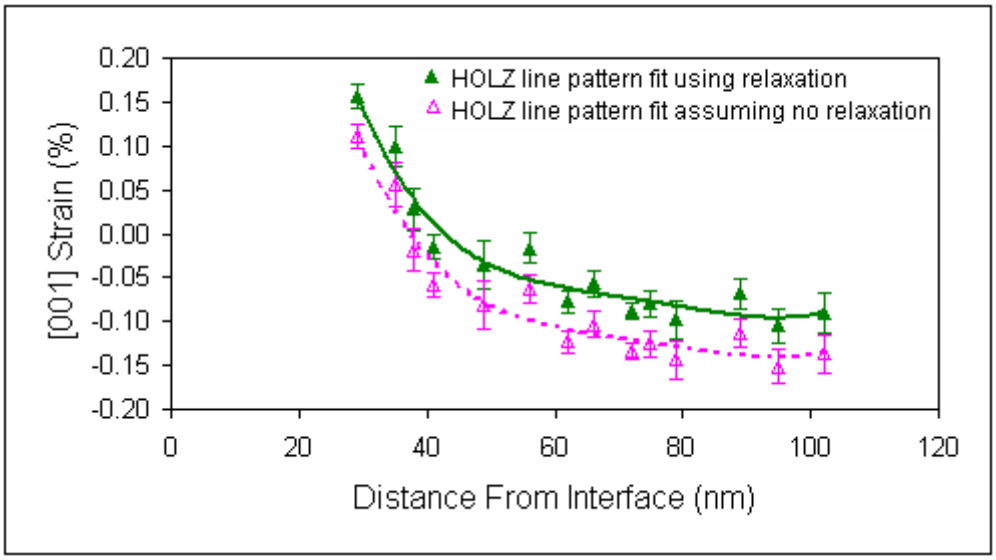

Figure 4.90 – [001] strain as determined from the <230> HOLZ line patterns using the calculated [110] relaxation and the assumption of no [110] relaxation.

shown in Figures 4.89 and 4.90. Similar behavior was seen for the other two axes.

This assumption results in the shift of each of the data points by a fixed value. The shift was negative for all strains and zone axes. That is, the strain is shifted toward greater compressive values and lower tensile values. It was also discovered that the magnitude of the shift was different between the strain directions for a given zone axis and also for a given strain direction between the different zone axes. The magnitudes of the shift in strain values for each zone axis from this structure are shown in Table 4.5. The values calculated fitting the patterns using this assumption were found to generally fall within the scatter and uncertainty of the values calculated taking the relaxation into account. However, since this assumption results in non-random errors (it always shifts the strain values in the negative direction), it can introduce significant deviations in calculations using these values, such as stress value calculations. The plane strain

assumption introduces an additional error when attempting to back out the strain values of the bulk structure for the values measured from the relaxed TEM specimen. This is discussed in section 4.2.2.3.6.

Table 4.5 – The shift in strain values calculated using the plane strain assumption as compared to that calculated taking the relaxation into account.

	$[1\bar{1}0]$ strain shift (%)	[001] strain shift (%)
<230> axis	-0.06	-0.05
<340> axis	-0.05	-0.05
<670> axis	-0.09	-0.03

4.2.2.3.5 Sources of Error

There are many potential sources for error in these measurements, including the assumption of no shear strain, the acceleration voltage determination, the relaxation determination, and the HOLZ line intersection point determination. These show up in the variations of the individual intersection point values from the calculated chi-squared best fit values. For clear HOLZ lines it was determined that the HOLZ line intersections could be determined within .042 nm^{-1} or 0.003 degrees. For some patterns, certain HOLZ lines exhibit some blurring. For these, the strongest central part of the HOLZ line was used in the determining the intersection points. Patterns with no clear intersection point were not used in the strain analysis. The uncertainty from these sources varied from pattern to pattern, but the typical variation in strain was the same for all three zone axes, around $\pm$ 0.04%.

Another source for uncertainty is in being able to distinguish changes between HOLZ line patterns with different strain values. In other words, how much change in the strain values is necessary to produce detectable differences in the HOLZ line pattern.

This shows up in how quickly the chi-squared parameter converges to the minimum value. This varied greatly depending on the zone axis. For the <230> axis, the chi-squared fit converged rapidly to a solution, resulting in an uncertainty from this source of ± 0.02%. For the <340> and <670> axes, the chi-squared parameter did not converge to the minimum as quickly, resulting in a series of solutions that were indistinguishable from each other within the range of detectability. For the <340> axis, this range was ± 0.05% in both the $[1\bar{1}0]$ direction and the [001] direction. For the <670> axis it was ± 0.16% in the $[1\bar{1}0]$ direction and ± 0.09% in the [001] direction. For both of these cases, fixing either one of the strain directions eliminates the large uncertainty for the other direction. Figure 4.91 shows this range of uncertainty for a <340> pattern and a <670> pattern both collected 22 nm from the silicon/gate interface.

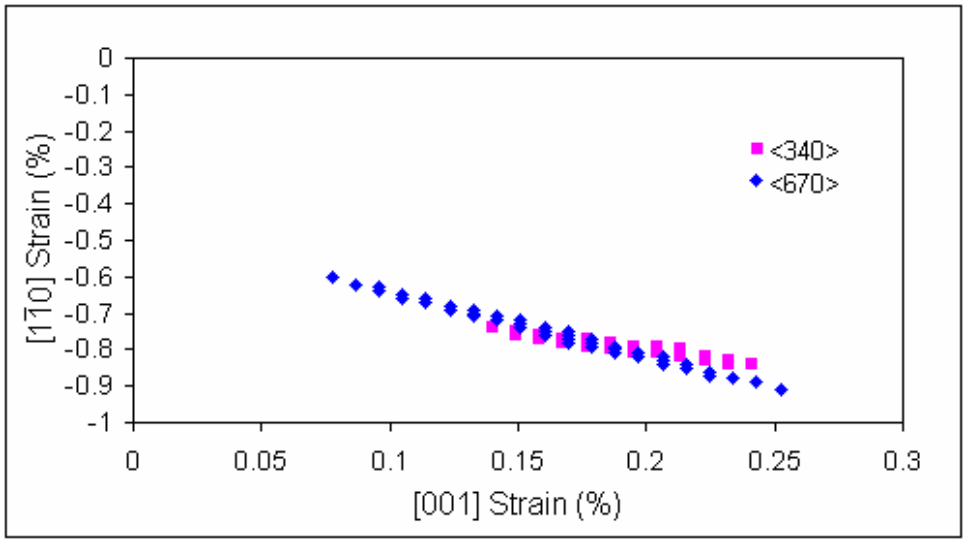

Figure 4.91 – The range of solutions over which the chi-squared values for the HOLZ line pattern fits are below the value of detectable differences for a point 22 nm from the silicon/gate interface as measured using the <340> and <670> axes.

4.2.2.3.6 Calculating the Strain Values in the Bulk

The importance of the specimen relaxation has been previously discussed in determining the best-fit values for a HOLZ line pattern. The calculation of relaxation is also important in attempting to determine the strain values in the bulk structure. If a plane strain assumption is made, then one of the directions is assumed to be unstrained. This research has shown that for a thinned TEM specimen of this structure, that assumption is invalid. Therefore, the strains that are measured in the TEM specimen are not those of the bulk structure.

One method of trying to determine the bulk strain values is through finite element analysis. Through this, a structure of the same thickness as the TEM specimen that simulates the experimentally measured values could then be simulated as a bulk structure. Research for which this was done has shown that for the structure investigated, the experimentally measured $[1\bar{1}0]$ compressive strain value of the TEM

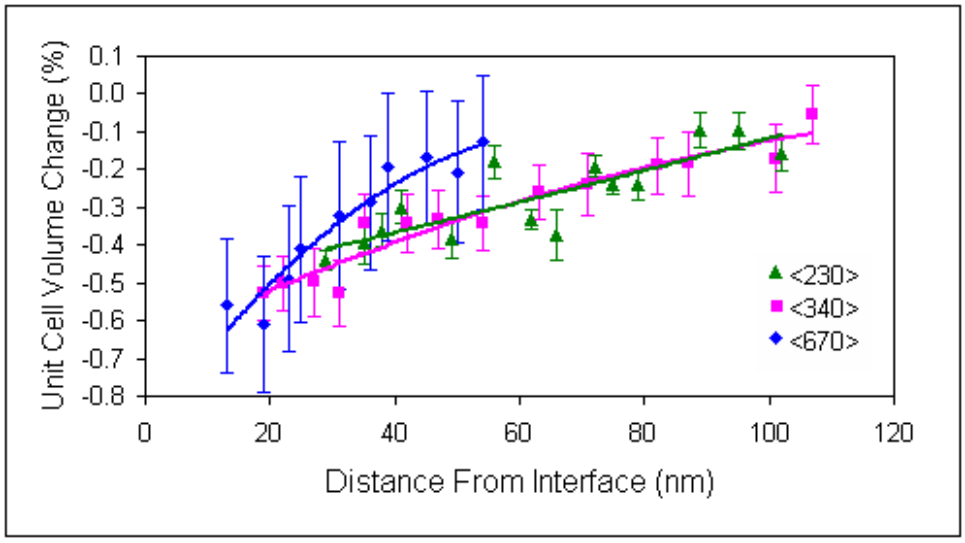

Figure 4.92 – Measured change in the unit cell volume as a function of distance from the silicon/gate interface.

specimen was about 20% greater than that of FE simulated bulk structure [77].

Another simpler method of estimating this effect is to compare the calculated relaxation strain to what would be expected based on the elastic compliance values for silicon. It has been shown that the compliance values of silicon change with volumetric changes [78]. However, for the volume changes observed in this research, shown in Figure 4.92, these compliance value deviations are less than 2%. Therefore, the bulk compliance values are used in this estimation.

For a uniaxial stress along the $[1\,\bar{1}\,0]$ axis, the following Poisson ratio relations can be shown [79]:

$$\nu_{110} = \frac{-(2S_{12} + S)}{(2S_{11} - S)} \tag{4.29}$$

$$\nu_{001} = \frac{-(2S_{12})}{(2S_{11} - S)} \tag{4.30}$$

where

$$S = S_{11} - S_{12} - \frac{S_{44}}{2} \tag{4.31}$$

$$S_{11} = -S_{12}\left(\frac{C_{11}}{C_{12}} + 1\right) \tag{4.32}$$

$$S_{12} = \frac{1}{C_{12}\left(\frac{C_{11}}{C_{12}} + 2\right)\left(-\frac{C_{11}}{C_{12}} + 1\right)} \tag{4.33}$$

$$S_{44} = \frac{1}{C_{44}} \tag{4.34}$$

ν_{110} and ν_{001} are the Poisson ratios for the 110 and 001 axes, respectively, S_{ij} are the compliance values, and C_{ij} are the stiffness values.

Using the stiffness values from equations 4.26 – 4.28 in equations 4.29 – 4.34 along with the measured $[1\bar{1}0]$ strain as a function of distance gives the expected strains in the [001] and [110] directions based on the Poisson ratios for uniaxial stress. The calculated and experimentally measured values for these directions are shown in Figures 4.93 and 4.94. Using this assumption, the measured [001] strains are less than the calculated values throughout the channel region. The calculated values do show fairly good agreement with the strain measurements from the <670> axis (see Figure 4.80). This suggests that the uniaxial stress state assumption may be more valid toward the center of the channel.

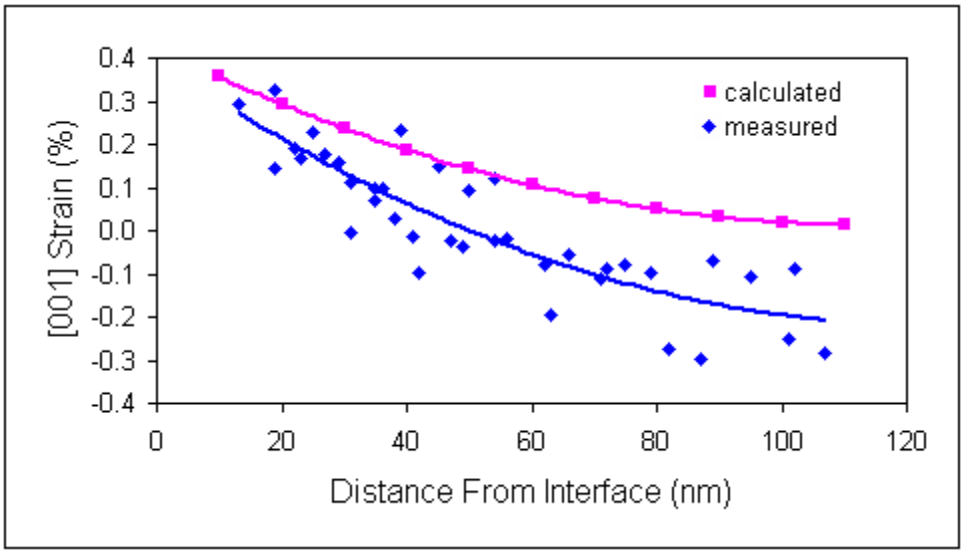

Figure 4.93 – Measured [001] strain for all axes as a function of distance and the [001] strain calculated using the measured $[1\bar{1}0]$ strain and the elastic constants of silicon assuming a uniaxial $[1\bar{1}0]$ stress condition.

The measured [110] strain based on the HOLZ line splitting behavior is greater than the calculated value throughout the channel region. This difference decreases as the distance from the silicon/gate interface decreases. This demonstrates that the

strain state of the thinned specimen is more complex than a simple Poisson effect from uniaxial stress. For both the [001] strain and the [110], the uniaxial $[1\bar{1}0]$ stress assumption appears to provide a better fit to the data at distances less than 20 nm from the interface. Even at these locations using this assumption, the measured $[1\bar{1}0]$ strain appears to be about 10-40% greater than that expected from the calculation.

The measured [110] strain being greater than the calculated value and the measured [001] strain being less than the calculated value are both consistent with strain relaxation in the [110] direction due to thinning of the specimen. These values suggest that the $[1\bar{1}0]$ compressive strain values measured in the TEM specimen are most likely higher than in the bulk structure.

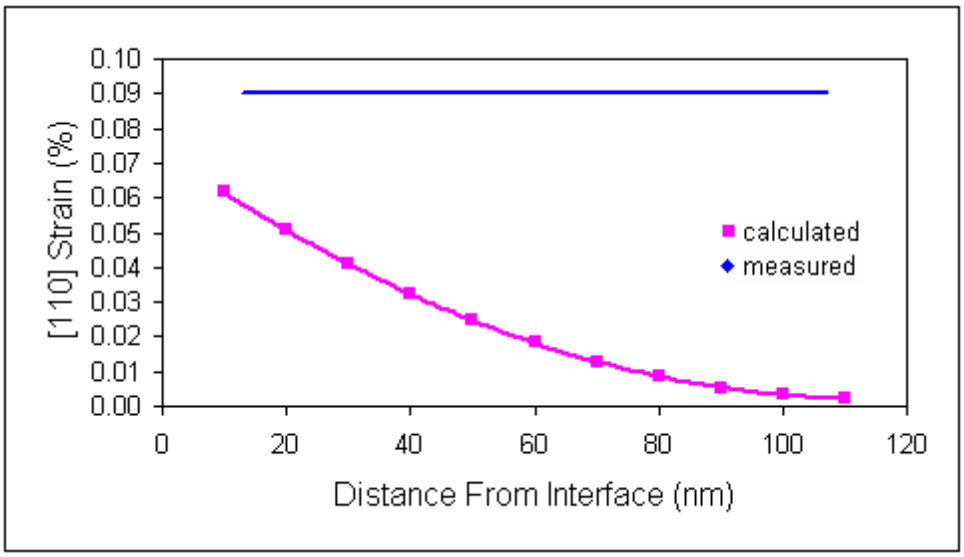

Figure 4.94 – Measured [110] strain based on the HOLZ line splitting curves and the [110] strain calculated using the measured $[1\bar{1}0]$ strain and the elastic constants of silicon assuming a uniaxial $[1\bar{1}0]$ stress condition.

For a biaxial stress along the $[1\bar{1}0]$ and [110] axes, the following strain relation can be shown [80]:

$$\varepsilon_{001} = \frac{-\nu_{001}}{1-\nu_{001}}(\varepsilon_{1\bar{1}0} + \varepsilon_{110}) \qquad (4.35)$$

where ε_{uvw} is the strain in the [uvw] direction. Using the measured $[1\bar{1}0]$ and [110] strains gives the expected strain in the [001] direction for a biaxial stress as shown in Figure 4.95.

Similar to the uniaxial assumption, the biaxial calculation using the measured $[1\bar{1}0]$ and [110] strains overestimates the [001] strain. However, the measured strain curve and the calculated biaxial values appear to have the same trend. By decreasing the measured [110] strain by 30% ($2.7\text{x}10^{-4}$) and the $[1\bar{1}0]$ strain by $3.4\text{x}10^{-3}$, which is

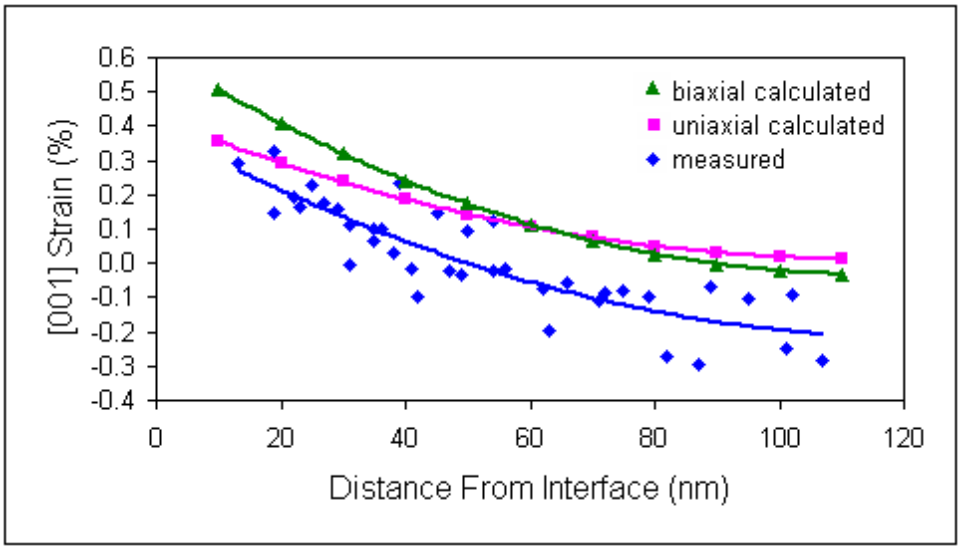

Figure 4.95 – Measured [001] strain for all axes as a function of distance and the [001] strain calculated assuming a $[1\bar{1}0]$ uniaxial stress and a $[1\bar{1}0]$ and [110] biaxial stress.

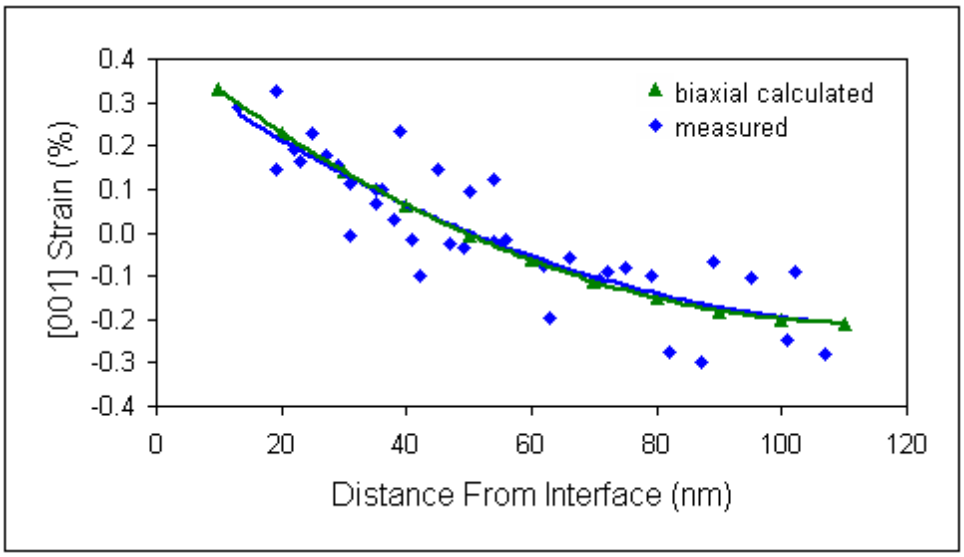

Figure 4.96 – Measured [001] strain for all axes as a function of distance and the [001] strain calculated assuming a [1$\bar{1}$0] and [110] biaxial stress using strain values 30% less than the maximum measured values.

30% of the maximum measured value, the [001] strain calculated from the biaxial stress falls on top of the measured strain curve. This is shown in Figure 4.96.

Assuming the [001] strain values are unchanged by thinning of the bulk device to make the TEM specimen, this gives an estimate of the [1$\bar{1}$0] and [110] strains in the channel region of the bulk device. From this, the [110] strain is 0.064% and the [1$\bar{1}$0] strain values are given as a function of distance from the interface in Figure 4.97. The above assumption means that essentially all of the [110] relaxation in the thinned specimen corresponds to an increase in the [1$\bar{1}$0] compressive strain. This may overestimate the difference in [1$\bar{1}$0] strain between the thinned specimen and the bulk structure because the relaxation in the [110] direction should also result in a decrease of the measured [001] strain relative to the bulk. Therefore the measured [1$\bar{1}$0] strain may be less than 30% greater than the bulk value. However, since the [1$\bar{1}$0] is the

main stress axis, it seems reasonable that the strain in this direction is affected more by the relaxation.

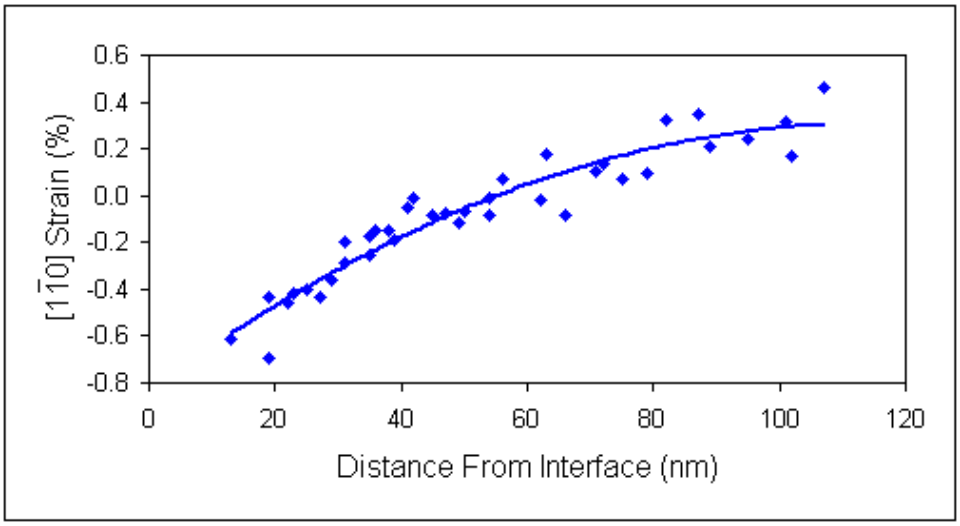

Figure 4.97 – Measured [1$\bar{1}$0] strain for all axes as a function of distance decreased by 30% of the maximum strain as an estimate of the strain in the bulk device.

CHAPTER 5

CONCLUSIONS

X-ray diffraction (XRD) and convergent beam electron diffraction (CBED) in the transmission electron microscope (TEM) have been used to study the strain and relaxation in two different SiGe on silicon blanket wafer systems.

1. XRD indicated that the film on wafer SiGe01 is 50 nm thick and has a composition of $Si_{.851}Ge_{.149}$ and the film on wafer SiGe02 is 126 nm thick and has a composition of $Si_{.788}Ge_{.212}$.

2. Both wafers had sharp interfaces between the SiGe and silicon and the SiGe film was lattice-matched with the silicon substrate resulting in a tetragonal distortion of the crystal structure with the c-axis being 0.99% longer than the a-axis in SiGe01 and 1.42% longer in SiGe02.

3. TEM specimens made from these wafers exhibited splitting of certain higher order Laue zone (HOLZ) lines in CBED patterns from the silicon substrate. The degree of the line splitting increased as the interface was approached and as specimen thickness increased.

4. The HOLZ line splitting was shown to result from rotational relaxation of the TEM specimen in the thinned direction with the degree of splitting correlating with the angular displacement.

5. Relaxation in SiGe01 specimens was shown to result in a maximum rotational displacement of about 0.2° on each side of the specimen.

6. The strain in the thinned direction of the silicon substrate at the interface with the SiGe was shown to be 0.16-0.20% for the SiGe01 specimens and 0.30-0.37% for the SiGe02 specimens. These values represent a relaxation of 29 – 45% of the bulk strain on the SiGe.

CBED was also used to determine the relaxation behavior of partially-processed and fully-processed metal oxide semiconductor field effect transistors (MOSFETs) with recessed SiGe structures.

1. In the partially-processed MOSFET TEM specimens, HOLZ line splitting was observed in the silicon below the SiGe structures and the gate structures. The splitting below the SiGe structures was similar to that observed for the blanket wafers; the degree of splitting below the gate showed a maximum at the depth of the SiGe structures then decreased closer to the gate.

2. HOLZ line splitting was also observed in the fully-processed MOSFET specimens. The degree of splitting was less than that of the partially-processed specimens and was not present at distances closer than 150 nm to the silicon/gate interface. This indicates that the additional material above the gate provide some constraint to relaxation, but did not prevent it entirely.

3. A schematic model of the relaxed structure of the fully-processed MOSFET was presented. The average relaxation in the thinned direction under the SiGe was 0.11% and under the gate was 0.09%.

The strain state of the silicon in the gate channel region of the fully-processed MOSFET was studied using HOLZ line simulations and experimental HOLZ line patterns.

1. Using a, c, and γ as independent variables does not produce a unique fit to an experimental silicon HOLZ line pattern for the <230>, <340>, or <670> axes.

2. The relaxation was calculated based on the HOLZ line splitting and used to fix the relationship between a and γ which allowed a unique solution to be produced for the experimental HOLZ line patterns.

3. The <230>, <340>, and <670> axes showed excellent agreement for the measured $[1\bar{1}0]$ strain values. The compressive strain in this direction

increases as the silicon/gate interface is approached, with a maximum measured strain value around -1%.

4. The [001] strain switched from compressive farther away from the gate to tensile closer to the gate, exhibiting a range of strains from -0.30% to 0.32%.

5. The $[1\bar{1}0]$ and [001] strain behavior showed good qualitative agreement with finite element simulations performed by other researchers.

6. The <670> axis allowed for the collection of clear HOLZ line patterns closer to the interface due to its better lateral resolution. However, this axis also provided the least precise measurement values.

7. Fitting experimental patterns using an assumption of no relaxation in the [110] direction shifted the best-fit strain values toward less tensile and more compressive values by around 0.06%.

8. Simple elasticity calculations indicate that the $[1\bar{1}0]$ compressive strain values measured in the thinned TEM specimens appear to be up to 30% greater than for the bulk structure near the interface. A biaxial stress assumption provides a better fit to the data than a uniaxial stress assumption.

CHAPTER 6

RECOMMENDATIONS FOR FUTURE WORK

1. Use other methods, such as XRD or ultraviolet Raman spectroscopy to quantify the relaxation in the blanket wafers.

2. Finite element simulations of the relaxed blanket wafer structures should be performed for comparison of strain and angular displacement values.

3. Dynamical HOLZ line simulations through relaxed blanket wafer and MOSFET structures could be used to determine the nature of the relaxation through the thickness of the specimens.

4. The roles of SiGe film thickness and germanium concentration on the blanket wafer relaxation behavior require further investigation.

5. Finite element simulations comparing thin and bulk MOSFET structure specimens would help validate and clarify the experimentally measured strain and relaxation.

APPENDIX A

MEASUREMENT OF ADDITIONAL LENGTH DUE TO ROTATIONAL RELAXATION

The rotational relaxation of a specimen is shown schematically in Figure A.1. By fitting a triangle to this region, it is apparent through geometry that the values of distance over which the relaxation takes place (Δx in the figure) and the average angle of rotation (θ in the figure) are sufficient to calculate the additional length in the thinned direction.

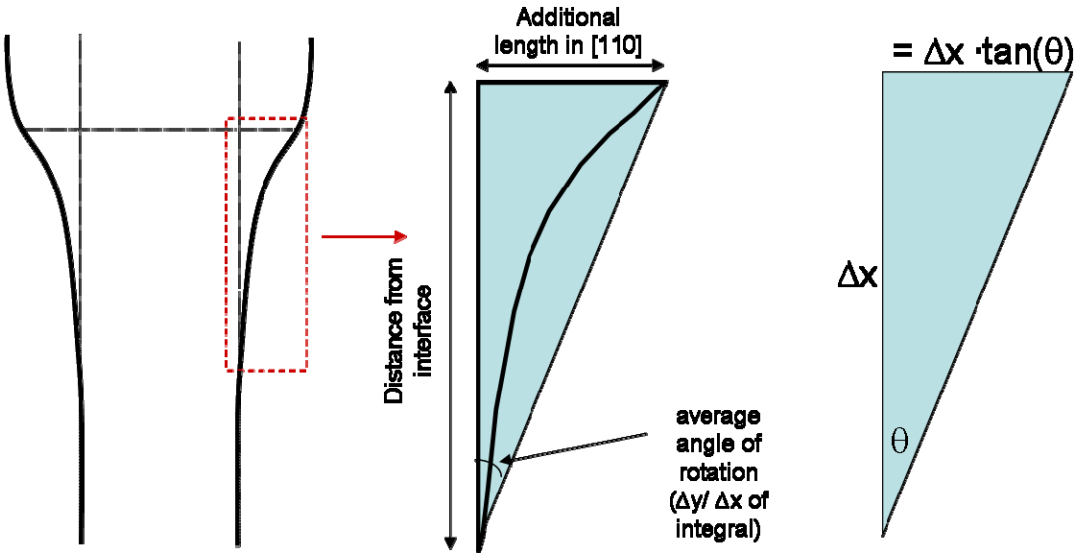

Figure A.1 – Schematic of a relaxed specimen and the values necessary to calculate the strain in the direction of relaxation.

A simplified hypothetical example of relaxation is shown in Figure A.2. The HOLZ line width versus distance from the interface curve for this example is shown in Figure A.3. Integrating this curve shows that the integrated curve provides the average angle of rotation ($\Delta y/\Delta x = \theta$) and the distance over which this occurs (Δx) as illustrated in Figure A.4.

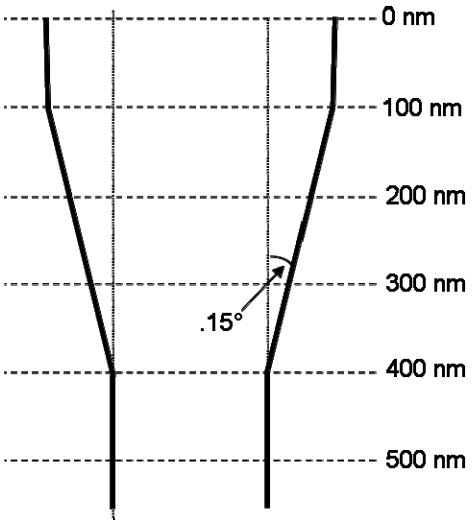

Figure A.2 – Simple relaxed structure for demonstrating the relaxation strain calculation.

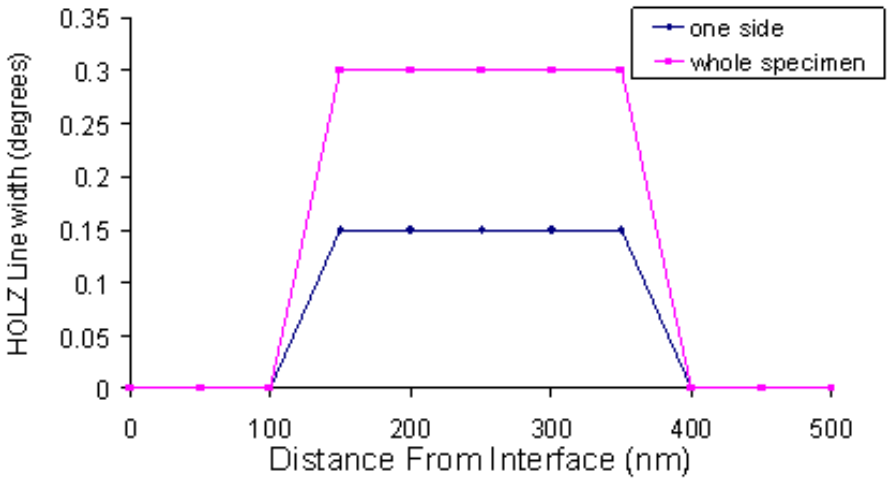

Figure A.3 – HOLZ line splitting for the hypothetical specimen in Figure A.2.

For an experimental curve this means first getting a baseline width of the HOLZ line from the unstrained region and subtracting this value from the whole curve as shown in Figures A.5 and A.6. Since the curve represents the whole specimen and the relaxation appears to be symmetric, the whole curve can be divided by two to represent

the relaxation behavior on only one side (Figure A.7). This curve is then fit with a polynomial equation due to the good approximation and ease of integration. Integrating this curve then provides the two values needed, $\Delta y/\Delta x$ and Δx, as shown in Figure A.8.

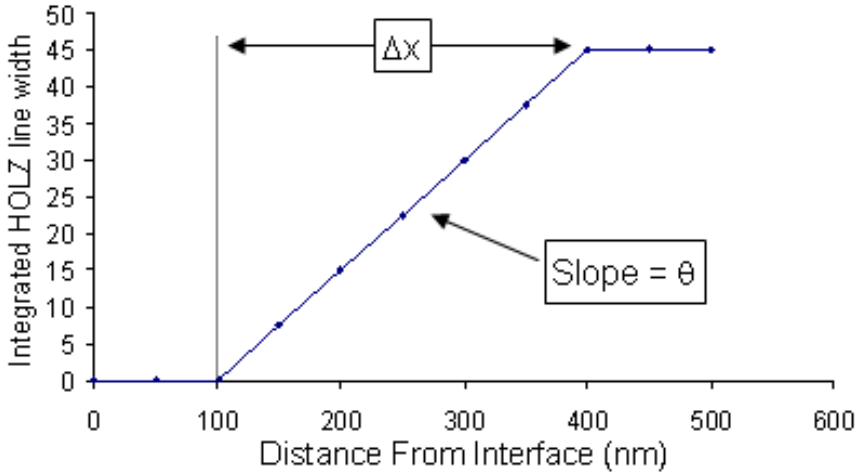

Figure A.4 – Integral of the HOLZ line splitting curve for one side of the specimen from Figure A.3.

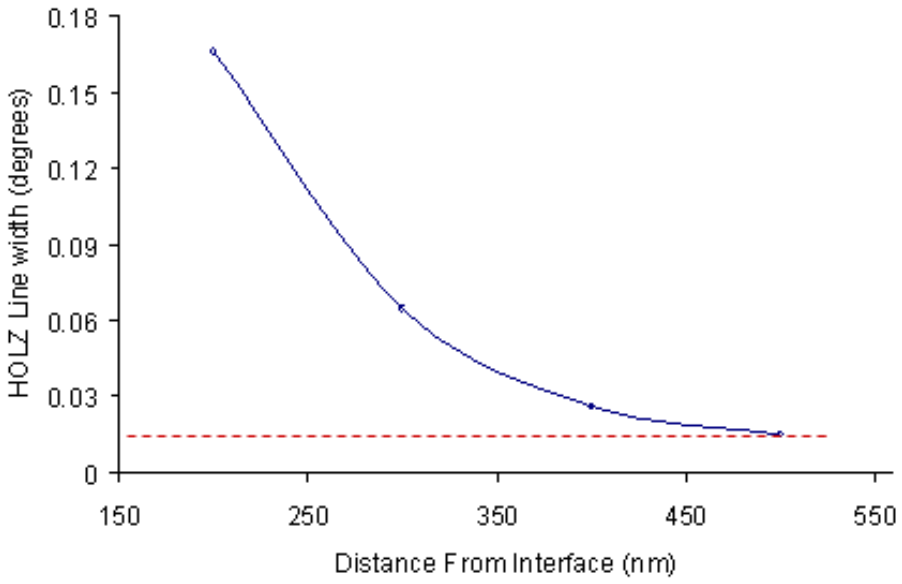

Figure A.5 – Sample experimental HOLZ line splitting curve as a function of distance from the interface. The dashed red line indicates the width of the unsplit HOLZ line.

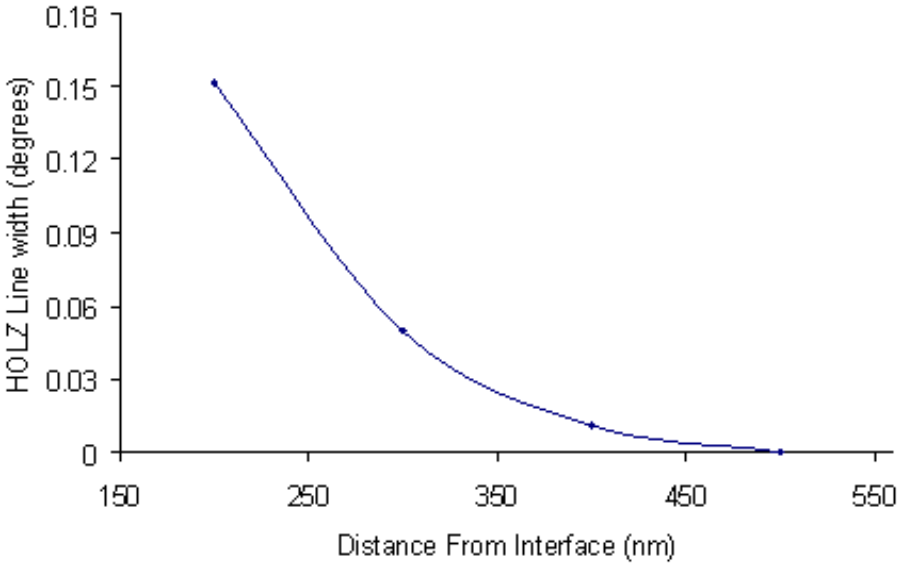

Figure A.6 – The curve from Figure A.5 with the width of the unsplit HOLZ line subtracted off of all the HOLZ line width values.

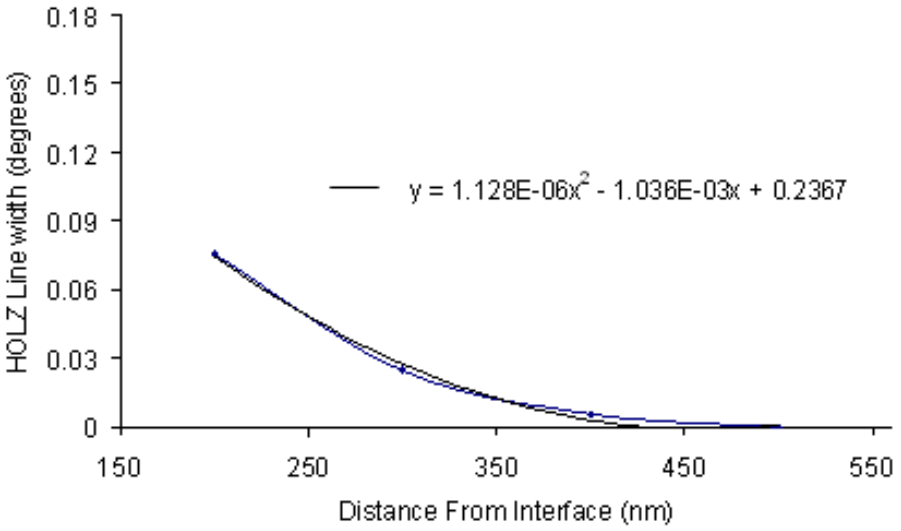

Figure A.7 – The curve from Figure A.6 divided in half to represent the relaxation behavior on one side of the specimen. This curve is fit with a polynomial equation.

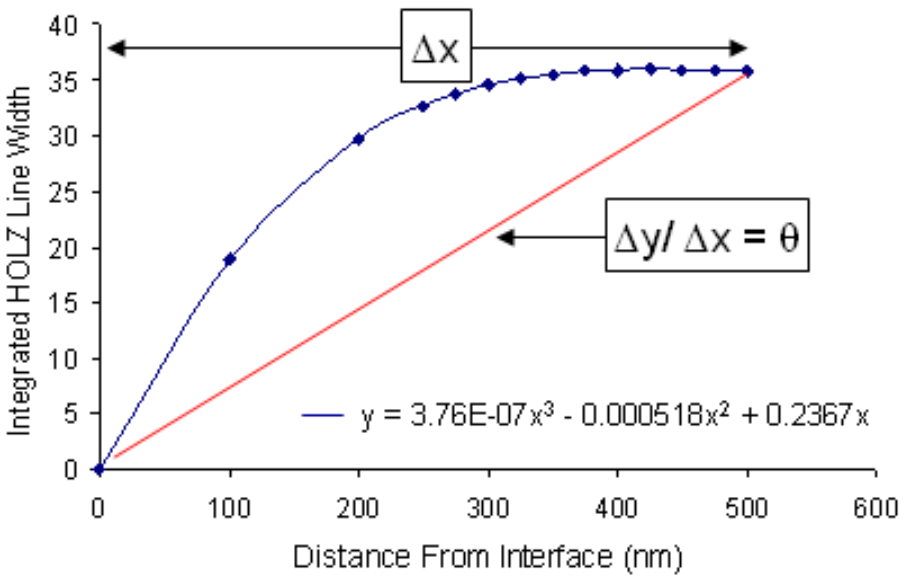

Figure A.8 – Integral of the curve in Figure A.7 indicating the Δx and θ values needed to calculate the relaxation strain as illustrated in Figure A.1.

It is noted that in this research the behavior of the $\bar{1}17$ HOLZ line splitting is being used to approximate that of the SiGe/silicon interface plane, which is a (001) plane. The angle between these two planes is ~11°. For a rotation about the $[1\bar{1}0]$ axis, this approximation will lead to an underestimate of the angle of rotation by about 2%.

APPENDIX B

SENSITIVITIES OF EACH PAIR OF INTERSECTION POINTS FOR EACH ZONE AXIS

<670> ZONE AXIS

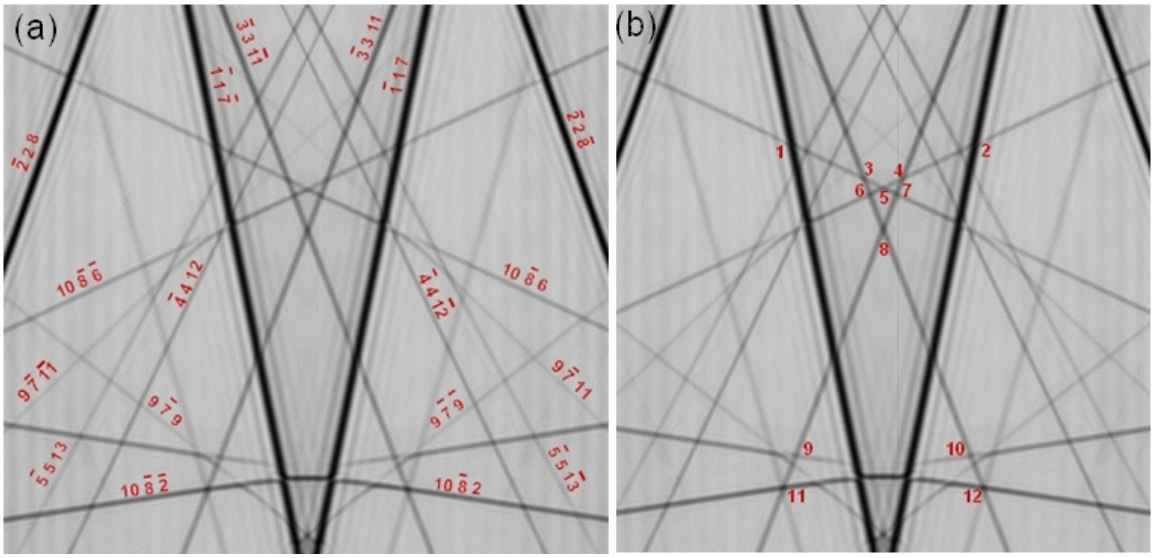

Figure B.1 – (a) The labeled HOLZ lines for the <670> zone axis. (b) The intersection points used for the strain determination.

Table B.1 – The strain sensitivities for the intersection pairs used for the strain determination from the <670> HOLZ line images.

Intersection Pair	Voltage Sensitivity (kV)	[110] Axis Strain Sensitivity	$[1\bar{1}0]$ Axis Strain Sensitivity	[001] Axis Strain Sensitivity
1-8	0.09	2.42×10^{-4}	3.42×10^{-4}	1.74×10^{-4}
2-8	0.09	2.42×10^{-4}	3.42×10^{-4}	1.74×10^{-4}
3-8	0.06	1.72×10^{-4}	2.45×10^{-4}	1.32×10^{-4}
4-8	0.06	1.72×10^{-4}	2.45×10^{-4}	1.32×10^{-4}
5-8	0.08	2.21×10^{-4}	3.20×10^{-4}	1.72×10^{-4}
6-8	0.09	2.43×10^{-4}	3.45×10^{-4}	1.91×10^{-4}
7-8	0.09	2.43×10^{-4}	3.45×10^{-4}	1.91×10^{-4}
9-8	0.08	2.22×10^{-4}	2.96×10^{-4}	1.87×10^{-4}
10-8	0.08	2.22×10^{-4}	2.96×10^{-4}	1.87×10^{-4}
11-8	0.08	2.03×10^{-4}	2.72×10^{-4}	1.66×10^{-4}
12-8	0.08	2.03×10^{-4}	2.72×10^{-4}	1.66×10^{-4}
3-4	0.09	2.60×10^{-4}	3.41×10^{-4}	1.89×10^{-4}
3-7	0.10	2.74×10^{-4}	3.67×10^{-4}	1.99×10^{-4}
4-6	0.10	2.74×10^{-4}	3.67×10^{-4}	1.99×10^{-4}
9-10	0.10	3.25×10^{-4}	4.38×10^{-4}	2.46×10^{-4}
11-12	0.11	2.89×10^{-4}	4.00×10^{-4}	2.30×10^{-4}

<340> ZONE AXIS

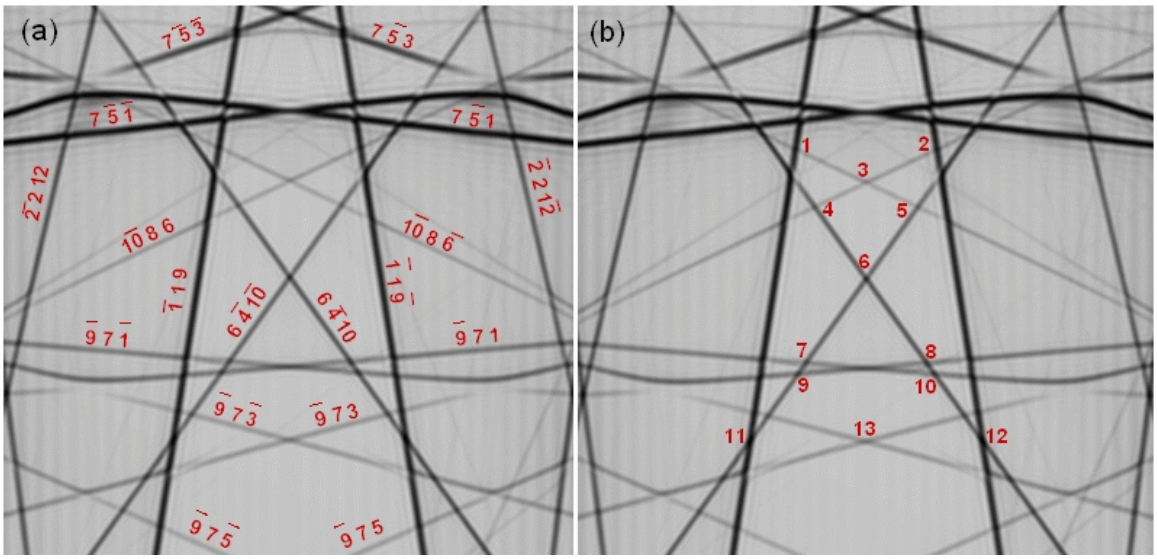

Figure B.2 – (a) The labeled HOLZ lines for the <340> zone axis. (b) The intersection points used for the strain determination.

Table B.2 – The strain sensitivities for the intersection pairs used for the strain determination from the <340> HOLZ line images.

Intersection Pair	Voltage Sensitivity (kV)	[110] Axis Strain Sensitivity	$[1\bar{1}0]$ Axis Strain Sensitivity	[001] Axis Strain Sensitivity
1-6	0.09	2.85×10^{-4}	3.32×10^{-4}	2.26×10^{-4}
2-6	0.09	2.85×10^{-4}	3.32×10^{-4}	2.26×10^{-4}
3-6	0.08	2.74×10^{-4}	2.46×10^{-4}	2.83×10^{-4}
4-6	0.09	2.75×10^{-4}	2.70×10^{-4}	3.10×10^{-4}
5-6	0.09	2.75×10^{-4}	2.70×10^{-4}	3.10×10^{-4}
7-6	0.08	2.80×10^{-4}	2.41×10^{-4}	3.02×10^{-4}
8-6	0.08	2.80×10^{-4}	2.41×10^{-4}	3.02×10^{-4}
9-6	0.08	2.65×10^{-4}	2.09×10^{-4}	2.09×10^{-4}
10-6	0.08	2.75×10^{-4}	2.25×10^{-4}	3.23×10^{-4}
13-6	0.10	3.25×10^{-4}	2.86×10^{-4}	2.86×10^{-4}
4-5	0.08	2.26×10^{-4}	2.31×10^{-4}	2.58×10^{-4}
7-8	0.07	2.36×10^{-4}	1.97×10^{-4}	2.63×10^{-4}
9-10	0.07	2.17×10^{-4}	1.73×10^{-4}	2.17×10^{-4}

<230> ZONE AXIS

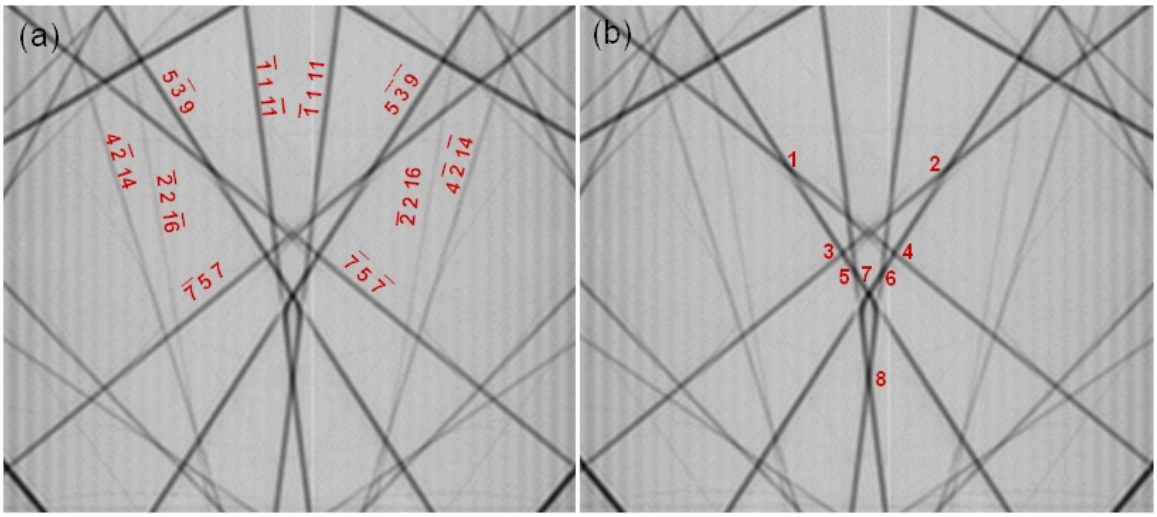

Figure B.3 – (a) The labeled HOLZ lines for the <230> zone axis. (b) The intersection points used for the strain determination.

Table B.3 – The strain sensitivities for the intersection pairs used for the strain determination from the <230> HOLZ line images.

Intersection Pair	Voltage Sensitivity (kV)	[110] Axis Strain Sensitivity	$[1\bar{1}0]$ Axis Strain Sensitivity	[001] Axis Strain Sensitivity
1-2	0.03	1.08×10^{-4}	1.30×10^{-4}	8.98×10^{-5}
1-3	0.05	1.74×10^{-4}	2.04×10^{-4}	1.42×10^{-4}
2-4	0.05	1.74×10^{-4}	2.04×10^{-4}	1.42×10^{-4}
1-4	0.04	1.32×10^{-4}	1.53×10^{-4}	1.07×10^{-4}
2-3	0.04	1.32×10^{-4}	1.53×10^{-4}	1.07×10^{-4}
1-5	0.03	8.97×10^{-5}	1.35×10^{-4}	6.23×10^{-5}
2-6	0.03	8.97×10^{-5}	1.35×10^{-4}	6.23×10^{-5}
1-7	0.04	1.20×10^{-4}	1.41×10^{-4}	9.85×10^{-5}
2-7	0.04	1.20×10^{-4}	1.41×10^{-4}	9.85×10^{-5}
5-8	0.02	8.38×10^{-5}	8.08×10^{-4}	3.87×10^{-5}
6-8	0.02	8.38×10^{-5}	8.08×10^{-4}	3.87×10^{-5}

REFERENCES

[1] G.E. Moore, Electronics, **38**, 114–7 (1965).

[2] S.E. Thompson, M. Armstrong, C. Auth, M. Alavi, M. Buehler, R. Chau, S. Cea, T. Ghani, G. Glass, T. Hoffman, C.-H. Jan, C. Kenyon, J. Klaus, K. Kuhn, M. Zhiyong, B. Mcintyre, K. Mistry, A. Murthy, B. Obradovic, R. Nagisetty, N. Phi S. Sivakumar, R. Shaheed, L. Shifren, B. Tufts, S. Tyagi, M. Bohr, Y. El-Mansy, IEEE Transactions on Electron Devices, **51**, 1790-7 (2004).

[3] S. Kubicek and K. DeMeyer, Advanced Semiconductor Devices and Microsystems, 259-69 (2002).

[4] S.E. Thompson, R.S. Chau, T. Ghani, K. Mistry, S. Tyagi, M.T. Bohr, IEEE Transactions on Semiconductor Manufacturing, **18**, 26-35 (2005).

[5] P.R. Chidambaram, B.A. Smith, L.H. Hall, H. Bu, S. Chakravarthi, Y. Kim, A.V. Samoilov, A.T. Kim, P.J. Jones, R.B. Irwin, M.J. Kim, A.L.P. Rotondaro, C.F. Machala, and D.T. Grider, 2004 Symp. on VLSI Tech. Dig. of Technical Papers, 48 (2004).

[6] V. Moroz, X. Xiaopeng, D. Pramanik, F. Nouri, Z. Krivokapic, Solid State Technology, **47**, 49-52 (2004).

[7] K. Rim, R. Anderson, D. Boyd, F. Cardone, K. Chan, H. Chen, S. Christansen, J. Chu, K. Jenkins, T. Kanarsky, S. Koester, B.H. Lee, K. Lee, V. Mazzeo, A. Mocuta, D. Mocuta, P.M. Mooney, P. Oldiges, J. Ott, P. Ronsheim, R. Roy, A. Steegen, M. Yang, H. Zhu, M. Ieong, H.-S.P. Wong, Solid-State Electronics, **47**, 1133-1139 (2003).

[8] T. Ghani, M. Armstrong, C. Auth, M. Bost, P. Charvat, G. Glass, T. Hoffiann, K. Johnson, C. Kenyon, J. Klaus, B. Mclntyre, K. Mistry, A. Murthy, J. Sandford, M. Silberstein, S. Sivakumar, P. Smith, K. Zawadzki, S. Thompson, M. Bohr, IEEE International Electron Devices Meeting 2003, 11.6.1-3 (2003).

[9] C. Mazure, I. Cayrefourcq, 2005 IEEE International SOI Conference - Proceedings, 1-6 (2005).

[10] L. Collins, IEE Review, **49**, 46-9 (2003).

[11] *B.* Dietrich, E. Bugiel, J. Klatt, G. Lippert, T. Morgenstern, H.J. Osten, P. Zaumseil, Journal of Applied Physics, **74**, 3177-80 (1993).

[12] I. De Wolf, V. Senez, R. Balboni, A. Armigliato, S. Frabboni, A. Cedola, S. Lagomarsino, Microelectronic Engineering, **70**, 425-35 (2003).

[13] M. Erdtmann, T.A. Langdo, Journal of Materials Science: Materials in Electronics, **17**, 137-47 (2006).

[14] W.J. Bartels, W. Nijman, J. Cryst. Growth, **44,** S18 (1978).

[15] L.E. Levine, B.C. Larson, W. Yang, M.E. Kassner, J.Z. Tischler, M.A. Delos-Reyes, R.J. Fields, W. Liu, Nature Materials, **5**, 619-22 (2006).

[16] S. Webster, D.N. Batchelder, D.A. Smith, Applied Physics Letters, **72**, 1478-80 (1998).

[17] D. Wood, G. Cooper, D.J. Gardiner, M. Bowden, *Journal of Materials Science Letters*, **16**, 1222-3 (1997).

[18] J.Vanhellemont, I. De Wolf, K.G.F Janssens, S. Frabboni, R. Balboni, Applied Surface Science, **63**, 119-25 (1993).

[19] W. Kossel, G. Möllenstedt, Ann. Phys., **36**, 113-40 (1939).

[20] J. Gjønnes, A.F. Moodie, Acta Crystallogr., **19**, 65–7 (1965).

[21] P.M. Jones, G.M. Rackham, J.W. Steeds, Proceedings of The Royal Society of London, Series A: Mathematical and Physical Sciences, **354**, 197-222 (1977).

[22] J.M. Zuo, Ultramicroscopy, **41**, 211-23 (1992).

[23] C.J. Humphreys, D.J. Eaglesham, D.M. Maher, H.L. Fraser, Ultramicroscopy, **26**, 13-24 (1988).

[24] M.E. Twigg, S.N.G. Chu, Ultramicroscopy, **26**, 51-8 (1988).

[25] R. Balboni, A. Armigliato, S. Frabboni, Applied Physics Letters, **68**, 2831-3 (1996).

[26] M.E. Twigg, S.N.G. Chu, D.C. Joy, D.M. Maher, A.T. Macrander, A.K. Chin, Journal of Applied Physics, **62**, 3156-60 (1987).

[27] S. Kramer, J. Mayer, Journal of Microscopy, **194**, 2-11 (1999).

[28] P.A. Stadelmann, Ultramicroscopy, **21**, 131-45 (1987).

[29] A. Chuvilin, U. Kaiser, Ultramicroscopy, **104**, 73-82 (2005).

[30] Deliverable D2, STREAM Project, http://stream.bo.cnr.it (2000).

[31] S.M. Hu, Journal of Applied Physics, **70**, R53-80 (1991).

[32] A. Armigliato, R. Balboni, G.P. Carnevale, G. Pavia, D. Piccolo, S. Frabboni, A. Benedetti, A.G. Cullis, Applied Physics Letters, **82**, 2172-4 (2003).

[33] N. Hashikawa, K. Fukumoto, T. Kuroi, M. Ikeno, Y. Mashiko, Microelectronics Reliability, **38**, 913-17 (1998).

[34] S.L. Toh, K. Li, C.H. Ang, E. Er, S. Redkar, K.P. Loh, C.B. Boothroyd, L. Chan, Proceedings of the 11th International Symposium on the Physical and Failure Analysis of Integrated Circuits, IPFA 2004, 143-6 (2004).

[35] A. Toda, I. Tsukuba, N. Ikarashi, H. Ono, Journal of Crystal Growth, **210**, 341-5 (2000).

[36] A. Armigliato, A. Spessot, R. Balboni, A. Benedetti, G. Carnevale, S. Frabboni, G. Mastracchio, G. Pavia, Journal of Applied Physics, **99**, 064504 (2006).

[37] C.K. Maiti, L.K. Bera, S. Chattopadhyay, Semiconductor Science and Technology, **13**, 1225-46 (1998).

[38] R. Balboni, S. Frabboni, A. Armigliato, Philosophical Magazine A (Physics of Condensed Matter: Structure, Defects and Mechanical Properties), **77**, 67-83 (1998).

[39] G. Bhagavannarayana, S.K. Halder, Journal of Applied Physics, **97**, 024509-1-6 (2005).

[40] F. Schaffler, in Properties of Advanced Semiconductor Materials GaN, AlN, InN, BN, SiC, SiGe., Eds. M.E. Levinshtein, S.L. Rumyantsev, M.S. Shur, John Wiley & Sons, Inc., New York, 149-188 (2001).

[41] Deliverable D10, STREAM Project, http://stream.bo.cnr.it (2001).

[42] S. Frabboni, F. Gambetta, A. Armigliato, R. Balboni, S. Balboni, F. Cembali, Physical Review B (Condensed Matter), **60**, 13750-61 (1999).

[43] A. Armigliato, R. Balboni, A. Benedetti, S. Frabboni, A. Tixier, J. Vanhellemont, Journal de Physique III, **7**, 2375-81 (1997).

[44] C. Stuer, J. Van Landuyt, H. Bender, R. Rooyackers, G. Badenes, Materials Science in Semiconductor Processing, **4**, 117-9 (2001).

[45] T. Akaogi, K. Tsuda, M. Terauchi, M. Tanaka, Journal of Electron Microscopy, **55,** 129–35 (2006).

[46] V. Hou, D. Li, Microsc. Microanal., **10 Suppl. 2**, 584 (2004).

[47] A. Toda, N. Ikarashi, H. Ono, Journal of Microscopy, **203**, 239-45 (2001).

[48] I. Berbezier, B. Gallas, A. Ronda, J. Derrien, Surface Science, **412-3**, 415-29 (1998)

[49] L. Clement, R. Pantel, L.F.Tz. Kwakman, J.L. Rouviere, Applied Physics Letters, **85**, 651-3 (2004).

[50] M.M.J. Treacy, J.M. Gibson, Journal of Vacuum Science & Technology B (Microelectronics Processing and Phenomena), **4**, 1458-66 (1986).

[51] D.D. Perovic, G.C. Weatherly, D.C. Houghton, Journal of Vacuum Science & Technology A (Vacuum, Surfaces, and Films), **6**, 1333-6 (1988).

[52] A. Fischer, H. Kuehne, G. Lippert, H. Richter, B. Tillack, Physica Status Solidi (A) Applied Research, **171**, 475-85 (1999).

[53] A.J. Wilkinson, Applied Physics Letters, **89**, 241910-1-3 (2006).

[54] A.R. Khan, J. Stangl, G. Bauer, D. Buca, B. Hollander, H. Trinkaus, S. Mantl, R. Loo, M. Caymax, Semiconductor Science and Technology, **22**, S212-5 (2007).

[55] S. Chakravarthi, unpublished research (2006).

[56] D. Zubia, S.D. Hersee, T. Khraishi, Applied Physics Letters, **80**, 740 (2002).

[57] C.T. Chou, S.C. Anderson, D.J.H Cockayne, A.Z. Sikorski, M.R. Vaughan, Ultramicroscopy, **55**, 334-47 (1994).

[58] F. Houdellier, C. Roucau, L. Clement, J.L. Rouviere, M.J. Casanove, Ultramicroscopy, **106**, 951-9 (2006).

[59] A. Chuvilin, U. Kaiser, Q. de Robillard, H.-J. Engelmann, Journal of Electron Microscopy, **54**, 515-7 (2005).

[60] J.M. Zuo, K. Miyoung, R. Holmestad, Journal of Electron Microscopy, **47**, 121-7 (1998).

[61] A. Armigliato, R. Balboni, S. Frabboni, Applied Physics Letters, **86**, 63508-1-3 (2005).

[62] J. Huang, M.J. Kim, P.R. Chidambaram, R.B. Irwin, P.J Jones, J.W. Weijtmans, E.M. Koontz, Y.G. Wang, S. Tang, R. Wise, Applied Physics Letters, **89**, 63114-1-3 (2006).

[63] J.A. Nucci, R.R. Keller, S. Kramer, C.A. Volkert, M.E. Gross, Materials, Technology and Reliability for Advanced Interconnects and Low-k Dielectrics. Symposium, **MRS Symposium Proceedings Vol.612**, 1-6 (2001).

[64] P. Paczkowski, M. Gigla, A. Kostka, H. Morawiec, Materials Chemistry and Physics, **81**, 233-6 (2003).

[65] S.J. Rozeveld, J.M. Howe, Ultramicroscopy, **50**, 41-56 (1993).

[66] R. Wittmann, C. Parzinger, D. Gerthsen, Ultramicroscopy, **70**, 145-59 (1998).

[67] R. Wittmann, P. Kruse, M. Frauenkron, D. Gerthsen, Philosophical Magazine A (Physics of Condensed Matter: Structure, Defects and Mechanical Properties), **80**, 2215-32 (2000).

[68] S. Kramer, J. Mayer, C. Witt, A. Weickenmeier, M. Ruhle, Ultramicroscopy, **81**, 245-62 (2000).

[69] A. Chuvilin, T. Kups, U. Kaiser, Journal of Electron Microscopy, **53**, 237-44 (2004).

[70] A. Morawiec, Philosophical Magazine, **85**, 1611-23 (2005).

[71] A. Armigliato, R. Balboni, A. Benedetti, S. Frabboni, High-Pressure Crystallography., Eds. A. Katrusiak, P. F. McMillan, Kluwer Academic Publishers, Netherlands, 277, (2004).

[72] S.L. Toh, K.P. Loh, C.B. Boothroyd, K. Li, C.H. Ang, L. Chan, Journal of Vacuum Science and Technology B: Microelectronics and Nanometer Structures, **23**, 940-6 (2005).

[73] V. Senez, A. Armigliato, I. De Wolf, G. Carnevale, R. Balboni, S. Frabboni, A. Benedetti, Journal of Applied Physics, **94**, 5574-83 (2003).

[74] Y.-C. Yeo, J. Sun, Applied Physics Letters, **86**, 023103-1-3 (2005).

[75] D.M. Maher, H.L. Fraser, C.J. Humphreys, R.V. Knoell, J.C. Bean, Applied Physics Letters, **50**, 574-6 (1987).

[76] D.J. Eaglesham, D.M. Maher, H.L. Fraser, C.J. Humphreys, J.C. Bean, Applied Physics Letters, **54**, 222-4 (1989).

[77] W. Zhao, G. Duscher, G. Rozgonyi, M.A. Zikry, S. Chopra, M.C. Ozturk, Applied Physics Letters, **90**, 191907 (2007).

[78] R. Zhu, E. Pan, P.W. Chung, X. Cai, K.M. Liew, A. Buldum, Semiconductor Science and Technology, **21**, 906-11 (2006).

[79] A. Ballato, IEEE Transactions on Ultrasonics, Ferroelectrics and Frequency Control, **43**, 56-62 (1996).

[80] J.M. Gere, Mechanics of Materials., Brooks/Cole, Belmont, CA, 501 (2004).